Search for point like sources of ultra high energy cosmic rays by evaluating small scale clusters of cosmic ray arrival directions observed by the Telescope Array

Graduate School of Science,
Osaka City University
2011/03

D07SA004
Takeshi Okuda

Abstract

Cosmic rays are the high energy particles and γ rays from space. High energy cosmic rays in atmosphere interact nuclei of atmosphere, and then induce a lot of particles and γ rays. This phenomenon is called air shower. The number of cosmic rays decreases as the energy of cosmic rays increases. The arrival frequency of ultra high energy cosmic rays($E \gtrsim 10^{19}$eV) is about 1 /km^2/year. Knowledge of the origin, propagation and the kind of particle of ultra high energy cosmic rays, or the interaction of this energy region is helpful to figure out the universe or high energy physics.

Telescope Array(TA) experiment detects air showers induced by extremely high energy cosmic rays in the middle west of Utah in the United States. The TA experiment consists of two different types of detectors i.e. atmospheric fluorescence detectors(FDs) and surface array detectors(SDs). The SD observation started in March 2008.

In this thesis, I describe about surface array detectors and shower reconstruction method. Finally, I describe that the searching small clusters with auto-correlation analysis by the 850-day data from surface array detectors of Telescope Array. For example, there are 42 events whose energy is higher than 40 EeV. The observed number of clusters within 2.5° is 1. The expected number of clusters within 2.5° from 42 events isotropic model is 0.84. And that deviation is 0.92. As a result, there is no indication of small clusters from TASD more than isotropic model. If these cosmic rays are proton, this result does not favor simultaneous situation that the intergalactic magnetic field is weak and the number density of cosmic ray source is small.

Contents

1 Introduction

1.1 Ultra High Energy Cosmic Rays

1.1.1 Origin

Cosmic rays are high energy protons, nuclei or photon(γ ray) from outer space. It is said that the origin of high energy cosmic rays is supernova or collision of moving plasma gasses and charged particles [11]. The size of acceleration region is greater than the gyroradius in a magnetic field for accelerating particles up to 10^{20} eV, in order to keep the particles in the region to accelerate. However, the magnetic field should be weak to avoid large synchrotron radiation loss compared with acceleration [1]. The candidate objects for acceleration which concern the size and the strength of magnetic field is shown in Figure 1.

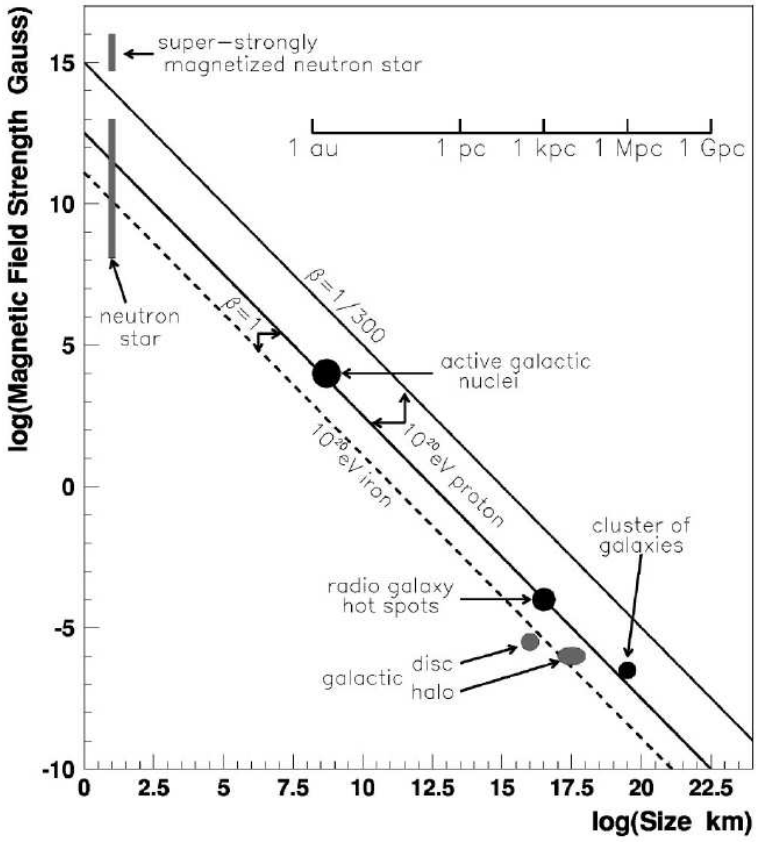

Figure 1: Candidate objects for acceleration up to 10^{20} eV concerned about magnetic strength and object size [1].

About the origin of ultra high energy cosmic rays, there are some hypotheses like these. The iron nucleus is accelerated by shock of galactic wind up to 10^{19} eV, by young neutron star with strong magnetic field up to 10^{20} eV. In radio galaxy hot spots whose size is a few kpc and magnetic field is a few hundred μG, the maximum accelerated energy is $\sim 10^{20}$ eV. These hot spots are shocks of jets from the central active galactic nucleus. In diffusive accretion shocks which is formed by clusters of galaxies, the particles can be accelerated

to ultra high energy. The proton is accelerated by γ ray burst up to 10^{21} eV. The particle comes from superheavy particles whose mass is more than 10^{21} eV. The Lorentz transformation is not valid for this energy region [1].

The acceleration by moving magnetic field in the space [2]. When a cosmic ray interacts the magnetic field in the cloud (interstellar medium) without collision, the cosmic ray is scattered by magnetic field. This situation is shown in Figure 2. Here, the cosmic ray is with energy E_1 initially, and scattered out

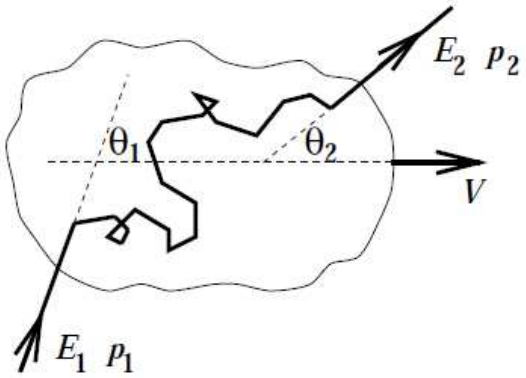

Figure 2: Particle acceleration by cloud moving with speed V [3].

with energy E_2. The cosmic ray energy is changed by Lorentz transformation between laboratory frame (without prime) and cloud rest frame (with prime).

$$E_1' = \gamma E_1 \left(1 - \beta \cos\theta_1\right) \tag{1}$$
$$E_2 = \gamma E_2' \left(1 + \beta \cos\theta_2'\right) \tag{2}$$

Here, $\beta = \frac{V}{c}$, $\gamma = \frac{1}{\sqrt{1-\beta^2}}$. Because of elastic scattering by magnetic field without collision, $E_2' = E_1'$. Therefore,

$$\frac{E_2 - E_1}{E_1} = \frac{\Delta E}{E_1} = \frac{1 - \beta\cos\theta_1 + \beta\cos\theta_2' - \beta^2\cos\theta_1\cos\theta_2'}{1-\beta^2} - 1 \tag{3}$$

Then, it is calculated that the probability (P) per solid angle for irruption and escapement with cloud magnetic field. For the cloud rest frame, scattered out directions are random. Therefore, $\frac{dP}{d\Omega_2'}$ is constant. And the particles irrupt from the front side of the cloud more than the back side. Therefore,

$$\frac{dP}{d\Omega_1} \propto v_1 - V\cos\theta_1 \propto 1 - \beta\cos\theta_1 \tag{4}$$

Here, the irruptive particle velocity is approximately c. Then, the average of $\cos\theta_1$, $\cos\theta_2'$ is calculated.

$$\langle\cos\theta_1\rangle = \frac{\int \cos\theta_1 \frac{dP}{d\Omega_1} d\Omega_1}{\int \frac{dP}{d\Omega_1} d\Omega_1} = \frac{\int_0^\pi \cos\theta_1 (1 - \beta\cos\theta_1)\sin\theta_1 d\theta_1}{\int_0^\pi (1-\beta\cos\theta_1)\sin\theta_1 d\theta_1} = -\frac{\beta}{3} \tag{5}$$

$$\langle\cos\theta_2'\rangle = \frac{\int \cos\theta_2' \frac{dP}{d\Omega_2'} d\Omega_2'}{\int \frac{dP}{d\Omega_2'} d\Omega_2'} = \frac{\int_0^\pi \cos\theta_2' \sin\theta_2' d\theta_2'}{\int_0^\pi \sin\theta_2' d\theta_2'} = 0 \tag{6}$$

Therefore, using Equation (3),

$$\frac{\Delta E}{E_1} = \frac{1+\frac{1}{3}\beta^2}{1-\beta^2} - 1 = \frac{1}{1-\beta^2}\cdot\frac{4}{3}\beta^2 \simeq \frac{4}{3}\beta^2 \tag{7}$$

Here, $\beta \ll 1$. This acceleration efficiency is second order of β. When a cosmic ray interacts the magnetic field in the shock (by supernova) without collision, the cosmic ray is scattered by magnetic field. This situation is shown in Figure 3. In this situation, Equation (3) is also valid with $\beta = \frac{V_p}{c}$. Then, it

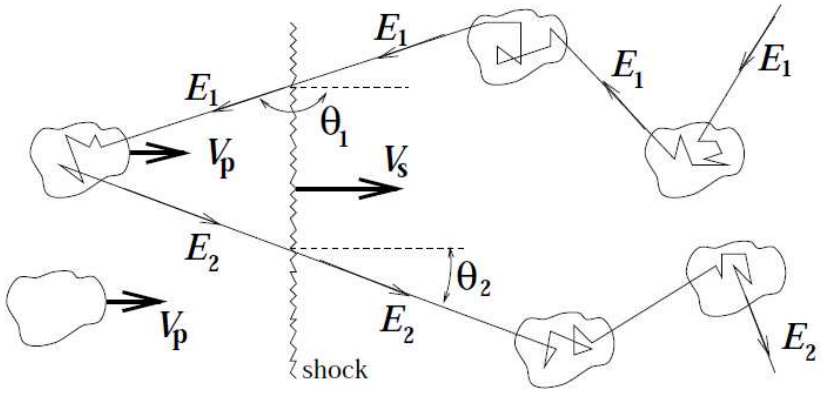

Figure 3: Particle acceleration by shock wave moving with speed V_s [3].

is calculated that the probability (P) per solid angle for passing through the shock front.

$$\frac{dP}{d\Omega_1} \propto \begin{cases} 0\ , & (\theta_1 : 0 \to \frac{\pi}{2}) \\ -\cos\theta_1\ , & (\theta_1 : \frac{\pi}{2} \to \pi) \end{cases} \tag{8}$$

$$\frac{dP}{d\Omega_2'} \propto \begin{cases} \cos\theta_2'\ , & (\theta_2' : 0 \to \frac{\pi}{2}) \\ 0\ , & (\theta_2' : \frac{\pi}{2} \to \pi) \end{cases} \tag{9}$$

Then, the average of $\cos\theta_1,\ \cos\theta_2'$ is calculated.

$$\langle\cos\theta_1\rangle = \frac{\int \cos\theta_1 \frac{dP}{d\Omega_1} d\Omega_1}{\int \frac{dP}{d\Omega_1} d\Omega_1} = \frac{\int_{\frac{\pi}{2}}^{\pi} \cos^2\theta_1 \sin\theta_1 d\theta_1}{\int_{\frac{\pi}{2}}^{\pi} \cos\theta_1 \sin\theta_1 d\theta_1} = -\frac{2}{3} \tag{10}$$

$$\langle\cos\theta_2'\rangle = \frac{\int \cos\theta_2' \frac{dP}{d\Omega_2'} d\Omega_2'}{\int \frac{dP}{d\Omega_2'} d\Omega_2'} = \frac{\int_{0}^{\frac{\pi}{2}} \cos^2\theta_2' \sin\theta_2' d\theta_2'}{\int_{0}^{\frac{\pi}{2}} \cos\theta_2' \sin\theta_2' d\theta_2'} = \frac{2}{3} \tag{11}$$

Therefore, using Equation (3),

$$\frac{\Delta E}{E_1} = \frac{1+\frac{4}{3}\beta+\frac{4}{9}\beta^2}{1-\beta^2} - 1 = \frac{1+\frac{13}{12}\beta}{1-\beta^2}\cdot\frac{4}{3}\beta \simeq \frac{4}{3}\beta \tag{12}$$

Here, $\beta \ll 1$. This acceleration efficiency is first order of β. Therefore, shock acceleration is more efficient for energy gain.

1.1.2 Propagation

About the ultra high energy cosmic rays (UHECRs), it is very hard to determine their composition (proton, nucleus, γ). The cosmic rays propagate in space, with bending by magnetic field or colliding with interstellar gasses. Especially, UHECRs interact cosmic background radiation during propagation and lose their energy. Therefore, the cosmic rays ($E \sim 10^{20}$ eV) from several tens of Mpc far can not get to the Earth. However, there are papers which report the observation of the cosmic rays over 10^{20} eV [7][6]. The energy flux over 6×10^{19} eV should decrease rapidly more than lower energy region. This decrease is called GZK cutoff [4][5][1].

The ultra high energy protons interact Cosmic Microwave Background (CMB).

$$p + \gamma(2.7\mathrm{K}) \rightarrow p + \pi^0,\ n + \pi^+ \tag{13}$$
$$p + \gamma(2.7\mathrm{K}) \rightarrow p + e^+ + e- \tag{14}$$

The peak energy of CMB photon is 6×10^{-4} eV and the density of photon is 400 /cm^2. For pair production(14), the energy threshold of proton is 10^{18} eV, the mean free path is ~ 1 Mpc. For pion production(13), the energy threshold of proton is $10^{19.6}$ eV, the mean free path is ~ 6 Mpc. The energy losses for these interactions are 0.1 % for pair production, 20 % for pion production. Therefore, the pion production is more significant than the pair production [1].

The ultra high energy heavy nuclei of mass A interact CMB.

$$A + \gamma(2.7\mathrm{K}) \rightarrow (A-1) + N,\ (A-2) + 2N \quad (N:\ p\ or\ n) \tag{15}$$
$$A + \gamma(2.7\mathrm{K}) \rightarrow A + e^+ + e- \tag{16}$$

The photodisintegration(15) is significant process above 2×10^{20} eV. For pair production(16), the nucleus does not disintegrate. This process is significant above 5×10^{19} eV [1].

The ultra high energy γ rays interact CMB.

$$\gamma + \gamma(2.7\mathrm{K}) \rightarrow e^+ + e- \tag{17}$$

For pair production(17), the energy threshold of ultra high energy γ ray is 4×10^{14} eV [1].

The ultra high energy charged particles are bent by magnetic field in propagation. Therefore, the arrival directions of charged high energy cosmic rays are deflected by coherent magnetic field and random magnetic field. By coherent magnetic field, simplistically, the arrival directions from the source are deflected same way. In fact, this deflection is sizable for some direction to study anisotropy. However, for small cluster search, this deflection is treated as small effect. By random magnetic field, the arrival directions from the source are spread out. Here is the RMS of deflection by random galactic magnetic field [8].

$$\delta_{rms} = 0.6^\circ\ \frac{10^{20}[\mathrm{eV}]}{E/Z} \frac{B_{rms}}{4[\mathrm{uG}]} \sqrt{\frac{L}{3[\mathrm{kpc}]}} \sqrt{\frac{L_c}{50[\mathrm{pc}]}} \tag{18}$$

L_c is coherent lengh, $L_c \sim 20$ pc [8][9]. The magnetic field of our galaxy is about 3 uG around earth. If cosmic rays are protons and its energy is 4×10^{19} eV, $\delta_{rms} = 0.4^\circ \sqrt{L[\mathrm{kpc}]}$. The thickness of our galaxy is about 0.5 kpc, the radius of our galaxy is about 15 kpc. Therefore, $\delta_{rms} = 0.3^\circ \sim 1.5^\circ$. According to [10], the typical deflection is $0.2^\circ \sim 1.5^\circ$.

1.1.3 Air Shower by Cosmic Rays

High energy cosmic rays interact with atmospheric molecules, and generate high energy particles including photons. These generated secondary particles interact with atmospheric molecules, and then innumerable particles are generated. This is called the air shower phenomenon. As increasing the number of particles, the energy of individual particles is decreasing. The low energy particles do not generate particles by interaction with air. They are absorbed in atmosphere.

The air shower consists of nucleon, π meson and K meson which generate many particles, called nuclear cascade. π^0 meson in nuclear cascade decays to γ rays. Therefore, the air shower also consists of γ ray, electron and positron which are generated by high energy γ ray's pair creation and breaking radiation, called electromagnetic cascade. $\pi^\pm$ decays to $\mu^\pm$. The air shower by high energy cosmic γ ray mainly consists of electromagnetic cascade. If the cosmic ray is nucleus heavier than proton, cosmic nucleus are fragmented by interactions with atmosphere, and ramified its energy earlier than proton. Therefore, the shower particles by cosmic nucleus increase earlier than by cosmic proton.

The number of particles of longitudinal development is represent by Gaisser Hillas function as $N(E, X)$, E is the energy of primary cosmic ray, X is slant depth of atmosphere [11][12].

$$N(E, X) = S_0 \frac{E}{\varepsilon} e^{\frac{X_{max}-\lambda}{\lambda}} \left(\frac{X - X_1}{X_{max} - \lambda} \right)^{\frac{X_{max}-\lambda}{\lambda}} e^{-\frac{X-X_1}{\lambda}} \tag{19}$$

$$X_{max} = X_0^{'} \ln \left(\frac{E}{\varepsilon} \right) \tag{20}$$

Here, $S_0 = 0.045$, $\varepsilon = 74$ MeV, $\lambda = 70$ g/cm^2, $X_0^{'} = 36$ g/cm^2. X_1 is the slant depth at first interaction point of primary cosmic ray and atmosphere. If X_1 is set to 0, $N(E, X)$ is shown in Figure 4.

The number of particles of lateral distribution for electromagnetic cascade is represent by Nishimura-Kamata-Greisen function, (NKG function) [13]. This lateral function shape is determined by Moliere unit (unit by X_m).

$$X_m = \frac{E_s}{E_c} X_0, \quad E_s = m_e c^2 \sqrt{\frac{4\pi}{\alpha}} \tag{21}$$

Here, $E_s = 21.21$ MeV, $E_c = 87.92$ MeV [14] and $X_0 = 36.62$ g/cm^2 [14]. Therefore, $X_m = 8.832$ g/cm^2.

$$r_m = \frac{X_m}{\rho} \tag{22}$$

ρ is density of atmosphere. For NKG function, the atmospheric density of ground level is not used, $2X_0$ higher altitude density is used [13]. For Telescope

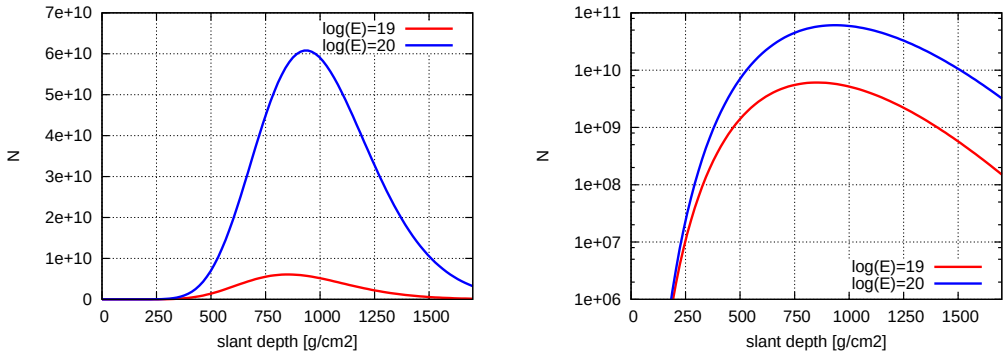

Figure 4: Longitudinal development by Gaisser-Hillas function for which primary energy is 10^{19} eV and 10^{20} eV.

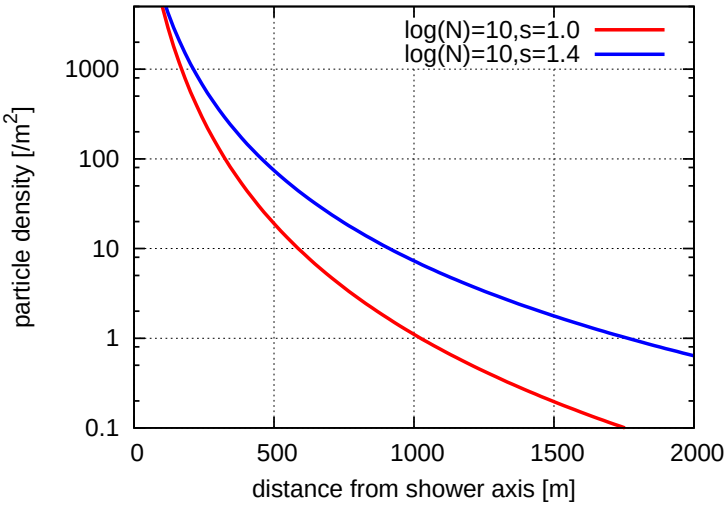

Figure 5: NKG function for which $\log N$ is set to 10 and two type of age s

Array site, altitude 1382 m is taken as origin. From US standard atmosphere, the pressure of this altitude is 858 hPa. 1 hPa=$\frac{100}{9.8}$ kg/m^2 $\times$9.8 m/s^2. Therefore, 1 g/cm^2 is equivalent to 0.98 hPa. 858 hPa-2X_0 hPa=786 hPa. For this pressure, the atmospheric density is 0.997×10^{-3} g/cm^3. Therefore, $r_m = 88.5$ m.

$$f(r) = NC(s) \left(\frac{r}{r_m}\right)^{s-2} \left(1 + \frac{r}{r_m}\right)^{s-4.5} \tag{23}$$

$$C(s) = \frac{1}{2\pi r_m^2} \frac{\Gamma(s)\Gamma(4.5-2s)}{\Gamma(4.5-s)} \tag{24}$$

The lateral distribution by NKG function is shown in Figure 5. s is the age parameter. s increases as shower development and $s = 1$ at maximum shower size.

The cosmic rays are measured directly by satellite and balloon, and also indirectly by ground based detectors measuring air showers. The differential energy spectrum of cosmic rays is shown as Figure 6. It decreases monotonically, about $Flux \propto E^{-3}dE$. Because the flux of cosmic rays at high energy is small, the detector on satellite or balloon, which has small detectable area,

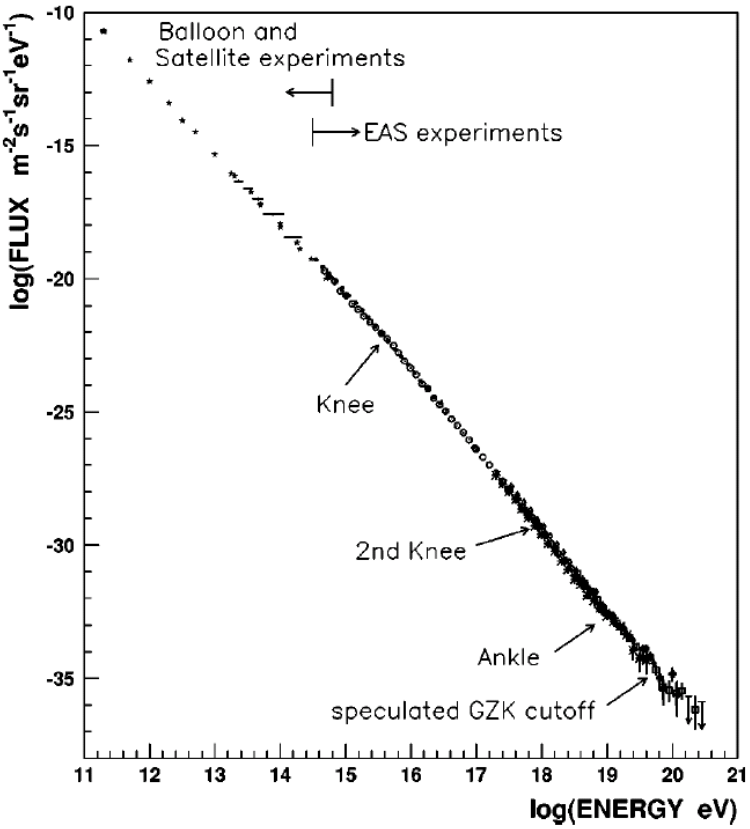

Figure 6: Energy Spectrum of Cosmic Rays [1].

can not get enough statistics over $E \sim 10^{15}$ eV. Therefore, the observation of cosmic rays over $E \sim 10^{15}$ eV takes place on the ground by measuring air shower. For the spectrum shown in Figure 6, there are bends at $E \sim 10^{15.5}$ eV and $E \sim 10^{19}$ eV, called *knee* and *ankle*. The cosmic ray flux over ankle is about 1 /km^2/year. Therefore, the detector which has very large detectable area is required to detect ultra high energy cosmic rays whose energy is higher than 10^{19} eV.

In order to determine energy spectrum for ultra high energy cosmic rays with enough statistics, large exposure observatory is required.

1.2 Observation method by air shower

1.2.1 Surface Array Particle Detector(SD)

The method by SD takes place by many particle counters arrayed on the ground. They record the number of particles and the particle arrival timing for each arrayed coordinates. From those information, the arrival direction and the energy of cosmic rays are estimated. The air shower caused by UHECRs has a swarm of many particles whose shape is a disk perpendicular to shower axis. The disk-shaped swarm of particles flies with almost light speed and hit the ground. The thickness of the disk-shaped swarm is about a few microsecond. The radius of the disk-shaped swarm is about a few kilometer for UHECRs. Each particle detector generates signals proportional to the number of particles which hit the detector. This schematic is shown in Figure 7. Therefore, the number of particles for each position is estimated from the signal size. The direction of the air shower axis is estimated from the difference of particle arrival timing for each position.

Basically, the surface particle detector detects charged particles. However, there are methods to absorb electron and positron by lead, iron or cement. On the other hand, by those materials, there are methods to increase the charged particles such as electron and positron which are generated from γ ray.

The energy of primary particle is estimated by comparison between the number of particles at each position and air shower simulation for each shower direction.

The method using surface array particle detector contains the air shower simulation to determine the primary particle energy. Therefore, there are systematic errors which come from unknown primary composition and unknown hadronic interaction model of shower simulation for energy determination. However, the surface array particle detectors are stable observational equipment and observe continuously with constant detectable area.

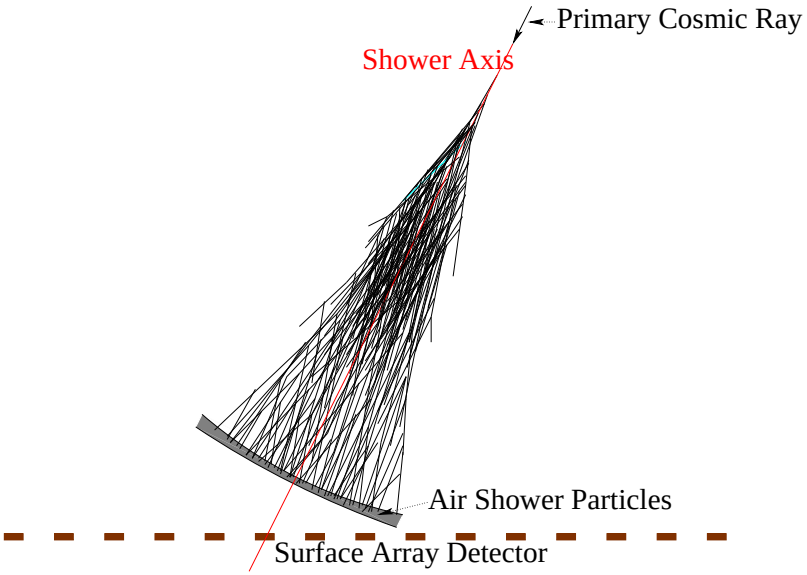

Figure 7: Observation by surface detector array

Akeno Giant Air Shower Array

AGASA experiment took place in Yamanashi, Japan [15]. It consists of 111 scintillation counters(2.2 m^2) and 27 muon detectors in 100 km^2 area. There are 156 scintillation counters(1.0 m^2) and 11 muon detectors in 1 km^2 area, which are used previously to AGASA, which is for lower energy cosmic rays. This relatively small array serves continuous observation for low energy region of AGASA. The energy spectrum of AGASA from 1991 to 2002 is Figure 8 [16]. The dashed line is a prediction spectrum of uniform cosmic ray source in extra galactic region. In Figure 8, AGASA result supports no suppression by GZK effect. The event sky map of AGASA is Figure 9 [17] and the separation angle distribution is Figure 10 [17]. The method to get separation angle distribution is counting pairs over energy threshold events for opening angle bins. This detail is described later.

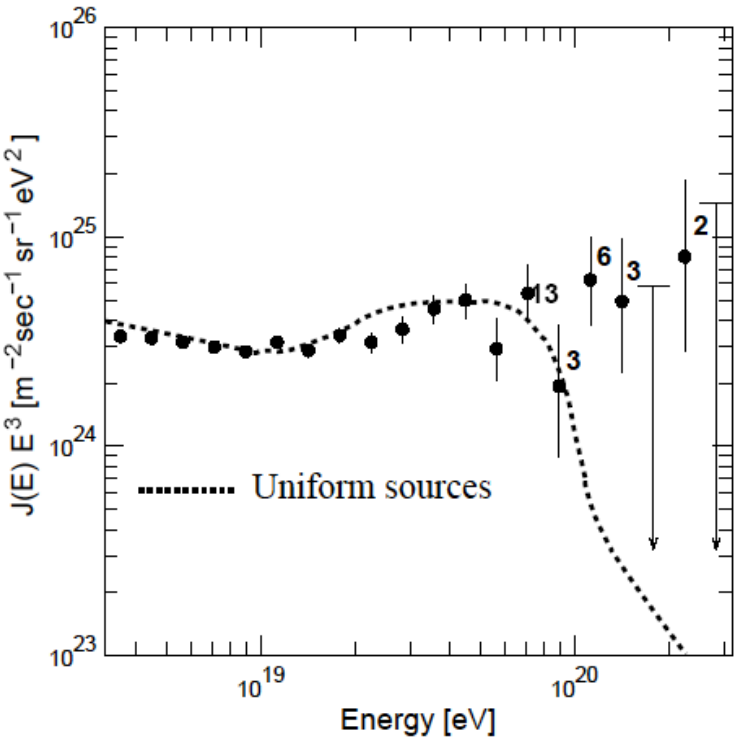

Figure 8: Energy spectrum by AGASA [16].

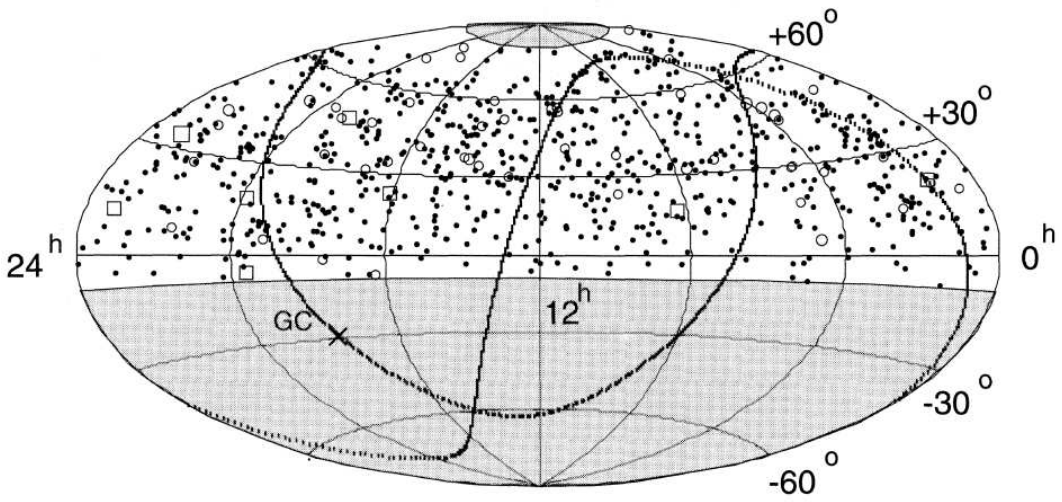

Figure 9: Event sky map by AGASA over 10 EeV events in equatorial coordinates [17].

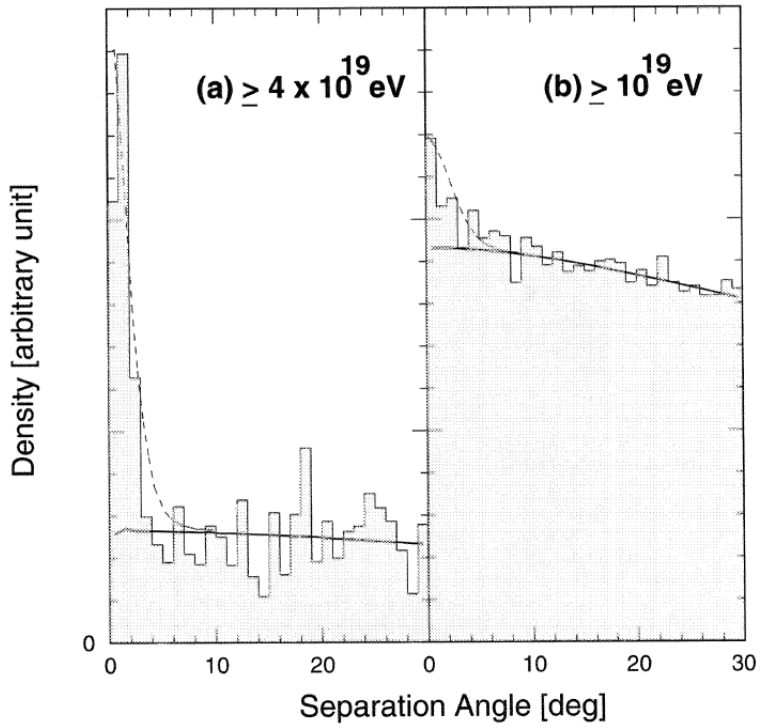

Figure 10: Separation angle distribution by AGASA [17]. Solid line: averaged separation angle distribution from isotropic model. Histogram: observed separation angle distribution.

1.2.2 Atmospheric Fluorescence Telescope(FD)

The method by FD takes place by telescopes for observing the atmospheric fluorescence photons which are induced by air showers. The direction is estimated from the track of fluorescence, the energy is estimated from the brightness. Charged particles in air shower excite nitrogen molecules in the atmosphere. The excited nitrogen molecules emit the light and the main wavelength is 300 nm $\sim$ 400 nm. The light emission efficiency in the atmosphere for electrons is 4$\sim$5 photon/meter/electron. The atmospheric fluorescence attenuates by the atmosphere between an emission point and an observational point. When the distant fluorescence telescopes observe the same region of same shower, the shower axis is estimated by combination of tracks for each telescope. Even if a shower is detected by one telescope, the shower axis is estimated from the signal width for each pixel and the difference of signal timing between the pixels. Once a shower axis is determined, the distance to the shower axis and the length of the shower axis are determined for each pixel.

The number of charged particles of each point on shower axis is estimated by the signal size of each PMT with atmospheric attenuation and fluorescence efficiency. The variation of the quantity of fluorescence along the shower axis represents the development of air shower. The total amount of the charged particles is converted to primary energy.

The energy estimation by the method using atmospheric fluorescence telescope is not affected by hadronic interaction model basically, because the energy is estimated from total number of shower particles. In addition, it can observe the development of air showers, therefore, the primary composition is estimated by the shape of shower development. However, the observation takes place only in dark night, and the status of the atmosphere is not stable. Therefore, there is systematic error from atmospheric attenuation for energy estimation.

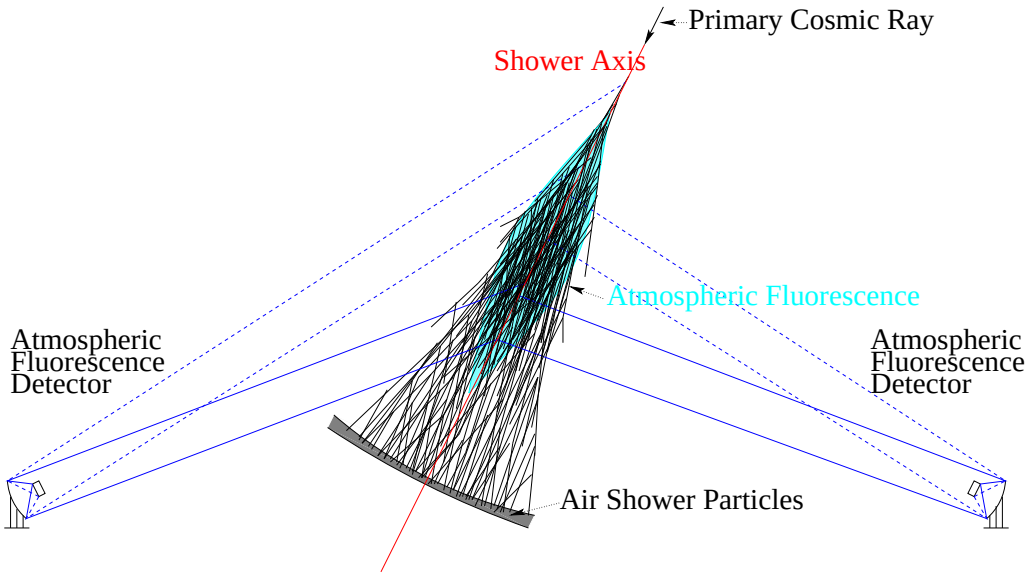

Figure 11: Observation by atmospheric fluorescence telescope.

High Resolution Fly's Eye

HiRes experiment took place in Utah, USA [19]. It consists of 2 fluorescence telescope stations, which are spacing 12.6 km. (HiRes-I, HiRes-II) The field of view of one telescope is 16° in azimuth, 14° in elevation. The camera consists of 256 hexagonal PMTs which has ∼40 mm in apothem. The spherical mirror area is 3.8 m^2 for one telescope. HiRes-I consists of 21 telescopes, whose field of view is 360° in azimuth, 3°-17° in elevation. HiRes-II consists of 42 telescopes, whose field of view is 360° in azimuth, 3°-31° in elevation. The energy spectrum of HiRes-I from 1997 to 2005 and HiRes-II from 1999 to 2003 is Figure 12 [20]. HiRes result supports the suppression by GZK effect. The event sky map is Figure 13 [21]. The X_{max} average and deviation for each energy is Figure 14 which is for primary mass composition study [22].

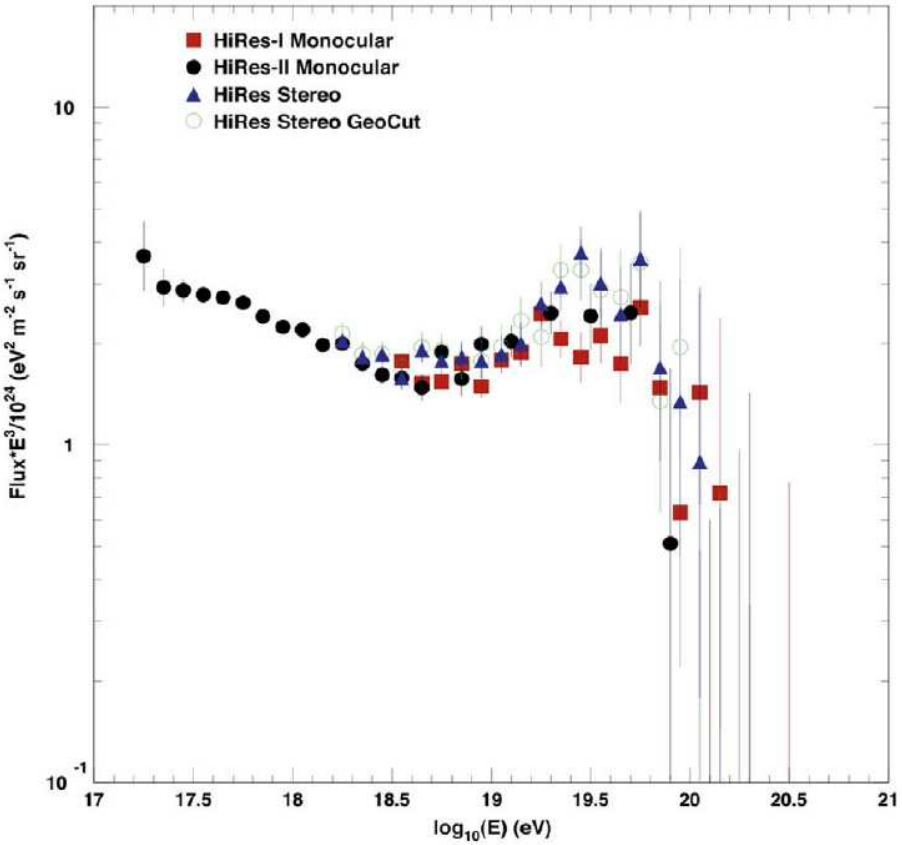

Figure 12: Energy spectrum by HiRes [20].

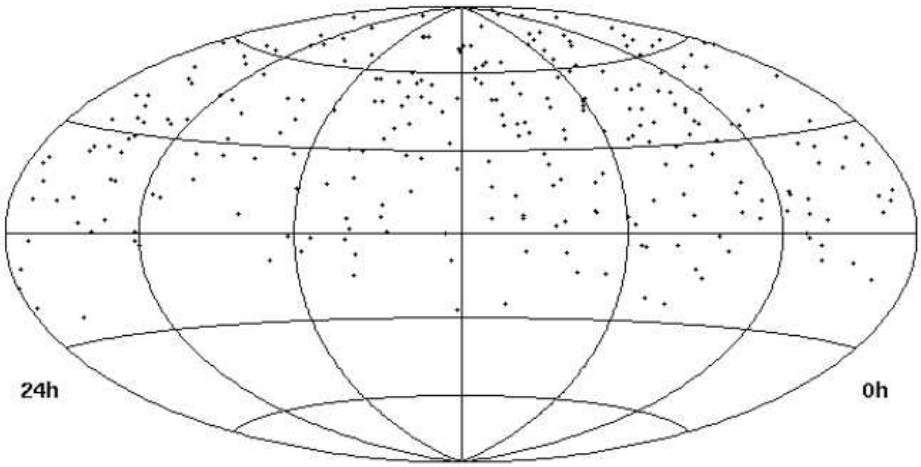

Figure 13: Event sky map by HiRes over 10 EeV events in equatorial coordinates [21].

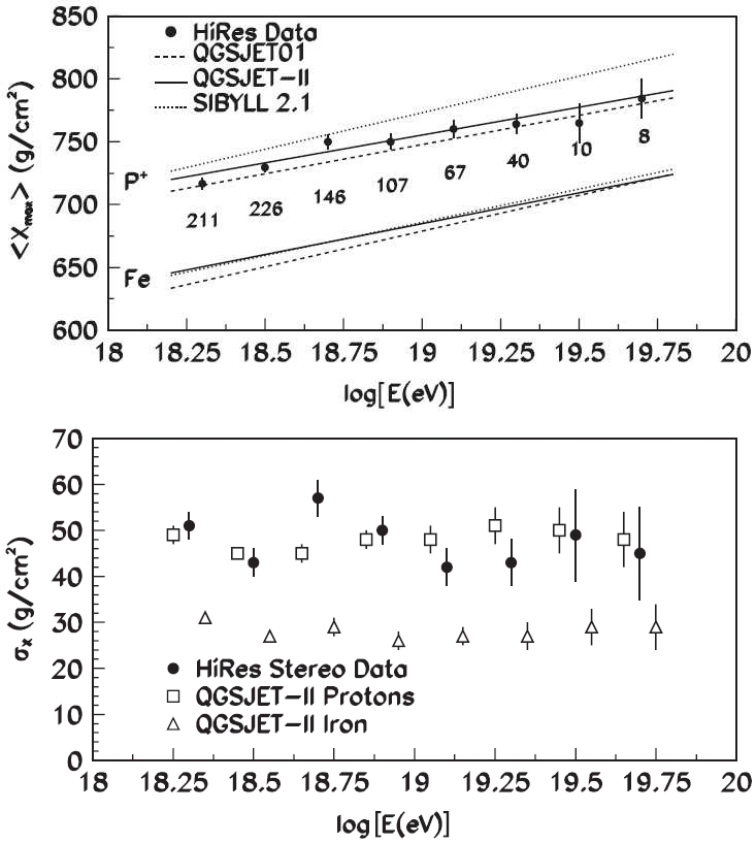

Figure 14: X_{max} distribution for each energy bin by HiRes with simulation result whose primary mass composition is proton and iron [22].

1.2.3 Hybrid Observation

The methods by either particle detector surface array or atmospheric fluorescence telescope have advantage and disadvantage each other. In addition, the results of energy spectrum and small cluster search are different for AGASA and HiRes. If same shower is observed by both SD and FD, the SD shower reconstruction can use the development of shower observed by FD, the FD shower reconstruction can use the position of shower axis on the ground by SD. Therefore, the hybrid observation can raise the determination accuracy for energy and direction more than the accuracy by the single species observation.

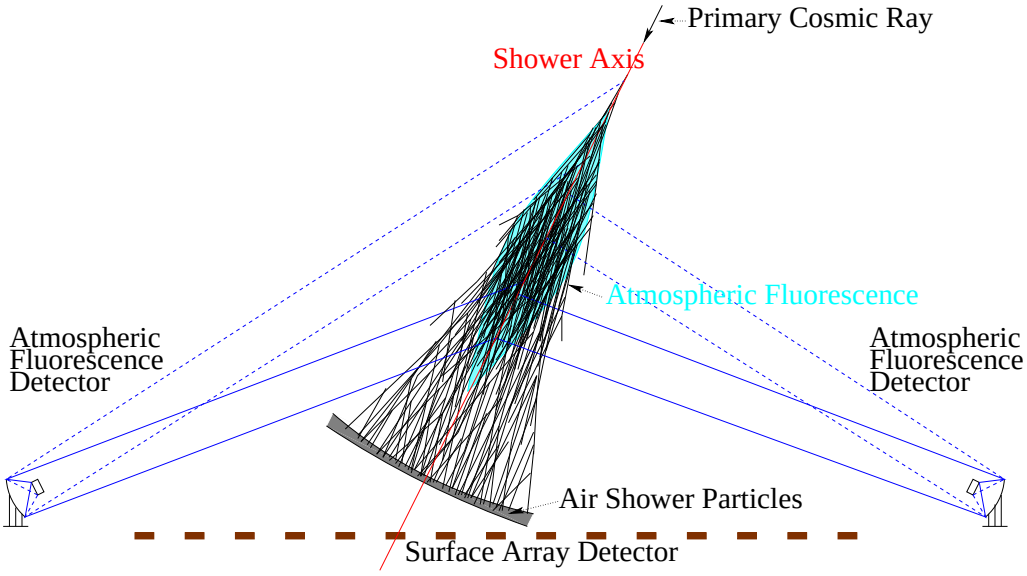

Figure 15: Observation by hybrid of SD and FD

Pierre Auger Observatory

Pierre Auger experiment takes place in Mendoza, Argentina [23]. It consists of 4 fluorescence telescope stations and 1600 water Cherenkov counters (10 m^2). 1600 SDs are deployed in a triangular grid with 1.5 km spacing. The field of view of one telescope is 30° in azimuth, 28.6° in elevation. The camera consists of 440 hexagonal PMTs. The spherical mirror area is 3.5 m × 3.5 m for one telescope. Each FD station contains six telescopes. The energy spectrum of Auger from 2005 to 2008 is Figure 16 [24]. Auger result supports the suppression by GZK effect. The event sky map is Figure 17 [25]. The X_{max} average and deviation for each energy is Figure 18 which is for primary mass composition study [26].

Telescope Array

Telescope Array experiment takes place in Utah, USA. Details are on next section.

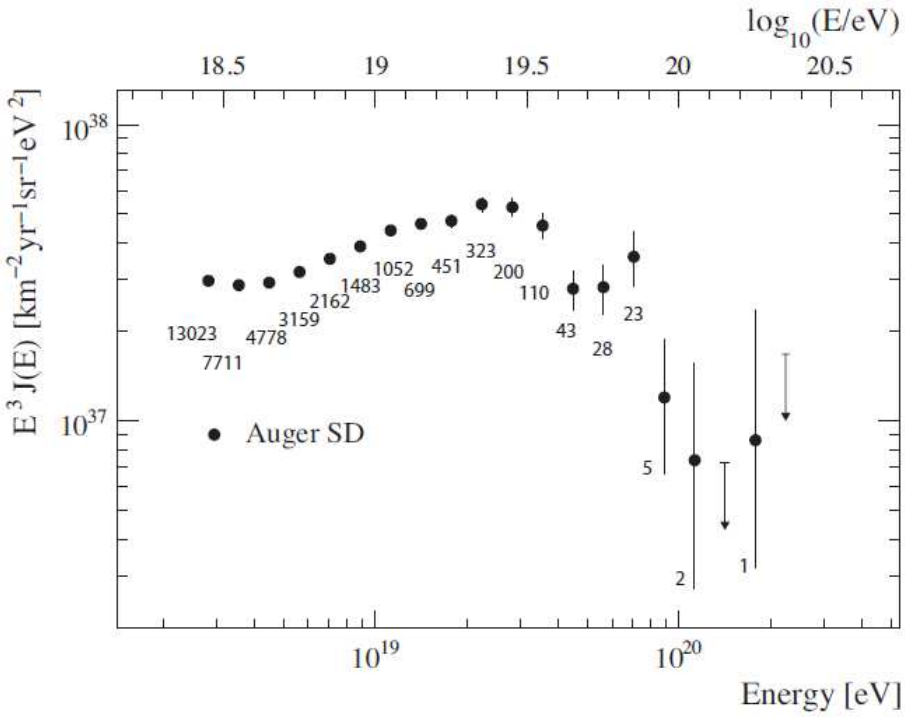

Figure 16: Energy spectrum by Auger [24].

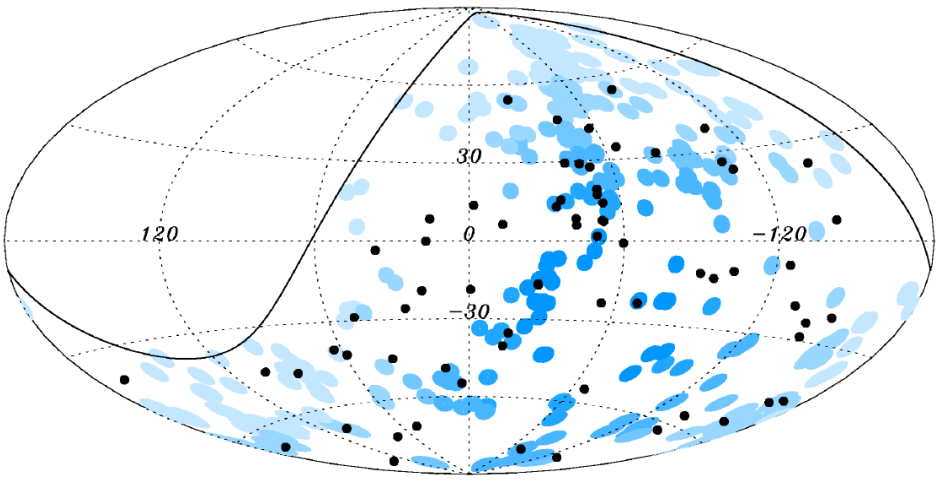

Figure 17: Event sky map by Auger over 55 EeV events in galactic coordinates. Blue point is AGN within 75 Mpc. The radius of blue point is 3.1° [25].

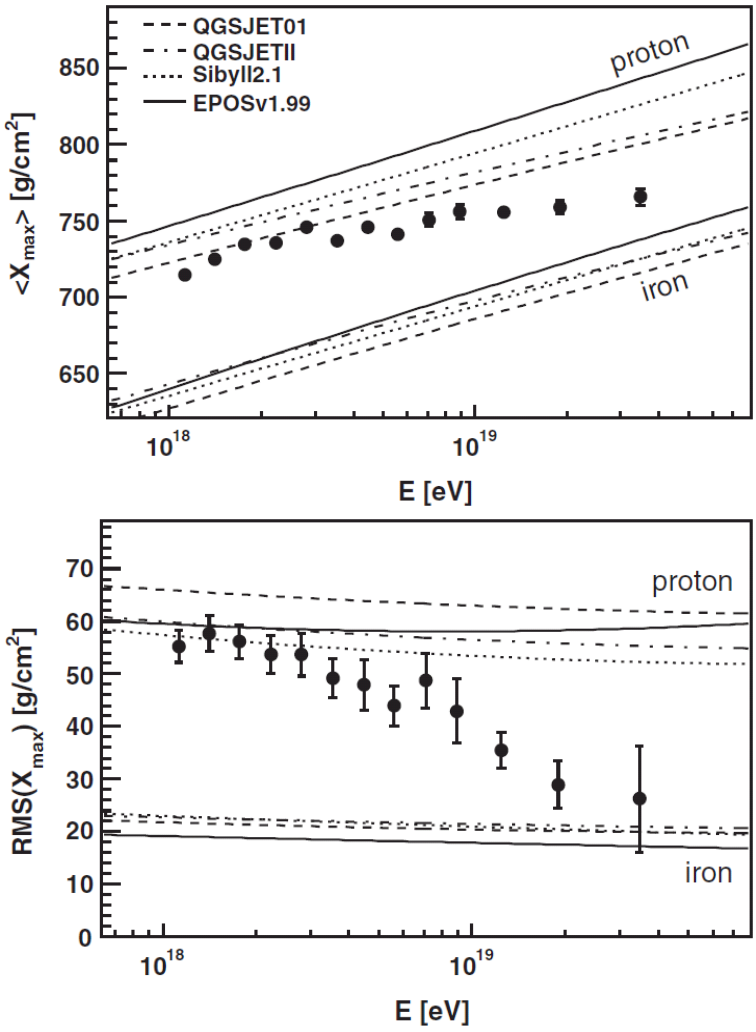

Figure 18: X_{max} distribution for each energy bin by Auger with simulation result whose primary mass composition is proton and iron [26].

2 Telescope Array Experiment (TA)

The Telescope Array experiment is hybrid observation for air shower caused by cosmic ray whose energy is greater than $10^{18.5}$ eV. This experiment takes in Millard County, Utah, United States. (39.3°N, 112.9°W, altitude 1382 m) Major construction of the Telescope Array experiment started in 2005. The TA consists of 3 atmospheric fluorescence detector stations, 507 surface array particle detectors, the central laser facility, the electron light source and 3 telecommunication towers. SDs are deployed in a square grid of 1.2 km spacing(Figure 19).

There are 12 telescopes in each station at Black Rock and Long Ridge (BRFD and LRFD). Each station covers $3° \sim 33°$ in elevation and 108° in azimuth. In addition, there are 14 telescopes at Middle Drum (MDFD), which come from HiRes-I. MDFD covers $3° \sim 31°$ in elevation and 114° in azimuth. By using MDFD, TA is directly comparable with HiRes energy scale. SD is 2 layers plastic scintillation detector, which covers 3 m^2. And data collection takes place through 3 telecommunication towers.

By hybrid observation with FD (partly from HiRes) and SD (plastic scintillator), Telescope Array experiment verifies whether the difference between AGASA and HiRes energy spectrum comes from observation method or not. TA determines the energy spectrum with high accuracy by hybrid observation or SD observation calibrated by FD energy. By FD stereo or hybrid observation, the mass composition study takes place. In addition, anisotropy study takes place by SD observation.

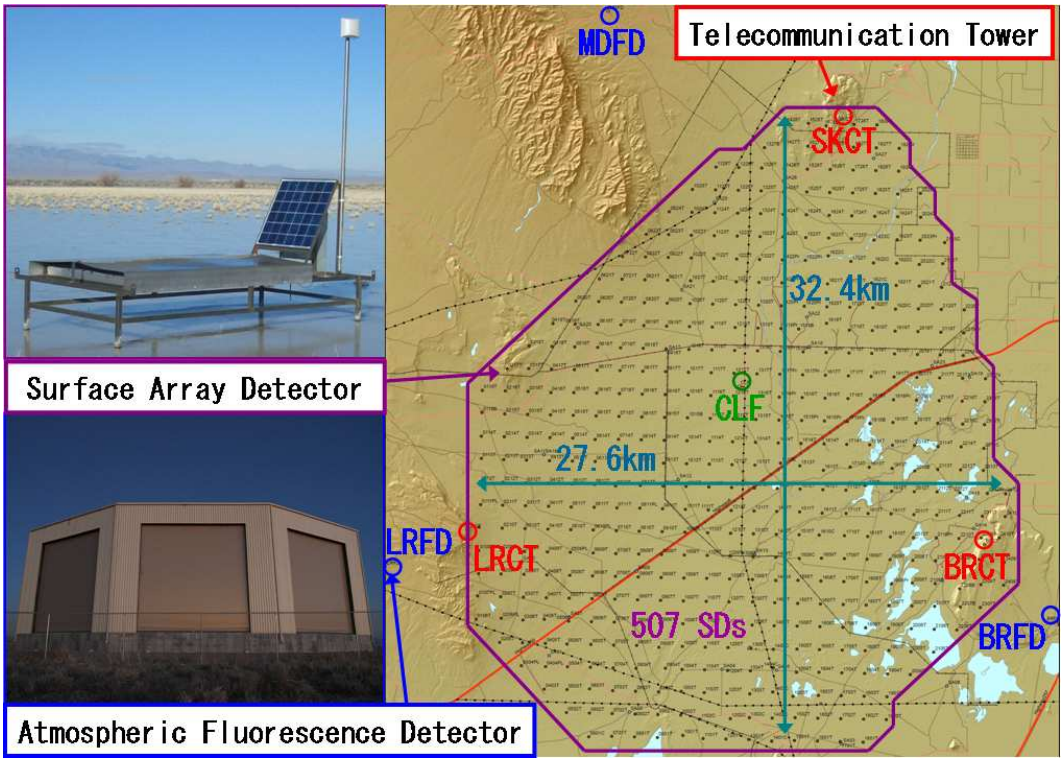

Figure 19: TA site over view [27]

2.1 Fluorescence Detector (FD)

FD consists of fluorescence telescopes and many kinds of calibration devices.

2.1.1 Fluorescence Telescopes (BRFD, LRFD)

The FD telescope for BRFD and LRFD is 3.3 m diameter spherical mirror telescope which is divided by 18 segment mirrors. The camera of telescope consists 256 PMTs whose field of view is 18° in azimuth and 15° in elevation. The PMT is 6 cm diameter and hexagonal photo cathode with 8 dynodes. There are 12 telescopes (6×2) in one FD station, and one station covers 3° ∼ 33° in elevation and 108° in azimuth. The observation started in November 2007.

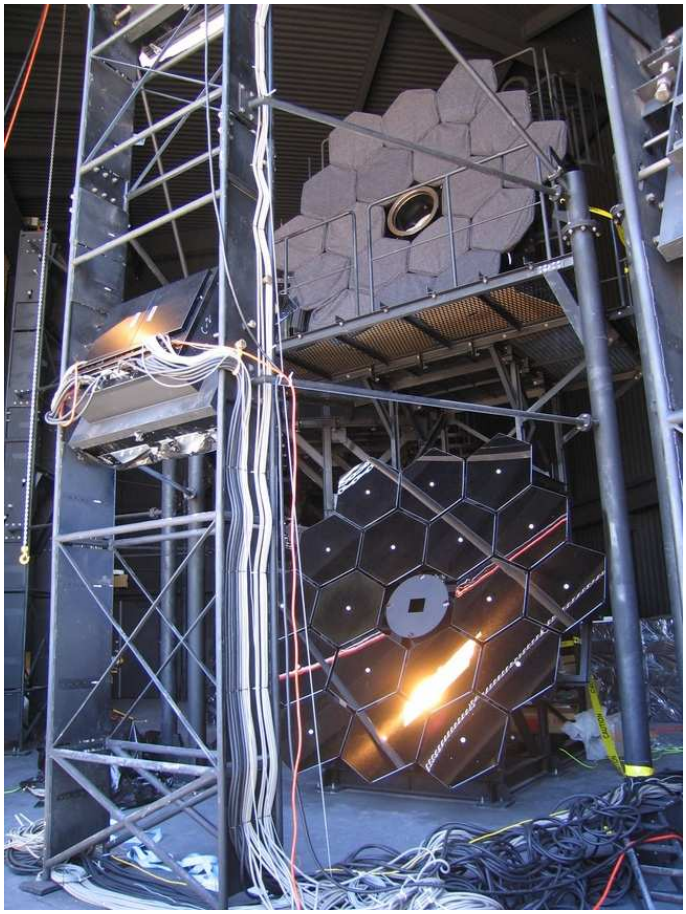

Figure 20: Fluorescence telescope in BRFD station

The reflectance of mirrors for same 4 telescopes are measured every one or two month for monitoring the time variation of reflectance. For each telescope, the reflectance of lower side segment mirrors goes down more than the reflectance of higher side segment mirrors with time. Mirror washing takes place once or twice a year to recover the reflectance. The individual difference of the reflectance of mirror is almost within ±1%. There are two types of UV transparent filter for PMT camera. One is for each PMT and the other is for

each camera. The individual difference of the transmittance of filter of each camera is smaller than 3%. The gains of some standard PMTs for camera are calibrated in laboratory by CRAYS. CRAYS is scattering light by pure nitrogen molecule, whose light source is nitrogen laser. The absolute intensity error is about 5%. These PMTs have a stable small light source which is on photo cathode called YAP pulsar to follow the gain changing of standard PMTs hourly. In addition, there is a xenon diffusing flasher for each camera. This is on the center of mirror and is used for non-standard PMTs to adjust relative gain to standard PMTs. This xenon flashing is done hourly [29]. The signal for each PMT is read by 12bit 40 MHz FADC.

2.1.2 Fluorescence Telescopes (MDFD)

The FD telescope for MDFD is 2 m diameter mirror telescope which is divided by 4 segment mirrors. and The camera of telescope consists of 256 PMTs whose field of view is 16° in azimuth and 14° in elevation. The PMT is 2 inch diameter. There are 14 telescopes (7×2) in one FD station, and one station covers 3° $\sim$ 31° in elevation and 114° in azimuth. The sensitivity of the telescope is monitored by UVLED. The observation started in December 2007 [28].

Figure 21: Fluorescence telescope in MDFD station

2.1.3 LIght Detection And Ranging, Central Laser Facility and Portable Laser

There is a LIDAR system at BRFD. This system measures the atmospheric transparency by the reflection of YAG laser, whose wavelength is 355 nm. The laser shots horizontally and vertically in two type of energy with 1 Hz. Therefore, four sets of shots take place and one set has 500 shots. This device has 30 cm diameter telescope with a UV filtered PMT to measure the light intensity and timing of back scattering laser by atmospheric molecules. This

measurement takes place before and after FD observation per night. The atmospheric transparency is measured by the difference between real data and pure atmosphere as a function of the light intensity and the height. The observation started in September 2007 [30].

Figure 22: LIDAR and BRFD station (right building).

There is the central laser facility (CLF) at the center of TA site, almost equidistant from three FD stations. This system also measure the atmospheric transparency by the reflection of YAG laser, whose wavelength is 355 nm. The laser shots vertically with 10 Hz. One set of shots has 100 shots. This light is used as a standard light source for each FD stations and can be used to measure the atmospheric transparency which changes in a short time. The observation started in December 2008 [30]. In addition, there is a vertical LIDAR system by two PMTs for different height range.

Figure 23: CLF (right). Solar-battery system (left back) is used to control and monitor. Liquefied petroleum gas generator (left front) whose controller is powered by solar-battery and switched remotely, is used to laser module and air conditioning.

The portable laser system is made to calibrate different telescopes and to

measure atmospheric transparency like CLF at different distance from FD. The laser is same as LIDAR and shot energy is calibrated at ELS site or CLF site for each purpose.

2.1.4 InfraRed Camera and Weather Code

There is an infrared camera at BRFD. The sensitive wavelength range of this camera is $8 \sim 14$ μm. The field of view of this camera is $25.8^\circ \times 19.5^\circ$, whose data is stored in 320×236 pixels. 14 pictures are taken hourly. twelve of them are directed to the sight of FD telescopes. one is directed to horizon and one is directed to vertical. This data can be used to measure the total amount of cloud in the field of view for FD telescopes. The infrared camera observation started in December 2007 [31].

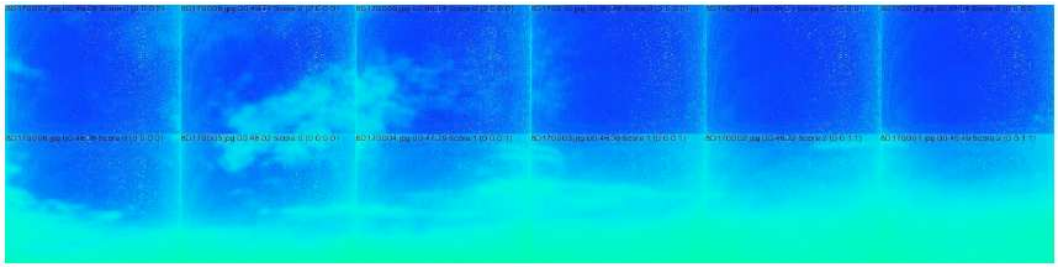

Figure 24: Example twelve pictures of IR camera [31].

The weather code is also cloud monitor by eye from HiRes. This is defined whether stars can be seen or not, for north, south, east, west, vertical. This data can be also used to measure the total amount of cloud.

2.1.5 Electron Light Source

There is the electron linear accelerator at BRFD. The accelerated electrons are bent to vertical in 100 m front of telescope. For FD, these electrons can be seen as a pseudo air shower which is measured without unstable atmospheric transparency. Therefore, this electron beam pulse is used to directly calibrate fluorescence telescope and atmospheric fluorescence efficiency. The beam pulse is about 40 MeV 10^9 electrons at 100 m from FD, which is scaled to the air shower of $E = 10^{20}$ eV at 10 km from FD. By the test operation in Japan, the accuracy of electron energy is less than 1% and the beam current can be measured in $\pm 6\%$ [32].

2.2 Surface Detector (SD)

SD consists of many particle detectors and control tower. They are operated by solar battery system with wireless LAN because all components are deployed in large area with spacing long distance.

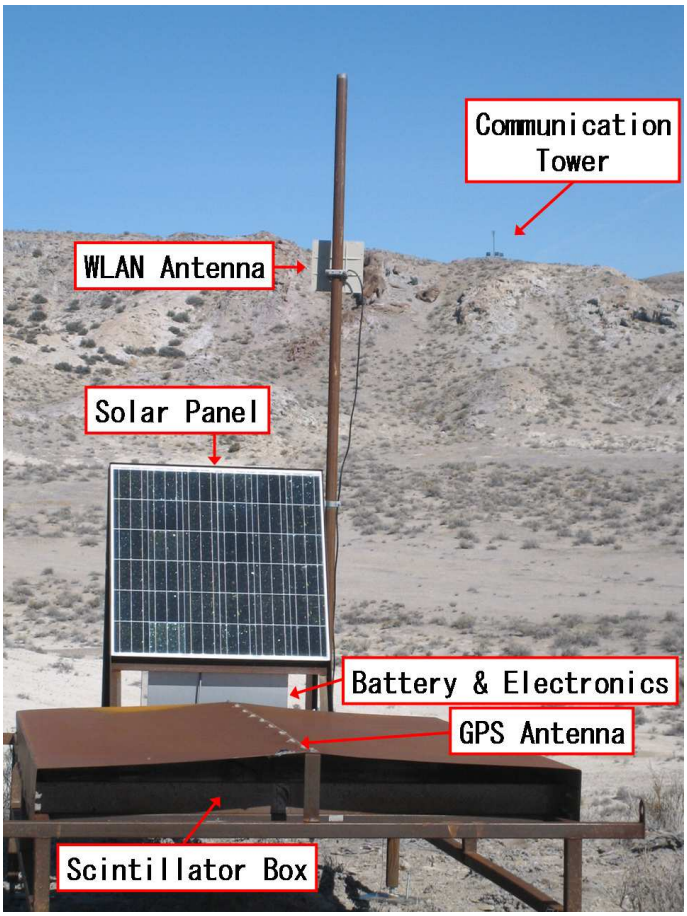

Figure 25: Surface detector and telecommunication tower.

2.2.1 Particle Detection Part

The particle detection part is in a SUS box which size is 230 cm south-north, 170 cm east-west, 10 cm height. It is optically separated 2 layers 3 m^2 detector, using 16 plastic scintillator sheets (150 cm $\times$ 25 cm $\times$ 1.2 cm) produced by CI and 220 wavelength shifting fiber (WLSF) (1 mmϕ $\times$ 500 cm) produced by KURARAY. Each scintillator sheet has 13 grooves on one side to store WLSF in 2 cm spacing. WLSFs are stored for whose both edges are equidistant from scintillator and gathered to PMT for each layer. Figure 26 and Figure 27 is the partial sectional view and overview.

Gathered WLSFs are fixed by fiber holders. The edge of WLSFs are polished and attached to the PMT with silicone grease produced by Shin-Etsu Chemical. Each layers are wrapped by 2 Tyvek sheets which is nonwoven fabrics produced by DuPont. 1 mm thickness SUS sheets is between 2 layers and 5 mm styrofoam is on the bottom of the box. There are 2 PMTs (9124SA) and

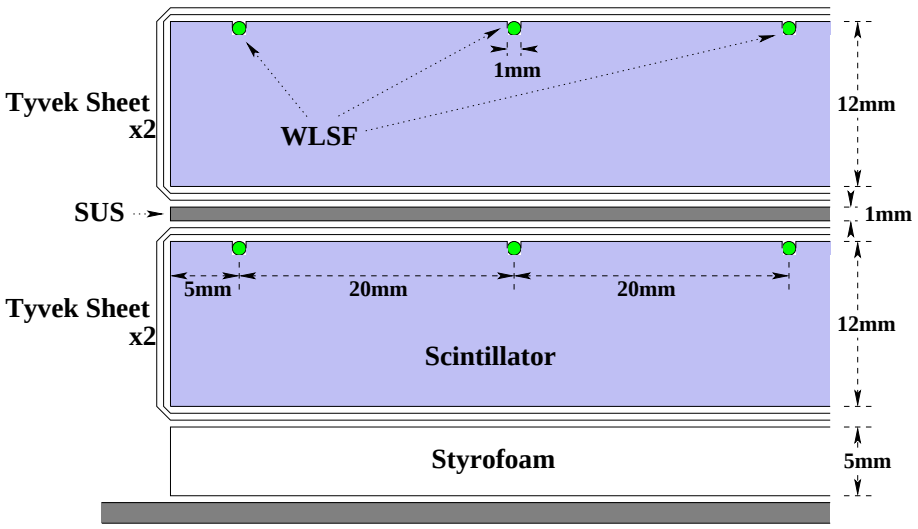

Figure 26: Partial sectional view of particle detection part.

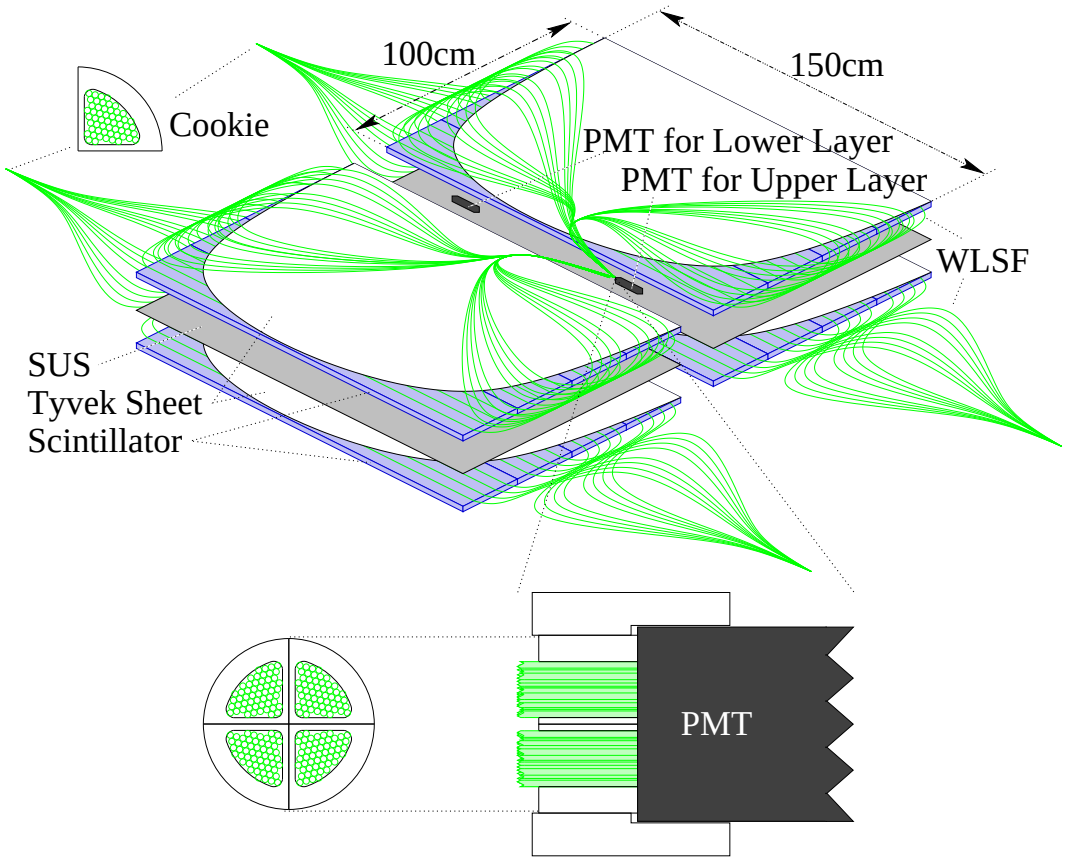

Figure 27: Overview of particle detection part.

power sockets of PMT (Modified PS1806/12F) for each layer are produced by Electron Tubes.

2 LEDs (470 nm peak produced by NICHIA) are installed to check the linearity of PMT for each layer, total 4 LEDs. There are thermometer and hygrometer at the center of the box. In addition, there are some clasps to fix scintillators for transportation including helicopter.

2.2.2 Electronics and Data Acquisition System

The electronics consists of Main board, charge control board, WLAN board and GPS board in electronics box and switch board in tuckerbox.(Figure 28)

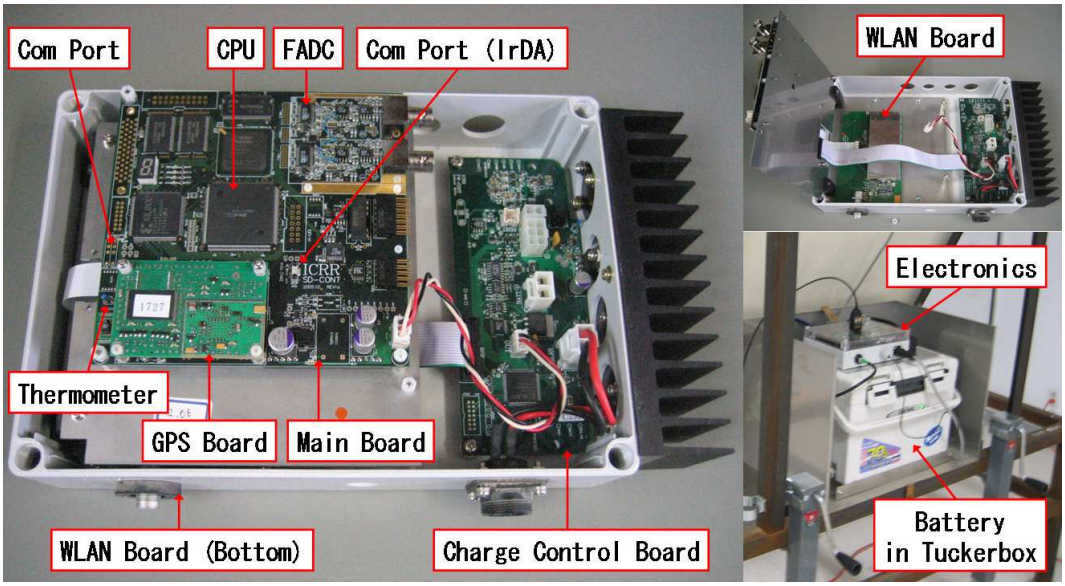

Figure 28: Electronics for surface detector.

The signal from PMT is read out by 12bit 50 MHz sampling FADC. 1pps resolution from GPS is about 20 ns. WLAN is on 2.4 GHz band. For WLAN, either parabolic antenna or plane antenna are chosen by distance to tower for detector. Omnidirectional antenna is used for tower. The solar panel is set for 30° elevation and generates 120 W, produced by KYOCERA. The capacity of battery is 12 V 100 Ah, produced by DYNASTY. It is installed in tuckerbox to avoid low temperature which decreases the battery capacity. Telecommunication towers are also activated by solar battery system whose charge controller is produced by Morningstar. Each telecommunication tower is linked by WLAN on 5.7 GHz band.

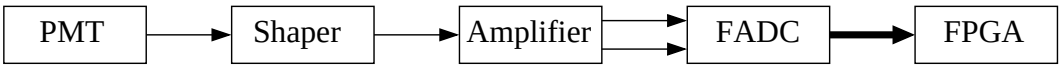

Figure 29: Digitalization of PMT signal.

The diagram of the front-end of PMT signal digitalization is shown in Figure 29. The shaper dulls the PMT signal for 50 MHz sampling FADC. The

amplifier is used as a single-ended-to-differential amplifier for FADC.

The DAQ procedure starts level0 trigger. The upper layer PMT is connected to Ch.1 and the lower layer PMT is connected to Ch.2 for electronics. The level0 trigger is coincidence trigger of both layers. When sum of continuous 8bins in FADC waveform is over 15 from sum of pedestal 8bins for both layer, the level0 trigger is generated. If the level0 trigger is generated, 128bin FADC waveform is stored, whose waveform contains level0 trigger point as 30th bin.

Then, level1 trigger is generated from stored level0 triggered waveform. When sum of 128bin FADC waveform is over 150 from sum of pedestal 128bins for both layer, the level1 trigger is generated. If the level1 trigger is generated, the trigger information tables are stored. This trigger table contains the triggered timing as integer in microsecond.

The level1 trigger tables are collected by tower electronics. The tower system generates level2 trigger (shower trigger) when there are trigger tables from 3 adjacent SD within 8 us width. The tower electronics collects waveform from all SDs in ± 32 us from triggered time.

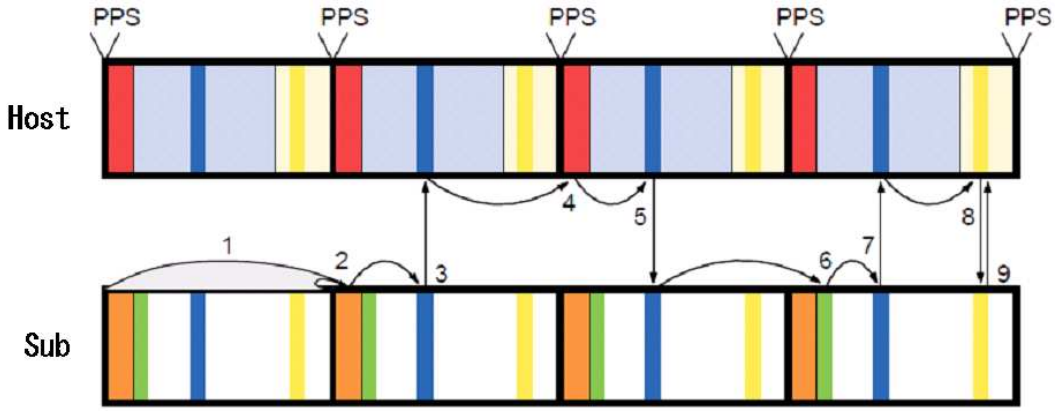

Figure 30: SD DAQ flow [33]. Host: Electronics at telecommunication tower. Sub: Electronics at arrayed each SD.

The DAQ flow in four seconds is described in Figure 30. The PPS is generated by GPS board, 1 pulse per second. All Host and Sub Electronics are synchronized by this pulse. Each process of number in Figure 30 is described here.

1. generate level0 trigger and store waveform [Sub]
2. generate level1 trigger table [Sub]
3. send level1 trigger table [Sub]
4. search level2 trigger [Host]
5. send level2 triggered time for searching waveform [Host]
6. search waveform [Sub]

7. send the number of waveforms which are searched [Sub]

8. request the waveform [Host]

9. send the waveform [Sub]

For detector control and DAQ, SD array is divided into 3 area by 3 towers. The data is stored in USB memory on the one board PC in the tower platform. The data is transferred twice a day to storage server in Delta. The data is compressed and burnt to 3DVDs (Delta, Salt Lake City, Kashiwa). In addition, after burning 3DVDs, the tower data is deleted to free the space of USB memory.

2.2.3 Construction, Running and Offline Calibration

The practical development of TASD started in 2004 and major construction started in 2005. The particle detection part of SD was assembled in Japan. Averagely, 3 scintillator boxes are assembled a day. The whole SD was finally assembled in Delta, Utah, near the observation site. The particle detector components are gathered to steel platform produced by T&D Maintenance. Total weight is about 400 kg. They are transported by trailer to the temporary front-line base, and deployed by helicopter. In 2007, WLAN antenna adjustment, basic calibration, development of the firmware of electronics and DAQ program were performed. The SD DAQ started in March 2008. PMT gain tuning was done in May. Therefore, the SD analysis uses the data from 2008/05/11. The cross boundary trigger for 3 tower sub-arrays was installed at the end of 2008.

The SD DAQ is continuously running well from 2008/05/11.

There are some offline calibrations mainly to remove initial failure of PMT, power socket and electronics.

One of the major offline calibration except for removing initial failure is the PMT linearity measured by LED in scintillator box. This calibration was done for all SDs in Delta, Utah, before deployment. This result is consistent with online MIP linearity. And these informations are used for signal saturation flag (5 % decrease from linear) for event reconstruction.

The other major offline calibration except for removing initial failure is the resolution of relative waveform timing in different SDs and position accuracy. This details are described on Appendix.

2.2.4 Online Calibration, Monitoring and Maintenance

There are some online monitor calibrations.

- Every Second
  - Time-stamp in 600 seconds (cyclic in 10 minutes)
  - Clock count between 1pps (50MHz clock)
  - Number of level1 triggers

- Every minute
  - Number of level0 triggers
  - Number of level1 triggers
  - Some DC voltages as sum of 1Hz sampling
  - Humidity and some temperatures as sum of 1Hz sampling
  - Battery voltage as sum of 1Hz sampling
  - Solar panel voltage as sum of 1Hz sampling
  - Charging current as sum of 1Hz sampling
- Every 10 minutes
  - Pedestal histogram
  - Level0 histogram
  - Pulse height linearity histogram
  - Pulse charge linearity histogram
  - Number of tracking GPS satellite and health of GPS

By using these monitor data, maintenance and reconstruction takes place. If there is lack of monitor information by bad communication status between Host and Sub, some interpolations and extrapolations are done for saving waveform as much as possible for reconstruction.

The conversion factor from energy deposition in scintillator to FADC count is obtained by the pedestal histogram and the level0 histogram (MIP histogram), stored every 10 minutes. In electronics, the pedestal value is treated as sum of 8bins because level0 trigger is judged by sum of continuous 8bins. For the pedestal histogram, FADC count is calculated as sum of 8bins which does not overlap another 8bins and cover the 50Mbins in a second. The pedestal histogram is shown in Figure 31. For the level0 histogram (MIP histogram), FADC count is calculated as sum of previous 4bin and following 8bin for level0 triggered bin, total 12bins. The level0 histogram is shown in Figure 32. In the original design, the peak of MIP histogram was set to 50. Therefore, level0 trigger (over 15) was equivalent to 0.3MIPs and level1 trigger (over 150) was equivalent to 3MIPs. For practical DAQ operation, the peak of level0 histogram (MIP histogram) is currently set to ~ 45 by high voltage adjustment for PMT gain. This is shown in Figure 33. However, the trigger condition is kept in FADC count. The conversion factor is obtained from these histogram by fitting with energy deposition histogram by Geant4 [34].

The triggered timing for each SD is stored as a clock count from 1pps of GPS, called "TrigClock". The clock speed is 50 MHz. So, simply, clock count $\times$ 20 ns is the triggered time. However, the clock speed varies and different individually. The clock count between 1pps is called "MaxClock". Therefore, the triggered time is obtained as TrigClock/MaxClock s. The variation of MaxClock is shown in Figure 34. The particle arrival timing is obtained by FADC waveform analysis, described on next section.

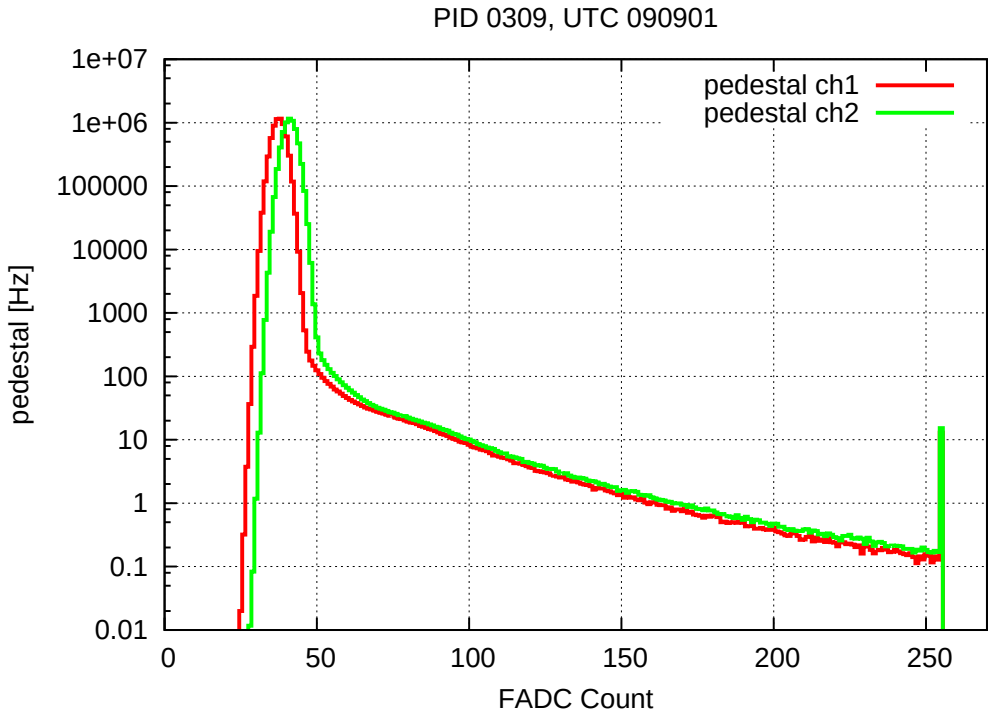

Figure 31: FADC pedestal histogram of 8bins sum.

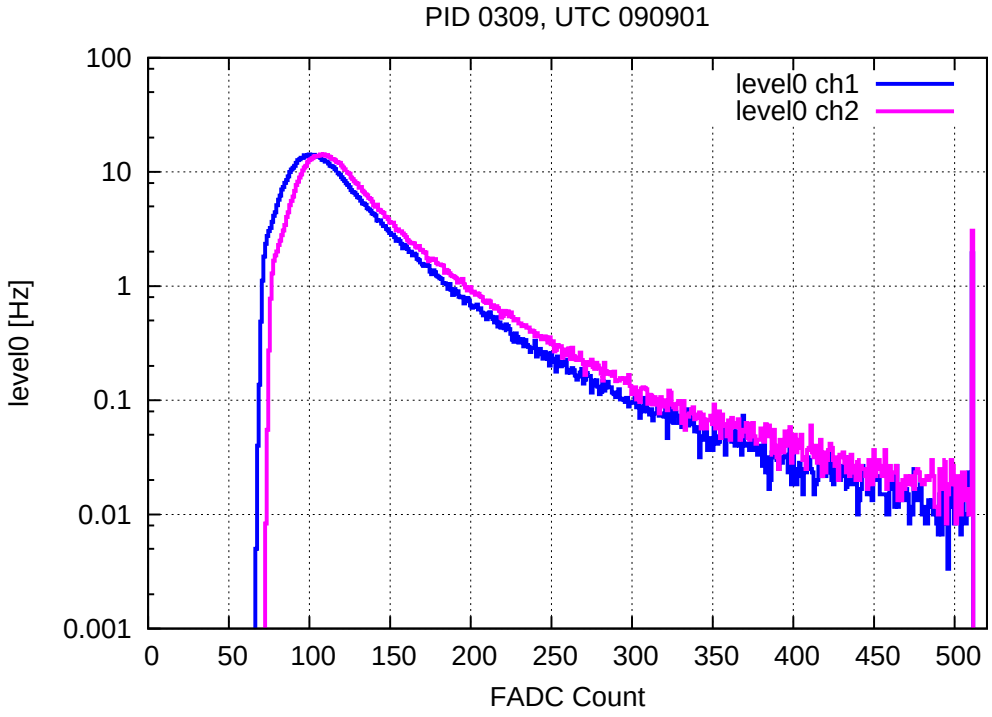

Figure 32: FADC level0 histogram of 12bins sum.

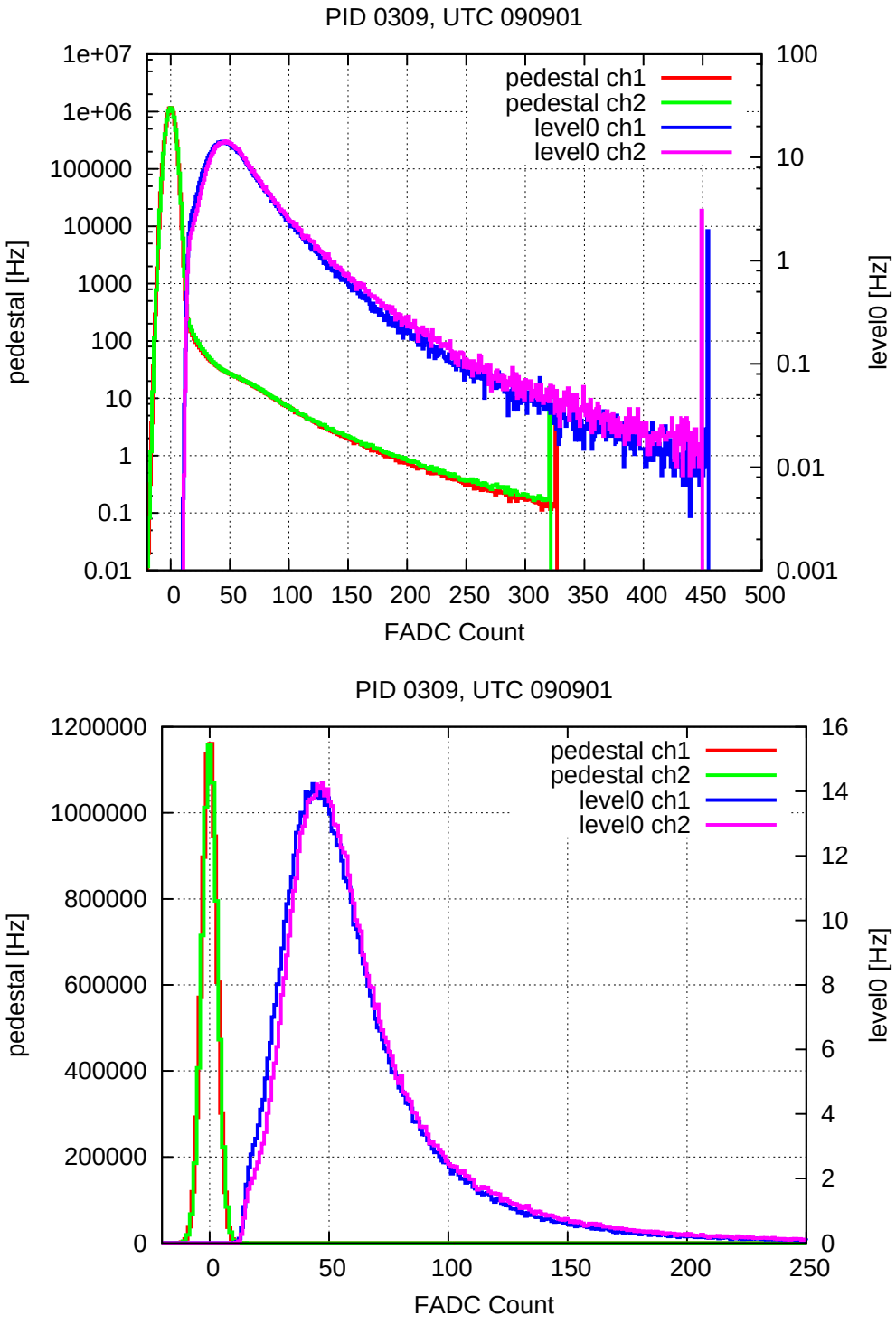

Figure 33: Pedestal histogram scaled to 12bins sum, and then, pedestal and level0 histogram moved for the pedestal peak to 0.

The shift person monitors the DAQ running status everyday. Mainly, there are three kinds of monitoring. One is checking current DAQ is running or not and transferring data correctly or not. Another is inter tower WLAN connection is enough or not for DAQ. The other is monitoring the health of individual SD. The sample plot for monitoring individual SD is shown in Figure 35.

By the monitor data, the shift person maintains the towers and detectors. Most of this work is rebooting electronics or exchanging electronics and battery.

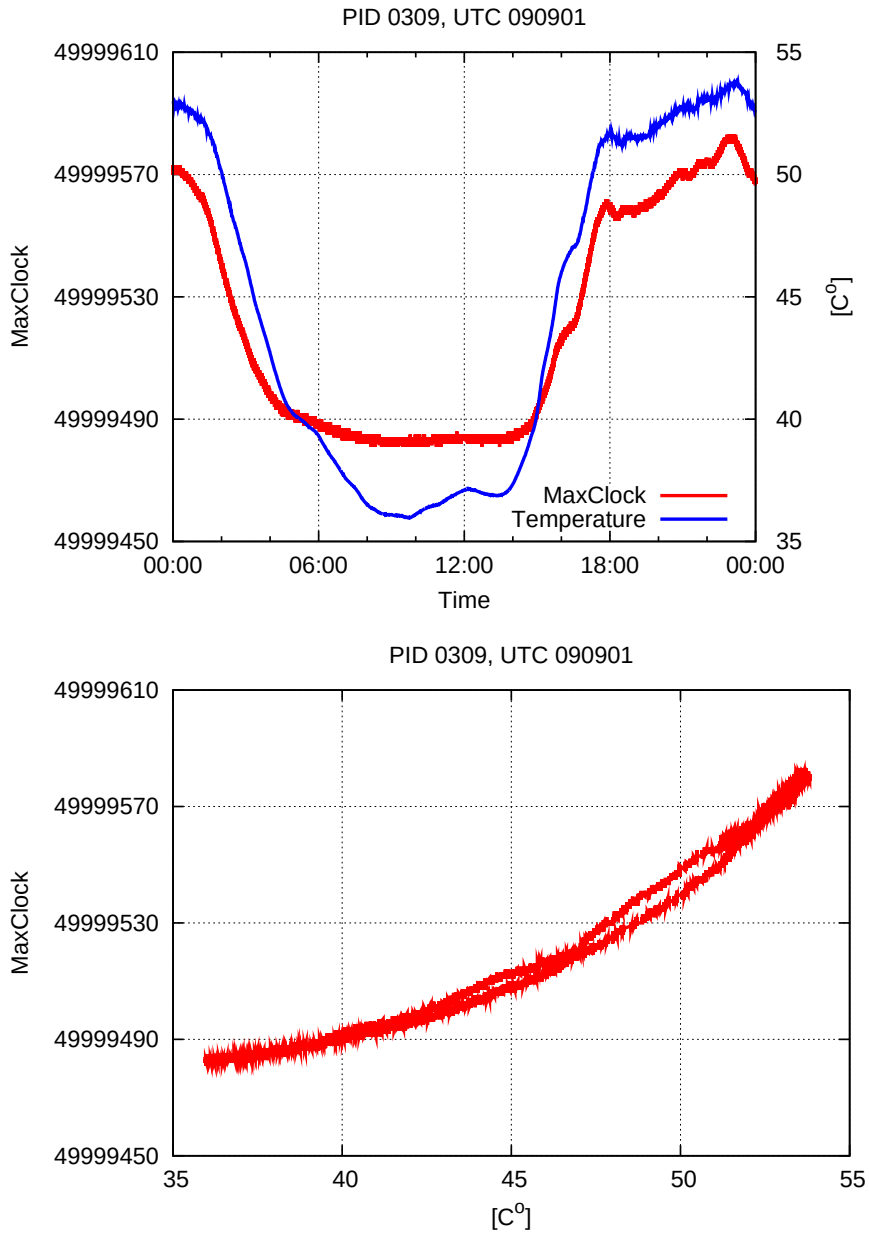

Figure 34: Top: Variation of MaxClock and electronics temperature with time. Bottom: Correlation of electronics temperature and MaxClock.

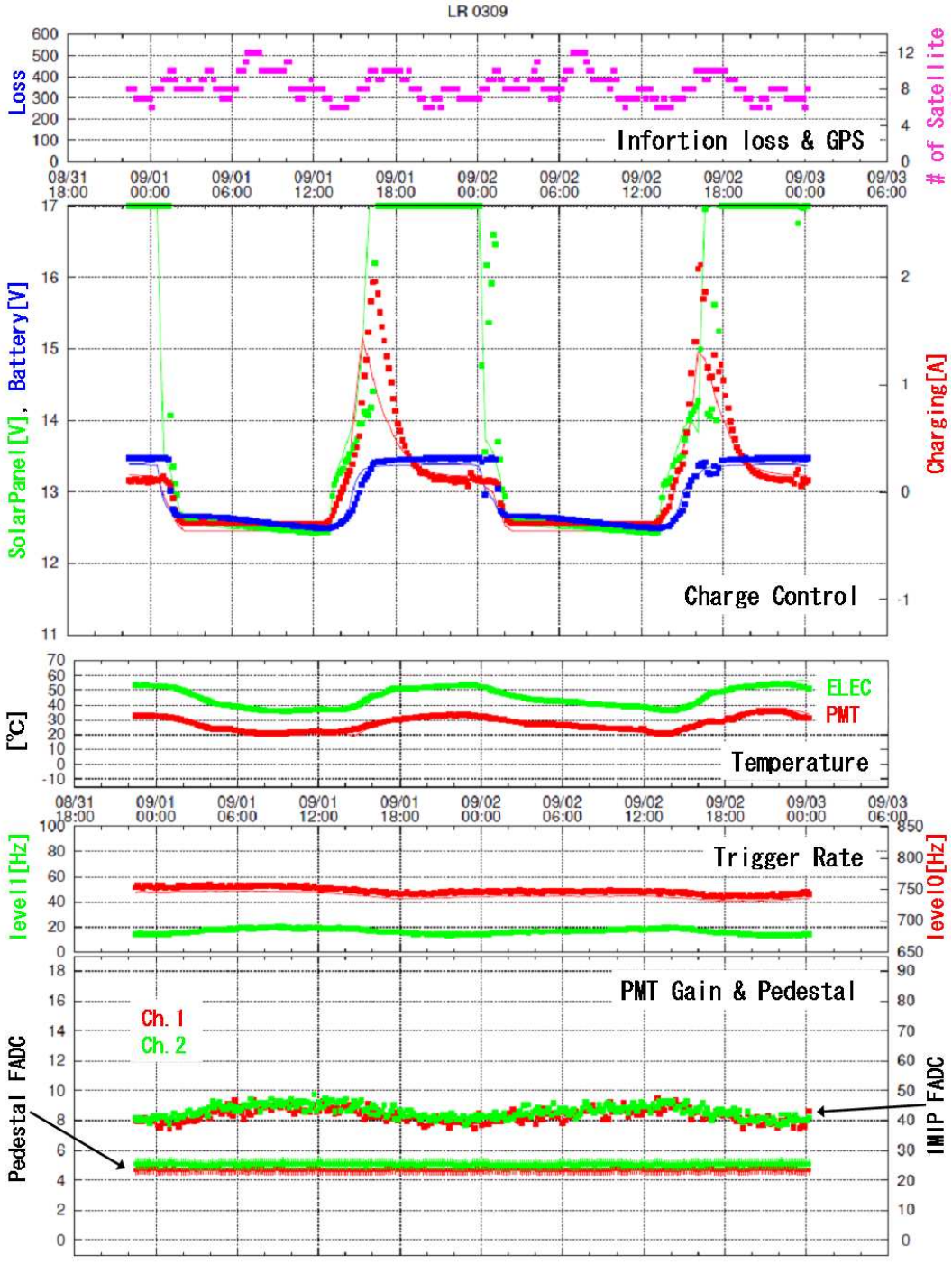

Figure 35: Monitoring plot for individual SD. SolarPanel V: the voltage over 17 V is plotted at 17 V. Pedestal FADC: this is the peak of pedestal histogram (Figure 31) divided by 8. 1MIP FADC: this is the peak of level0 histogram (Figure 33).

3 Reconstruction of Shower Data

I made this reconstruction for arrival direction analysis of ultra high energy cosmic rays. This reconstruction consists of these processes.

- Waveform analysis.
- Pre-selection.
- Initial core search.
- Geometry reconstruction.
  - Direction search (fitting the particle arrival timing).
  - Core search (fitting the number of particles).
- Energy conversion.
- Post-selection.

3.1 Waveform Analysis

First, the program searches for level0 trigger for acquired waveform. Here, I define the FADC count for bin i as C_i, and pedestal average and standard deviation as A and S. A and S is calculated from pedestal histogram. The

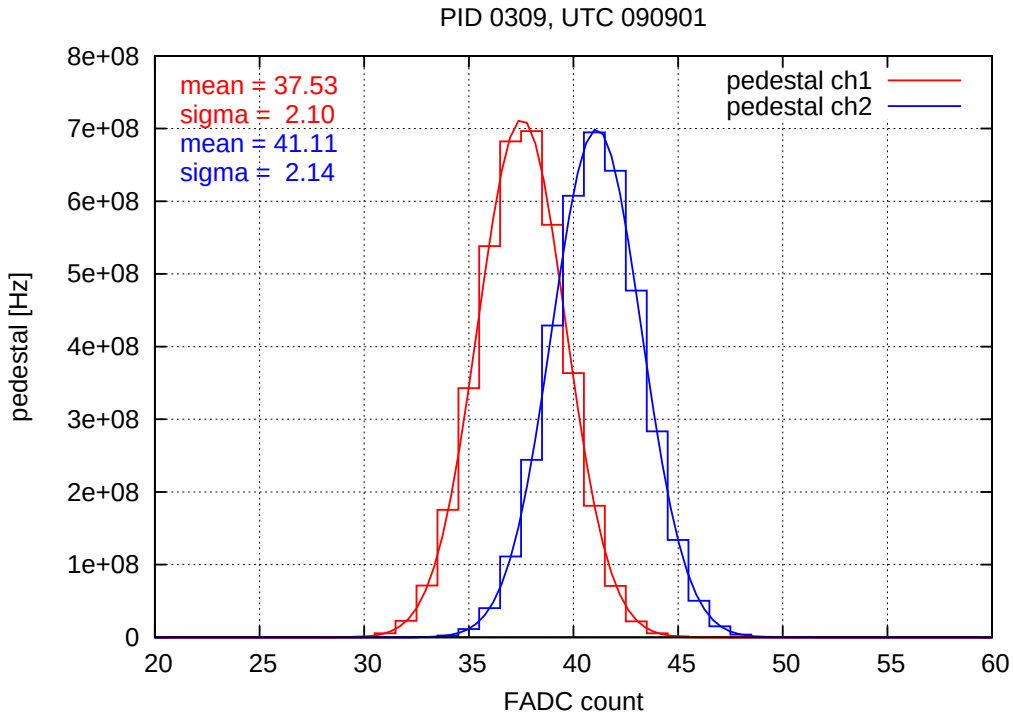

Figure 36: Gaussian fitting for pedestal histogram. This pedestal is 8bins sum. A is mean value / 8. S is sigma value / $\sqrt{8}$.

level0 trigger search is search for j for both layer which satisfied the condition (25).

$$\sum_{i=j}^{j+k} (C_i - A) > 15 \tag{25}$$

Here, j is 0, k moves 1 to 7 and is fixed to 7. After k is fixed to 7, j moves from 0 to larger. If (25) is satisfied for both layer with increasing k and j, $j+k$ is level0 triggered bin.

In order to get the signal region, the program searches Start Bin and End Bin. The threshold is set to 2σ of pedestal distribution in continuous 2bin. Typically, the pedestal standard deviation is 0.8 count. From triggered bin, the program searches previous bin until both layer under threshold, i.e. searches the condition of (26). The first satisfied bin i from triggered bin is Start Bin of signal.

$$\frac{C_i + C_{i-1} - 2 \times A}{2} < \frac{2 \times S}{\sqrt{2}} \tag{26}$$

From triggered bin, the program searches following bin until both layer under threshold, i.e. searches the condition of (27). The first satisfied bin i from triggered bin is End Bin of signal.

$$\frac{C_i + C_{i+1} - 2 \times A}{2} < \frac{2 \times S}{\sqrt{2}} \tag{27}$$

The region between Start Bin and End Bin is signal region, and I define the signal waveform in this region as WaveForm (WF) Unit shown in Figure 37.

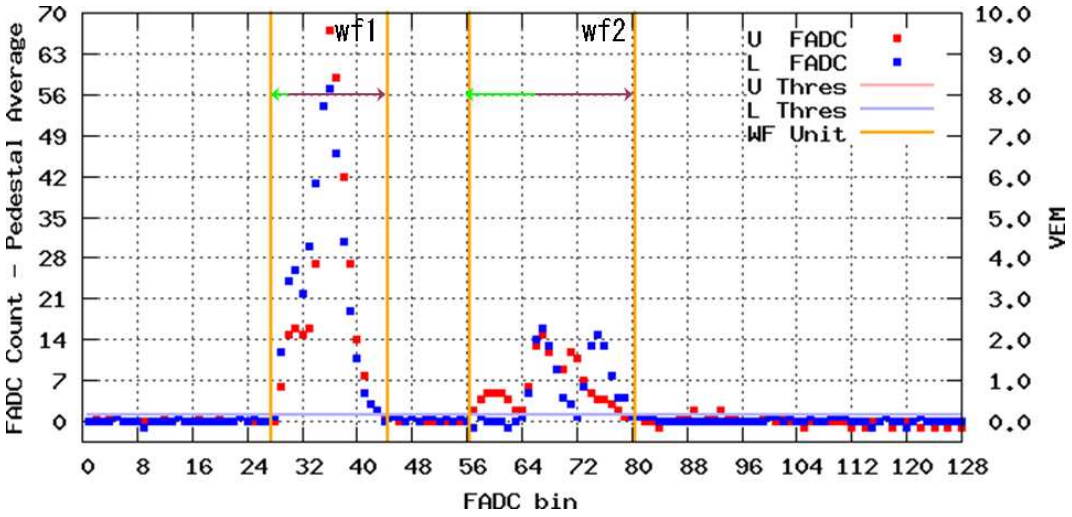

Figure 37: Definition of WF Unit. Green arrow: search for Start Bin. Purple arrow: search for End Bin.

Second, the program searches for integral region of signal for each layer in WF Unit. From Start bin, the program searches following bin until each layer

over threshold, i.e. searches the condition of (28). The first satisfied bin i from Start Bin is Start Integral Bin of signal.

$$\frac{C_i + C_{i+1} - 2 \times A}{2} > \frac{2 \times S}{\sqrt{2}} \tag{28}$$

From End bin, the program searches previous bin until each layer over threshold, i.e. searches the condition of (29). The first satisfied bin i from End Bin is End Integral Bin of signal.

$$\frac{C_i + C_{i-1} - 2 \times A}{2} > \frac{2 \times S}{\sqrt{2}} \tag{29}$$

Third, the program sums up $C_i - A$ for each layer in integral region from Start Integral Bin to End Integral Bin. I treat the signal size as the vertical muon equivalent cont (VEM). The VEM for each layer of the WF Unit is converted from this integration. In integration of WF Unit, the bin that VEM becomes larger than 0.2 VEM is Timing Edge Bin shown in Figure 38. For getting Timing Edge Bin, the VEM integration is connected adjacent integral bin by polygonal line. Therefore, this Timing Edge Bin is not integer bin. The particle arrival timing is defined as this Timing Edge Bin's clock / MaxClock.

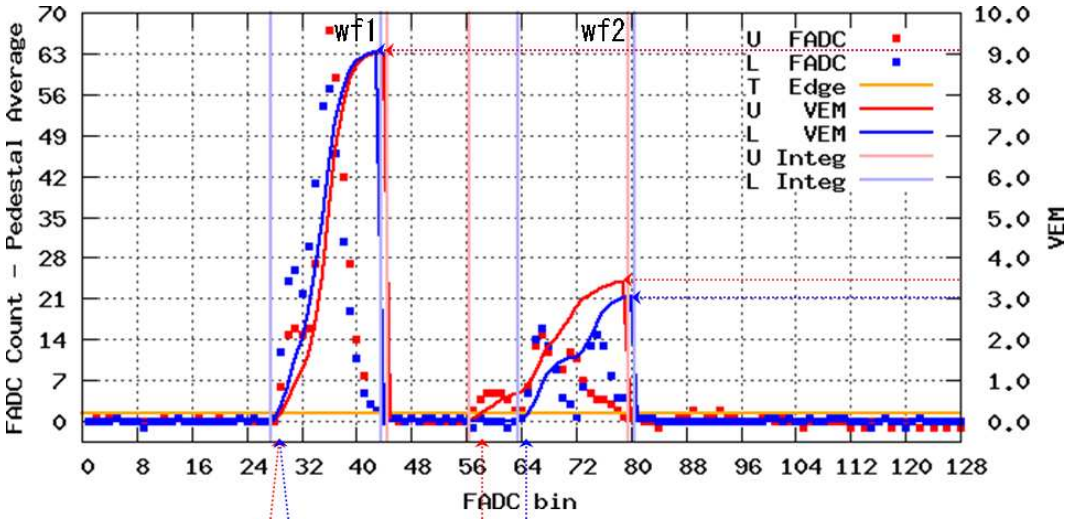

Figure 38: Getting VEM for each layer. Timing Edge Bin is defined as integrating VEM line (Red, Blue) exceed Orange (0.2 VEM).

Here, the arrival particle timing and VEM for each layer for this WF Unit was obtained. Then, the program goes back to (25), in which j starts from current End Bin. These process takes place until the end of acquired waveform. At this point, the arrival particle timing and VEM for each layer for some WF Units was obtained. One timing and VEM are chosen from two layers for each WF Unit. If one layer is disordered, the other layer is chosen. The timing which is earlier in two layers is chosen. For VEM, If both layers are saturated, the big VEM layer is chosen. If one layers is saturated, the other layer VEM is chosen. If both layers are not saturated, the small VEM layer is chosen. Some combination processes of WF Units in 6 us takes place to reduce of choices for fitting in geometry reconstruction process.

3.2 Pre-selection before Geometry Reconstruction

The pre-selection before geometry reconstruction is three steps for the SDs in red region in Figure 39. The event which passes these three conditions goes in the geometry reconstruction.

(1) The biggest VEM SD has over 50 VEM. I call this SD as "MaxSD". (Red region in Figure 39 are defined by MaxSD.)

(2) There are two or more SDs over 10 VEM in red region. (including MaxSD.)

(3) There are six or more hit SDs in red region. Some rough hit pattern selection in red region described later.

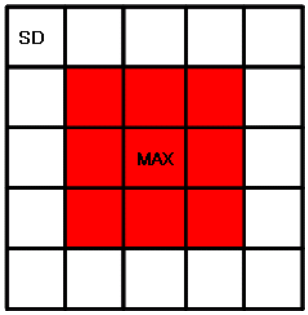

Figure 39: SDs for pre-selection. Each box represents SD because the SDs are arrayed in a square grid.

The detail of selection (3) is following.

The pre-selection (3) is determined by the information from 9 SDs in red region with imaginary SDs. At least, six hit SDs in red region is required. The definition of the type of SDs in red region is here.

- hitSD : There is usable waveform.
- zeroSD : This SD recorded 0VEM, not disordered SD.
- nohitSD : This is disordered SD and imaginary SD.
- insideSD : This is not hitSD but exists and belongs to DAQ tower.

So always, the sum of hitSD, zeroSD and nohitSD is 9.

The procedure by hit pattern of pre-selection (3) is shown in Figure 40. By this selection, basically, the events which passes the pre-selection hit the inside region of active surface detector array. The result of the reconstructed shower core position is described later.

The evaluation of this reconstruction was done by using COSMOS [35] shower Monte Carlo simulation events. Proton is used as a primary composition. QGSJET-II [36] for particle over 80 GeV and DPMJET-III [37] under 80 GeV is used as the interaction model. The primary energy is set from 10^{18} eV to 10^{20} eV with 0.2 step in log(E[eV]). The zenith angle θ is set by $\cos\theta$ from 1.00 to 0.50 with 0.01 step.

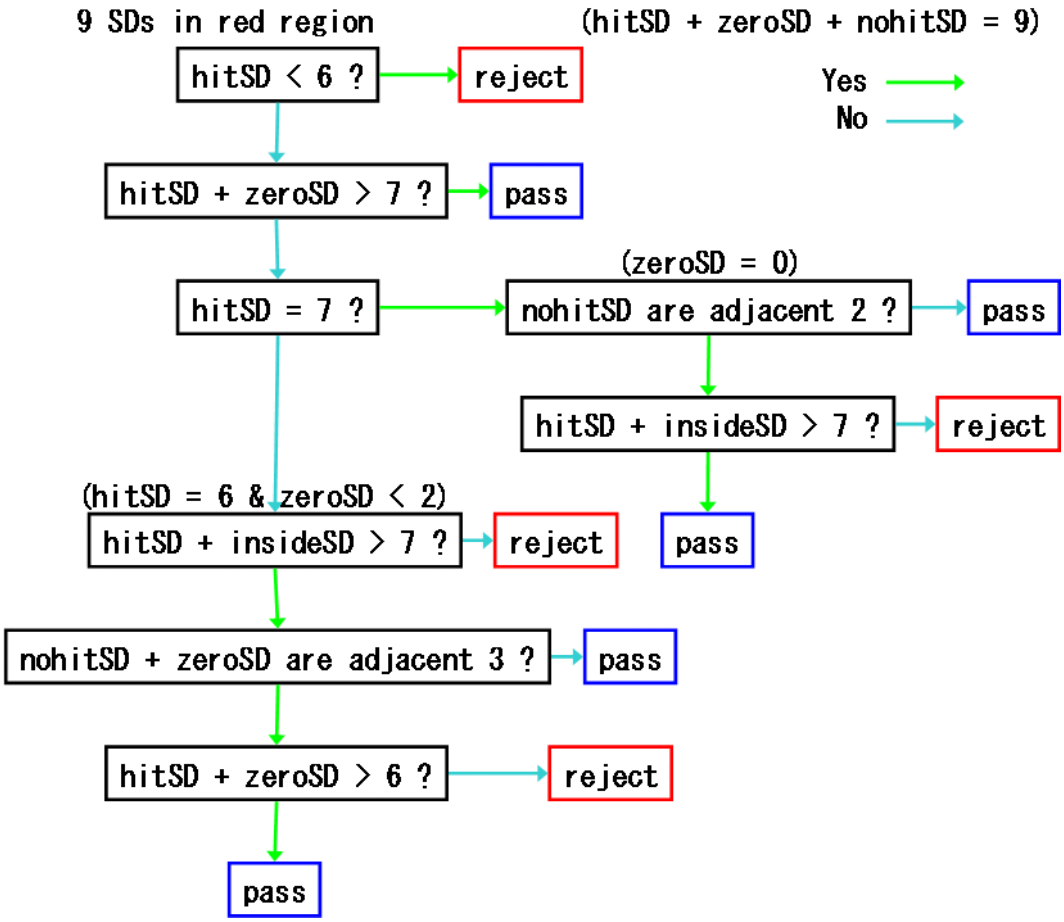

Figure 40: Pattern selection in pre-selection (3). hitSD : There is usable waveform. zeroSD : This SD recorded 0VEM, not disordered SD. nohitSD : This is disordered SD and imaginary SD. insideSD : This is not hitSD but exists and belongs to DAQ tower.

		ALL		w/o Disordered SD	
log(E[eV])	up to zenith angle	45°	60°	45°	60°
18.8		94.1%	89.0%	95.3%	90.0%
19.0		98.9%	96.9%	99.2%	97.4%
19.2		99.3%	99.2%	99.8%	99.5%
19.4		100.0%	100.0%	100.0%	100.0%

Table 1: Left column represents the simulated primary energy. For log(E[eV]) = 19.0, up to zenith angle 45°, ∼99% of events pass the pre-selection.

I checked the efficiency of this pre-selection. Because I would like to know the pure efficiency, I removed the events which hit on edge of the array, before this efficiency check. The result is shown in Table 1.

3.3 Initial Core

The direction search in geometry reconstruction requires the core position. I define the initial core position as the center of gravity of $\sqrt{VEM}$. For the initial core calculation, the SDs used for the center of gravity of $\sqrt{VEM}$ are pre-selection (2) only, i.e. the SDs which detect over 10 VEM in red region in Figure 39 are used. The histogram of the distance of initial core from simulated axis for log(E[eV]) = 19.0 and zenith angle $\leq 45^\circ$ is shown in Figure 41.

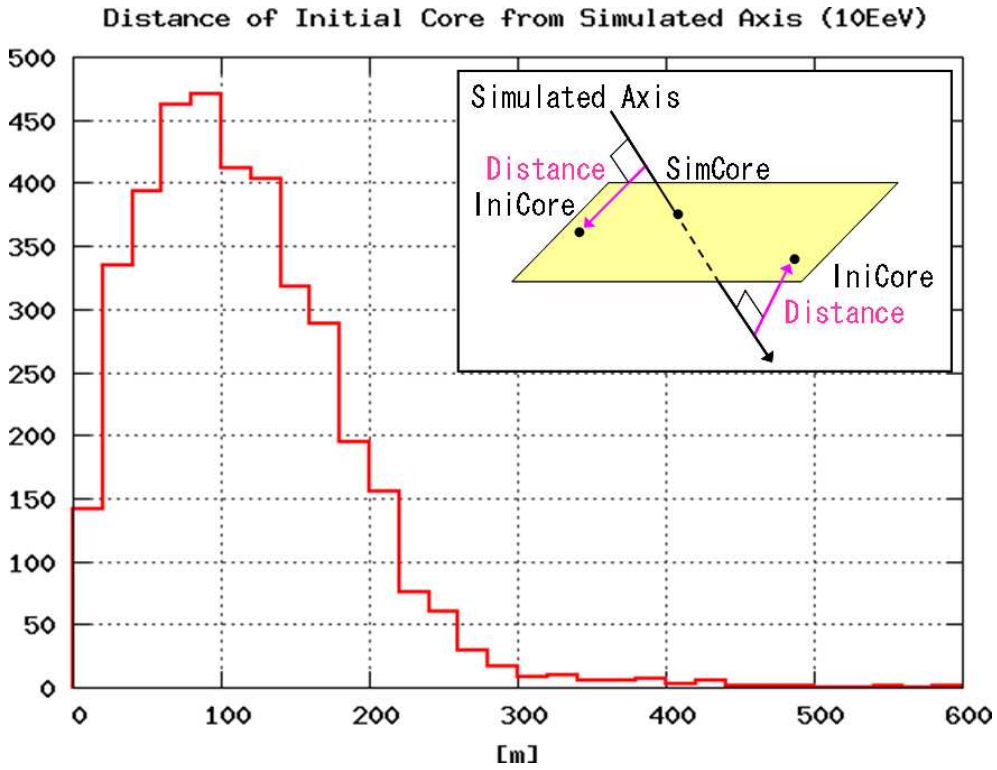

Figure 41: Histogram of initial core distance from simulated axis. The definition of the distance of initial core from simulated axis is shown in right small figure. It is minimum distance between any point on simulated axis and initial core.

3.4 Geometry Reconstruction

Geometry reconstruction has two processes such as direction search and core search. Each process uses the SDs which is shown in Figure 42 defined by MaxSD.

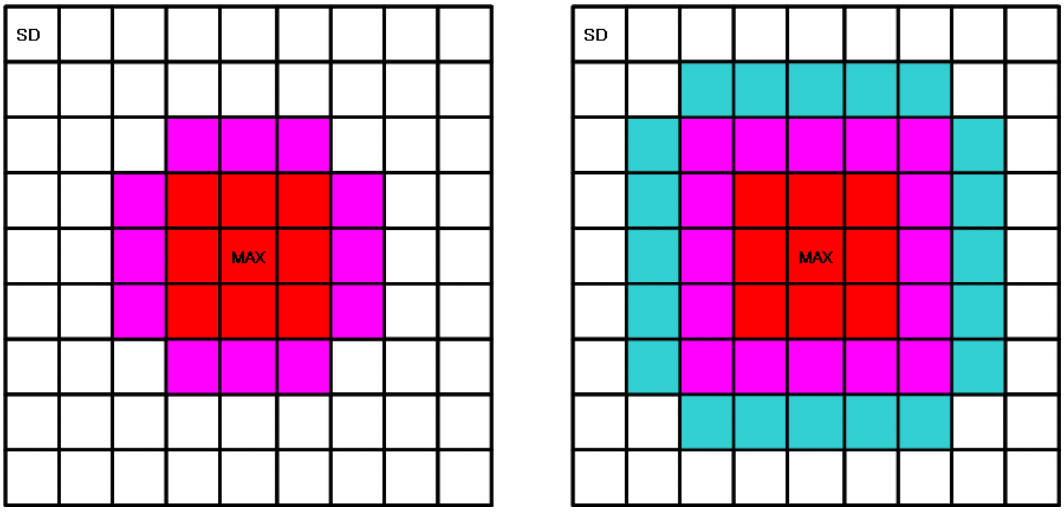

Figure 42: SDs for geometry reconstruction. Each box represents SD because the SDs are arrayed in a square grid. Left: Direction Search uses hitSD within pink region in left figure. Right: Core Search uses SDs within pink region in right figure. and some SDs in cyan region which depend on zeroSD in pink region. If a pink SD is zeroSD, the adjacent cyan SD is not included for reconstruction.

The geometry reconstruction takes place by grid search and iterates three times. The direction search takes place as three parameters search. These three parameters are zenith angle (θ), azimuth angle (φ) and height of certain point in the sky (H). In this reconstruction, the curvature of air shower front is assumed as spreading sphere, and H is the center of the sphere. I call this central point of sphere as "SIP". The shower phenomenon is coarsely grained as all particles on the ground comes from shower axis, and the shower starts from SIP with constant spreading particles. The timing when the shower core hit the ground is not free parameter, because I chose H as a free parameter, which concerns shower front curvature. The timing when the shower core hit the ground can be calculated in the condition that the observed timing at MaxSD is on the shower front sphere. The grid scan range in zenith angle is from 85° to 0° and the range in azimuth angle is from -180° to 180°. The range in height of the center of the shower front sphere is from 16600 m to 4500 m. H is correspond to the altitude in WGS84 for vertical shower axis. The core search takes place as three parameters search. These three parameters are X of core, Y of core and scaling factor K for the number distribution of particles. The practical value of K is shown later in subsection Energy Conversion. For core search, K is just a free parameter for scaling. For direction grid search, the minimum step in zenith angle is 0.09°, in azimuth angle varies by zenith angle. For core grid search, the minimum step of X and Y of core is 5 m.

The reconstruction flow is following.

(1) Direction search for two parameters
The program searches for θ from 85° to 0°,
for φ from -180° to 180°. H is fixed at 16600 m for this search.

(2) Core search for three parameters
The program searches for X and Y within ±750 m from initial core,
and K.

(3) Direction search for three parameters
The program searches for θ and φ around the direction of step-(1),
and H.

(4) Core search for three parameters
The program searches for X and Y within ±200 m from core of step-(2),
and K.

(5) Direction search for three parameters
The program searches for θ and φ around the direction of step-(3),
and H.

(6) Core search for three parameters
The program searches for X and Y within ±80 m from core of step-(4),
and K.

(7) Direction search for three parameters
The program searches for θ and φ around the direction of step-(5),
and H. This last process is not for practical search but for getting final parameters.

This geometry reconstruction has adding up process of spread function. The definition of parameters for reconstruction function is shown in Figure 43. I define certain point on the shower axis. I call this point as "TIP", and TIP moves from SIP to 100 g/cm^2 above each SD with 0.5 g/cm^2 step in a vertical. The spread function is calculated at each TIP.

In this reconstruction, the velocity of light in vacuum is expressed as c. For direction search, I define the observed timing of ith SD as $T_{\mathrm{obs},i}$, which determined by the waveform analysis of ith SD. I also define the shower front model timing at ith SD as $T_{\mathrm{mdl},i}$, which comes from $T_{\mathrm{sip}} + \frac{R1_i}{c}$. Here, I define the time at which shower core passes SIP, as T_{sip}. As written previously, the observed timing at MaxSD is on the shower front model. Therefore, for MaxSD, $T_{\mathrm{obs},MaxSD} = T_{\mathrm{mdl},MaxSD} = T_{\mathrm{sip}} + \frac{R1_{MaxSD}}{c}$. Therefore, for ith SD, $T_{\mathrm{mdl},i}$ is calculated as following.

$$T_{\mathrm{mdl},i} = T_{\mathrm{obs},MaxSD} - \frac{R1_{MaxSD}}{c} + \frac{R1_i}{c} \tag{30}$$

Then, I define the fluctuation of the $T_{\mathrm{mdl},i}$ as $\sigma_{T,i}$. For getting $\sigma_{T,i}$, I defined

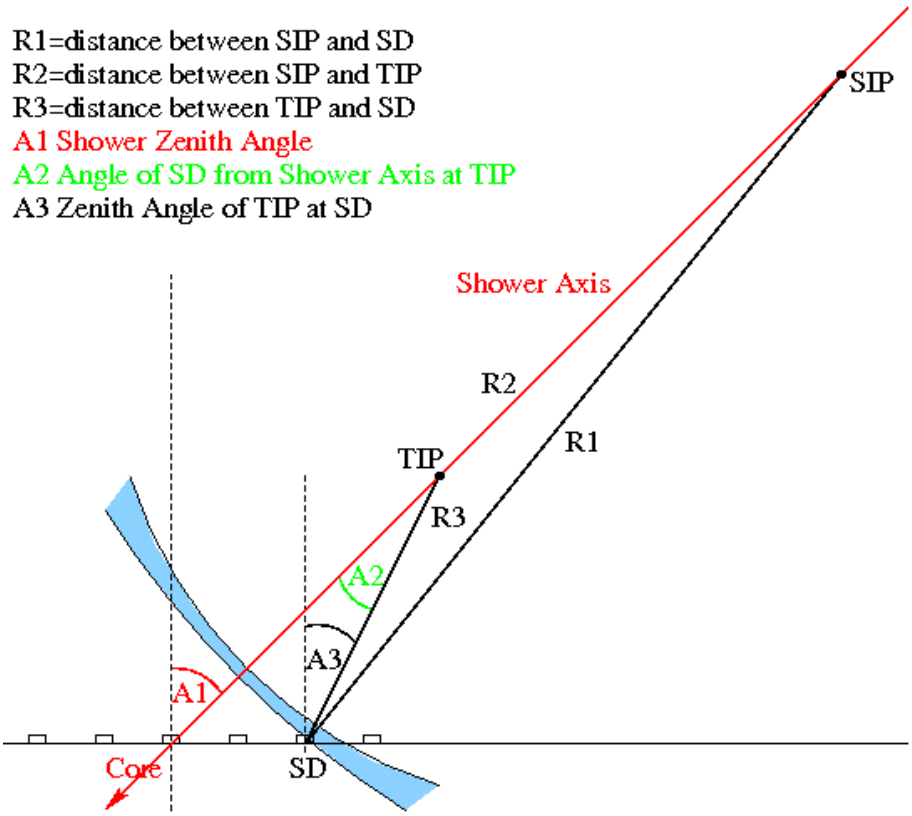

Figure 43: In this reconstruction, I assume that the shower front curvature is sphere centered at SIP. H is the altitude of SIP. TIP on the shower axis moves down from SIP.

the following segment value $s1_i$.

$$f(A2_i) = \frac{\cos^{12}\left(\frac{A2_i}{2}\right)}{\sin^2\left(\frac{A2_i}{2}\right)} \tag{31}$$

$$s1_i = \frac{1}{\cos(A1)} \times \cos(A3_i) \times \frac{1}{R3_i^2} \times f(A2_i) \tag{32}$$

$f(A2_i)$ is the spread function for ith SD at the TIP on shower axis. The factor $\frac{1}{R3_i^2}$ comes from spreading from TIP to ith SD. The factor $\cos(A3_i)$ comes from detection area of ith SD viewed from TIP. The factor $\frac{1}{\cos(A1)}$ comes from adding up procedure in a vertical. I define $S1_i$ as sum of $s1_i$ for all the TIP moved from SIP to 100 g/cm^2 above ith SD with 0.5 g/cm^2 step in a vertical.

I define the number of hit particles of ith SD (N_i) for direction search in (33).

$$N_i = VEM_i \times \cos(A3_i), \text{ if}(N_i < 1)\ N_i = 1 \tag{33}$$

This $A3_i$ is defined by the TIP when the sum of $s1_i$ exceeds the 50% of $S1_i$. The VEM_i is signal size of ith SD in vertical muon equivalent. I define $\sigma'_{T,i}$ in (34).

$$\sigma'_{T,i} = 4.25 \times \frac{R2_i + R3_i - R1_i}{c} \times \frac{1}{\sqrt{N_i}} \tag{34}$$

These $R1_i, R2_i, R3_i$ are defined by the TIP when the sum of $s1_i$ exceeds the 68% of $S1_i$. I define the the fluctuation of 1pps from GPS module as σ_{pps}. In this reconstruction, I set σ_{pps}=20 ns. For $T_{\mathrm{mdl},i}$ less than $T_{\mathrm{obs},i}$, $\sigma_{T,i}$ is calculated in (35).

$$\sigma_T = \sqrt{\sigma_T'^2 + \sigma_{pps}^2} \tag{35}$$

For $T_{\mathrm{mdl},i}$ more than $T_{\mathrm{obs},i}$, basically $\sigma_{T,i}$ is calculated in (36).

$$\sigma_T = \sqrt{(0.05\sigma_T')^2 + \sigma_{pps}^2},\ \mathrm{if}(\sigma_T > 3\sigma_{pps})\ \sigma_T = 3\sigma_{pps} \tag{36}$$

Therefore, $\sigma_{T,i}$ is very asymmetric for $T_{\mathrm{mdl},i}$.

I define that the direction of shower axis is calculated with minimizing χ^2 in (37), through grid searching of three parameters i.e. zenith angle, azimuth angle and H.

$$\chi^2 = \frac{1}{n-3}\sum_{i=1}^{n}\frac{(T_{\mathrm{obs},i} - T_{\mathrm{mdl},i})^2}{\sigma_{T,i}^2} \tag{37}$$

Here, n is the number of hit detector. This is an asymmetric chi-square minimization. Against noise hit there are some treatments in minimizing.

For core search, I change the definition of observed number of particles at ith SD as $N_{\mathrm{obs},i}$ instead of N_i which is defined in (33). I also define the number of particles from the model calculation at ith SD as $N_{\mathrm{mdl},i}$, and the fluctuation of $N_{\mathrm{mdl},i}$ as $\sigma_{N,i}$.

I defined the following segment value $s2_i$.

$$g(A2_i, A1) = \frac{\cos^{8+24(1-\cos(A1))}\left(\frac{A2_i}{2}\right)}{\sin^{1.0+0.5\cos(A1)}\left(\frac{A2_i}{2}\right)} \tag{38}$$

$$s2_i = \frac{1}{\cos(A1)} \times \cos(A3_i) \times \frac{1}{R3_i^2} \times g(A2_i, A1) \tag{39}$$

The adding up process of core search is a little bit different from direction search. $g(A2_i, A1)$ is the spread function for ith SD at the TIP on shower axis. SIP is fixed at H = 16600 m and all SDs are individually moved along the shower axis to the plane (height = 1600 m). H is correspond to the altitude in WGS84 for vertical shower axis. I define $S2_i$ as sum of $s2_i$ for all the TIP moved from SIP to 100 g/cm^2 above ith SD with 0.5 g/cm^2 step in a vertical.

To obtain $N_{\mathrm{obs},i}$ and $\sigma_{N,i}$, the additional definition is shown in Figure 44. By additional definition, I define $N_{\mathrm{obs},i}$ in (40).

$$N_{\mathrm{obs},i} = VEM_i \times \cos(B1_i),\ \mathrm{if}(0 < N_{\mathrm{obs},i} < 1)\ N_{\mathrm{obs},i} = 1 \tag{40}$$

From $S2_i$ and scaling factor K, I define $N_{\mathrm{mdl},i}$ in (41).

$$N_{\mathrm{mdl},i} = (K \times S2_i)^{DEX},\ DEX = 1.5 + 1.0\cos(A1) \tag{41}$$

I define $\sigma_{N,i}^2$ in (42).

$$\sigma_{N,i}^2 = N_{\mathrm{mdl},i}(1.1 + C_i) + (0.05N_{\mathrm{obs},i})^2 \tag{42}$$

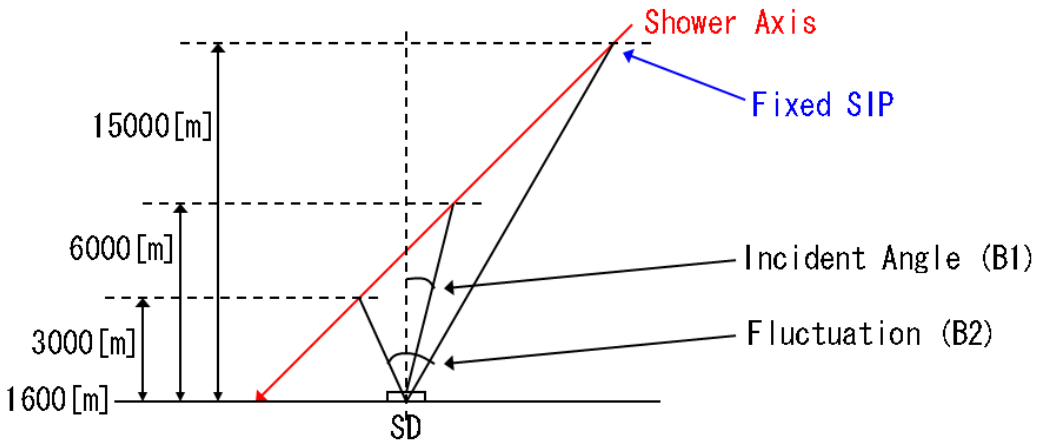

Figure 44: Incident angle and its fluctuation

Here, I define C_i as following function.

$$D_i = \sqrt{(0.1\pi)^2 + B2_i^2},\ \text{if}(D_i > 0.3\pi)\ D_i = 0.3\pi \tag{43}$$

$$C_i = (D_i \times \tan(B1_i))^2 \tag{44}$$

C_i represents the fluctuation factor of energy deposition by incident angle for ith SD. 1.1 in (42) represents the Poisson and some small factor.

I define that the core position is calculated with minimizing χ'^2 in (46), through grid searching of three parameters i.e. X of core, Y of core and K.

$$L_{\sigma,i} = \ln(\sigma_{N,i}^2),\ \text{if}(\sigma_{N,i}^2 < 0.1)\ L_{\sigma,i} = \ln(0.1) \tag{45}$$

$$\chi'^2 = \sum_{i=1}^{n} \frac{(N_{\text{obs},i} - N_{\text{mdl},i})^2}{\sigma_{N,i}^2} + L_{\sigma,i} \tag{46}$$

Here, n is the number of detector. The weight of zeroSD for chi-square sum is 25% of hitSD, whose type of SD are defined in subsection Pre-selection. χ'^2 shown in (46) comes from maximum likelihood estimation of Gaussian model.

$$\begin{aligned} Likelihood &= \prod_i^n \frac{1}{\sqrt{2\pi}\sigma_i} \exp\left(-\frac{(x_i - m_i)^2}{2\sigma_i^2}\right) \\ \ln(Likelihood) &= -\sum_i^n \left\{\ln(\sqrt{2\pi})\right\} - \sum_i^n \{\ln(\sigma_i)\} - \sum_i^n \left\{\frac{(x_i - m_i)^2}{2\sigma_i^2}\right\} \\ &= -\frac{1}{2}\sum_i^n \{\ln(2\pi)\} - \frac{1}{2}\sum_i^n \left\{\frac{(x_i - m_i)^2}{\sigma_i^2} + \ln(\sigma_i^2)\right\} \end{aligned}$$

The maximum $\ln(Likelihood)$ means minimum χ'^2 shown in (46).

In this reconstruction, I use a shower structure model of time delays and number densities of particles including fluctuations, which depend not only on the distance from shower axis. Therefore, it is very difficult that I show the agreement of model and simulated or real data. Comparisons of particle

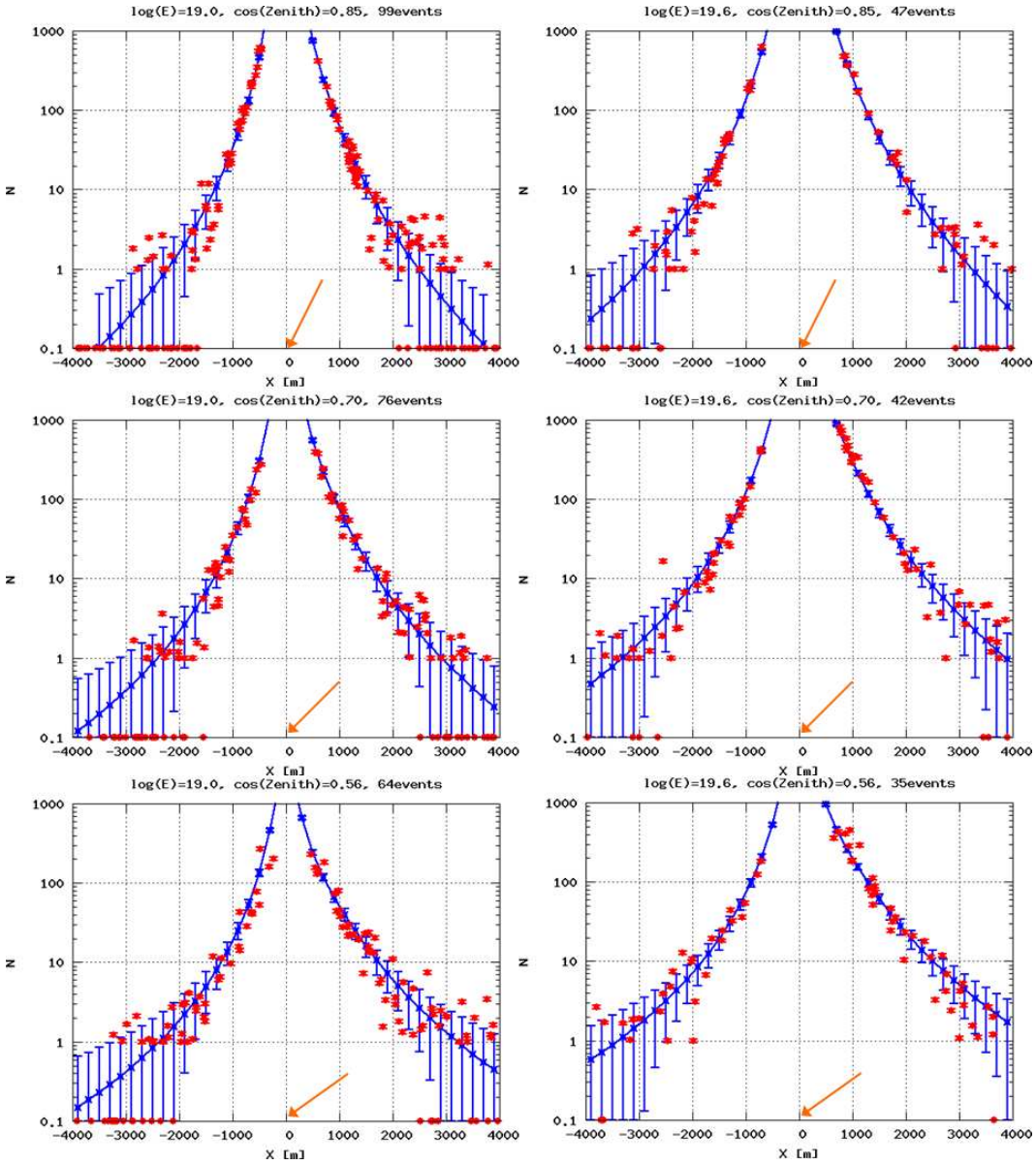

Figure 45: Comparison about particle distribution between model and some simulated events which are superimposed. Red: $N_{\rm sim}$, Blue: $N_{\rm mdl}$. $N_{\rm sim}$ is defined as same as $N_{\rm obs}$ except for difference between real event and simulated event. Taking shower direction ϕ as +x axis. Therefore, +x: earlier stage of shower development, -x: later stage of shower development. $N_{\rm sim}$ are from the SDs -200 m <y< 200 m. $N_{\rm mdl}$ are calculated as y=$\pm$100 m. Simulated zeroSD is plotted at N=0.1. The error bars on $N_{\rm mdl}$ are calculated with the first term of (42). The error bars on $N_{\rm sim}$ are calculated with the second term of (42). Left: log(E[eV])=19.0, Right: log(E[eV])=19.6. Top: cos(θ)=0.85, Middle: cos(θ)=0.70, Bottom: cos(θ)=0.56. Here, θ is zenith angle of shower direction.

distribution between the model calculation and MC simulated events as cross-sectional views which region contains shower axis is shown in Figure 45.

I call the systematic errors of the reconstructed core position as "core bias". The core bias is evaluated by "Cx" distribution. The definition of Cx is shown in Figure 46.

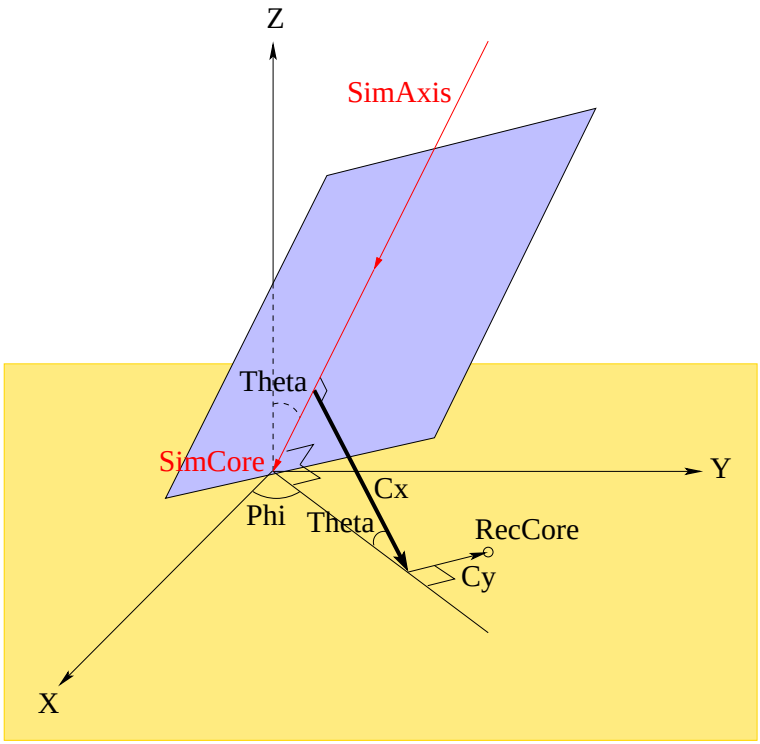

Figure 46: The definition of Cx for the shower direction (Theta,Phi). For the sign of Cx, the blue plane is defined as which contains shower axis and perpendicular to Phi-Z plane. The sign of Z of the minimum distant position on the blue plane from RecCore correspond to the sign of Cx, when Z of SimCore is 0. +Cx: earlier stage of shower development, -Cx: later stage of shower development. Cy is symmetric.

The core bias is evaluated from Cx histogram of MC simulated events shown in Figure 47. The evaluations of the core position resolution are shown in Figure 48. This red histogram on top in Figure 48 corresponds to Figure 41. The difference between both red histogram shows that the geometry reconstruction works well.

The zenith angle bias is evaluated from zenith angle histogram shown in Figure 49. The evaluations of the angular resolution are shown in Figure 50. The bottom in Figure 50 corresponds to Fig. 1 in [17].

For a simulated event sample in the primary energy of $10^{19.6}$ eV, the overview is shown in Figure 51, and the fitted result by geometry reconstruction is shown in Figure 52.

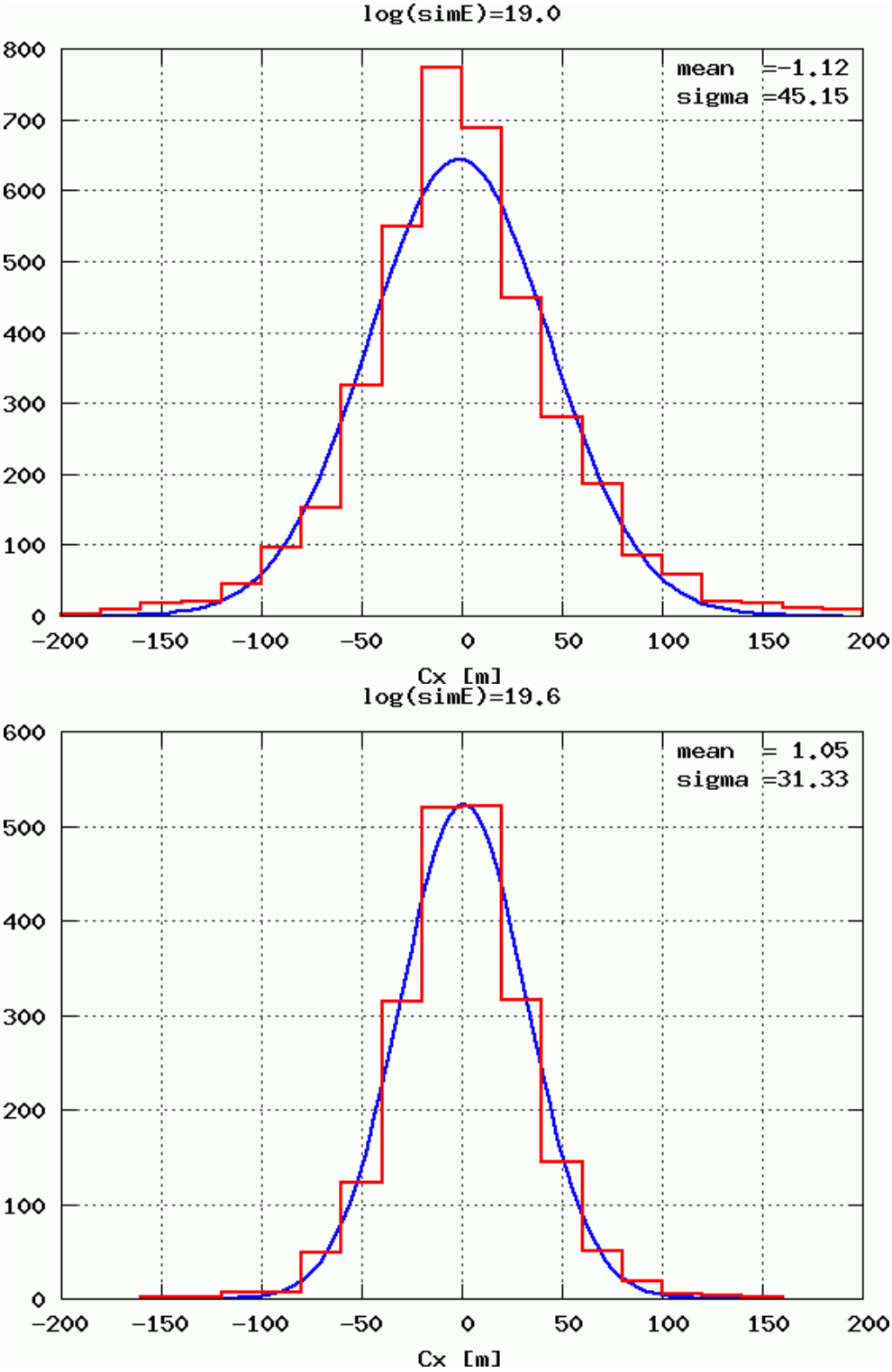

Figure 47: Cx histogram for evaluating core bias (Red) for the events whose zenith angle is less than 45°. Blue line is fitted Gaussian. Top: log(E[eV]) = 19.0, Bottom: log(E[eV]) = 19.6

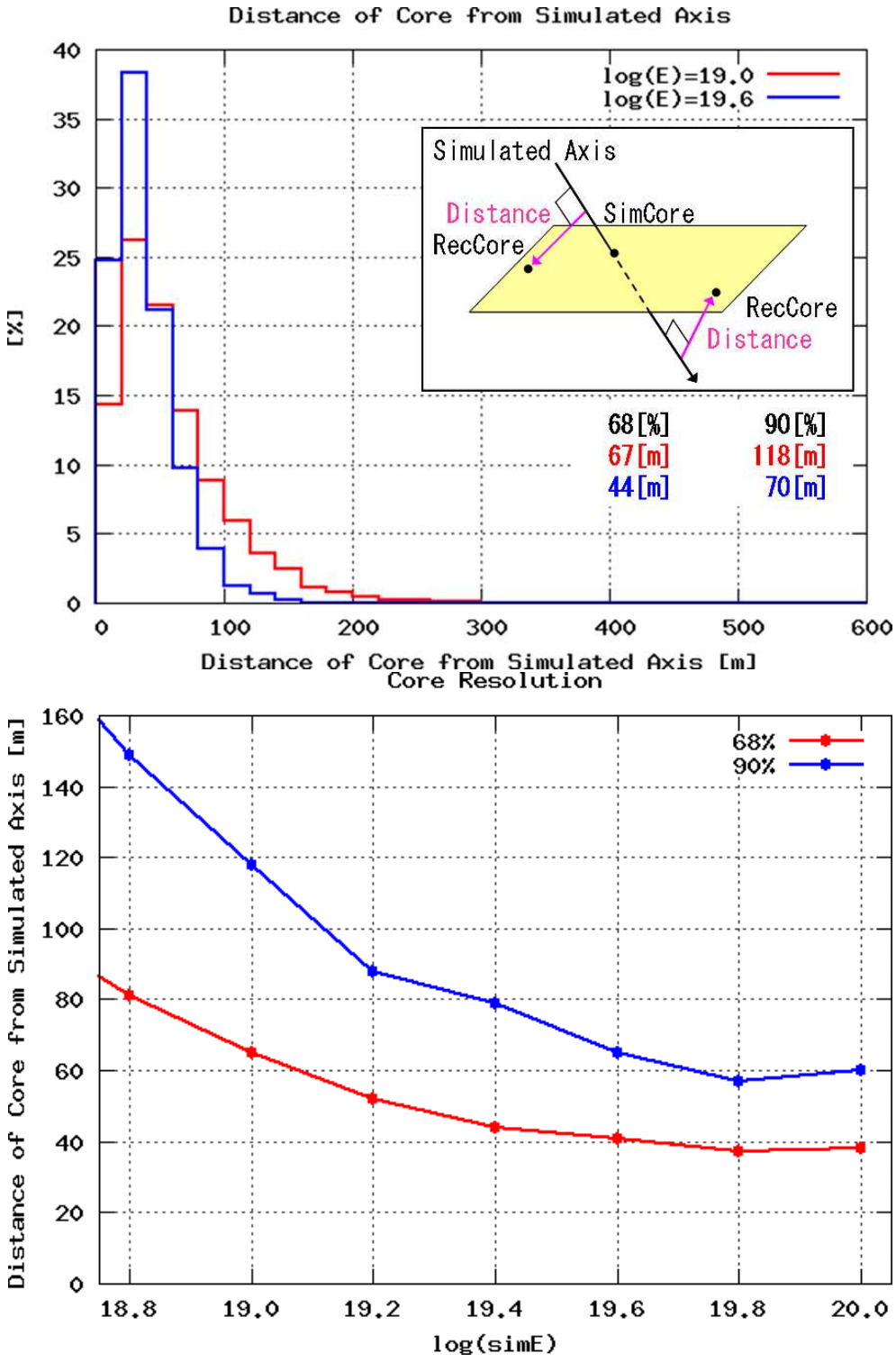

Figure 48: Core resolution for the events whose zenith angle is less than 45°. Top: Distribution of distance of reconstructed core from simulated axis, (Red: log(E[eV])=19.0, Blue: log(E[eV])=19.6). Bottom: Energy dependence of core resolution, (Red: The distance of reconstructed core from simulated axis encompasses 68% of events, Blue: The distance of reconstructed core from simulated axis encompasses 90% of events).

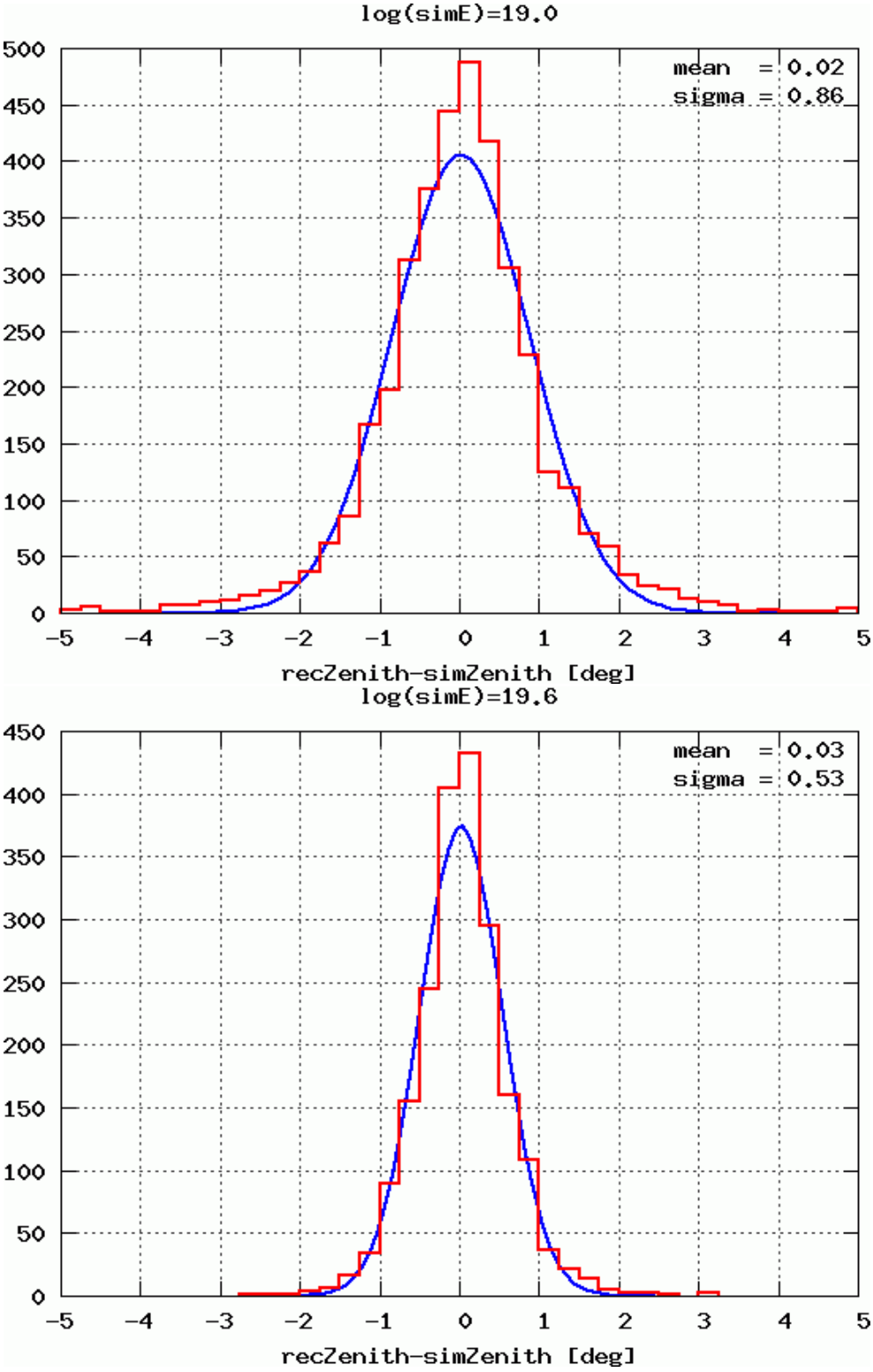

Figure 49: Zenith angle histogram for evaluating zenith angle bias (Red) for the events whose zenith angle is less than 45°. Blue line is fitted Gaussian. Top: log(E[eV]) = 19.0, Bottom: log(E[eV]) = 19.6

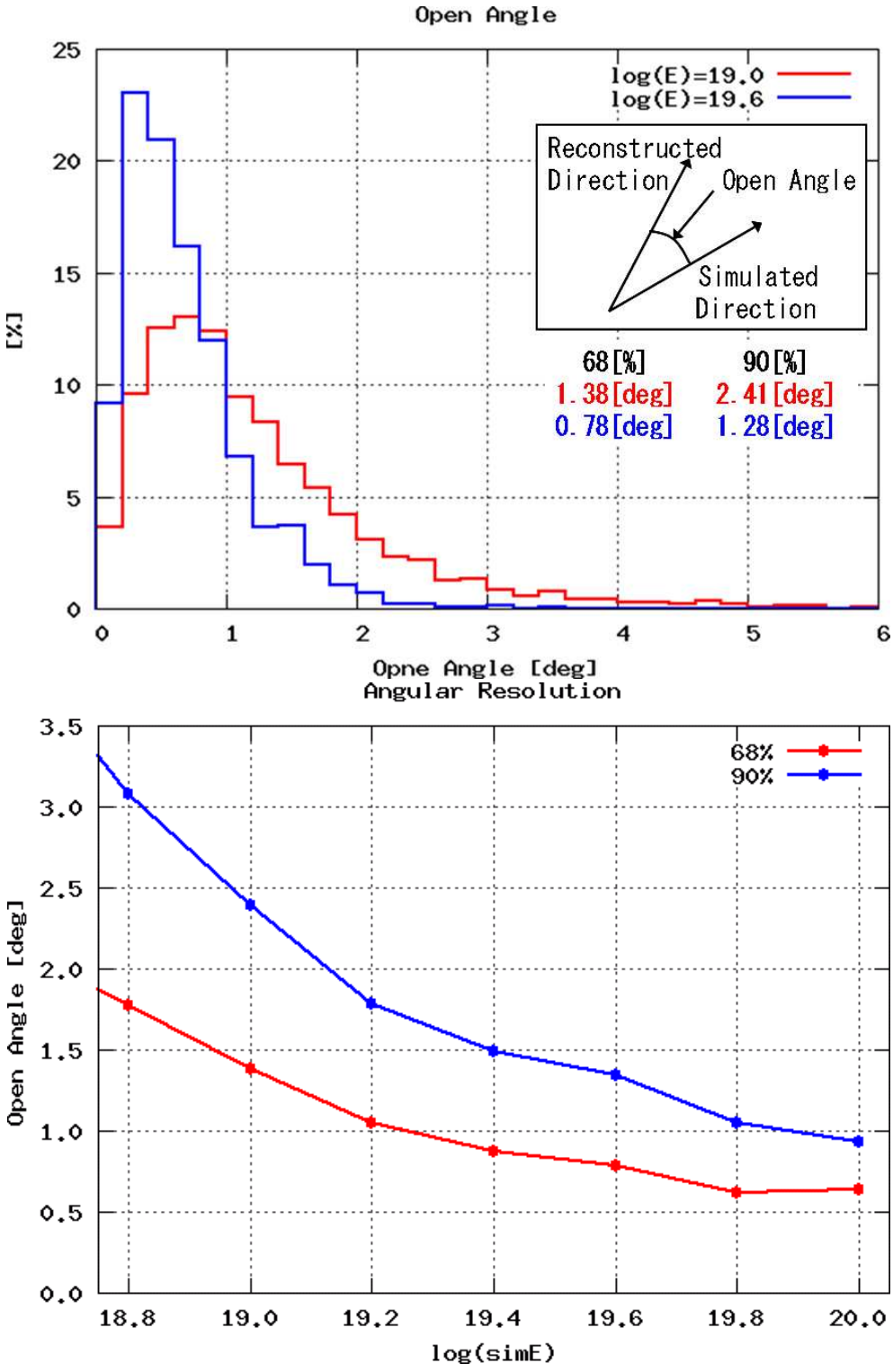

Figure 50: Angular resolution for the events whose zenith angle is less than 45°. Top: Distribution of opening angle between simulated direction and reconstructed direction, (Red: log(E[eV])=19.0, Blue: log(E[eV])=19.6). Bottom: Energy dependence of angular resolution, (Red: The opening angle between simulated direction and reconstructed direction encompasses 68% of events, Blue: The opening angle between simulated direction and reconstructed direction encompasses 90% of events).

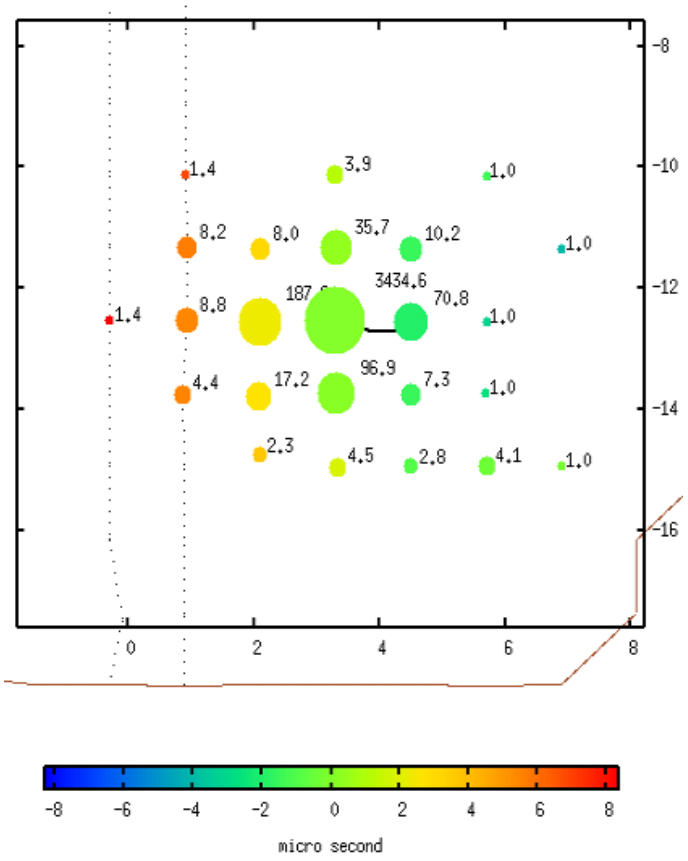

Figure 51: Overview of MC sample event the primary energy of $10^{19.6}$ eV, whose zenith angle is less than 45°. The simulated arrival direction is (Theta,Phi)=(39.90°,-1.76°). The number beside the circles which are plotted on the SD location indicates the number of particles in VEM unit. The colors of the circles indicates the leading edge relative timing to the MaxSD, when arrival particles comes to the SD.

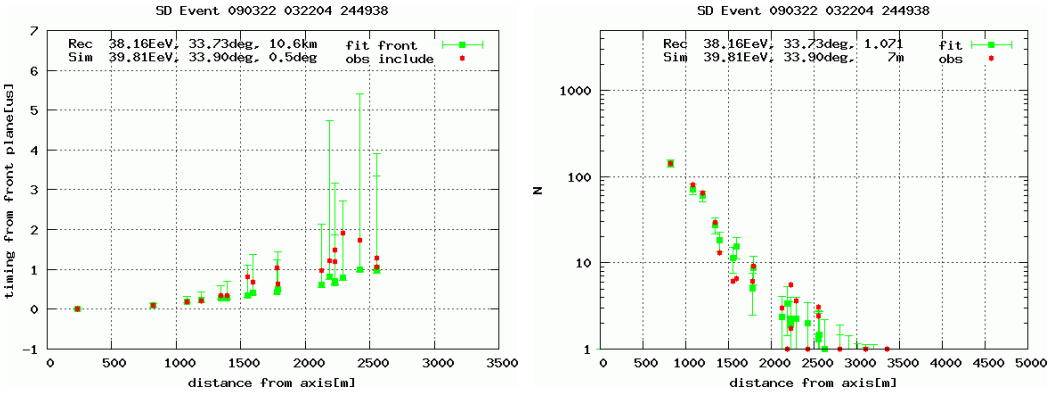

Figure 52: The fitted result of the event in Figure 51. Left: Delays of the particle arrival timing for each distance from shower axis. The green point with error bar shows $T_{\rm mdl}$ and σ_t. The red points shows $T_{\rm sim}$. Right: Number of particles (except for saturated SD) for each distance from shower axis. The green point with error bar shows $N_{\rm mdl}$ and σ_N. The red points shows $N_{\rm sim}$.

3.5 Energy Conversion

The scaling parameter K which is used for core search in geometry reconstruction depends on its primary energy and arrival zenith angle. Therefore, I need a parameter which is independent of arrival zenith angle and dependent on primary energy. I call this parameter as K'. From the many MC simulated events, I employ the fitting function, shown in (48), to describe the relation between K and zenith angle through K'.

$$x = \cos(\theta), \quad \theta : zenith\ angle \tag{47}$$

$$K = K' \left(1.0 - (1.7 + 0.5K') \left| x - \frac{5.75 - K'}{8.0} \right|^{1.5} \right) \tag{48}$$

Here, K' is the maximum of the function (48). The result of K and zenith angle from many MC simulated events whose primary energy are $10^{19.0}$ eV and $10^{19.6}$ eV is shown in left part of Figure 53. I employ the fitting function,

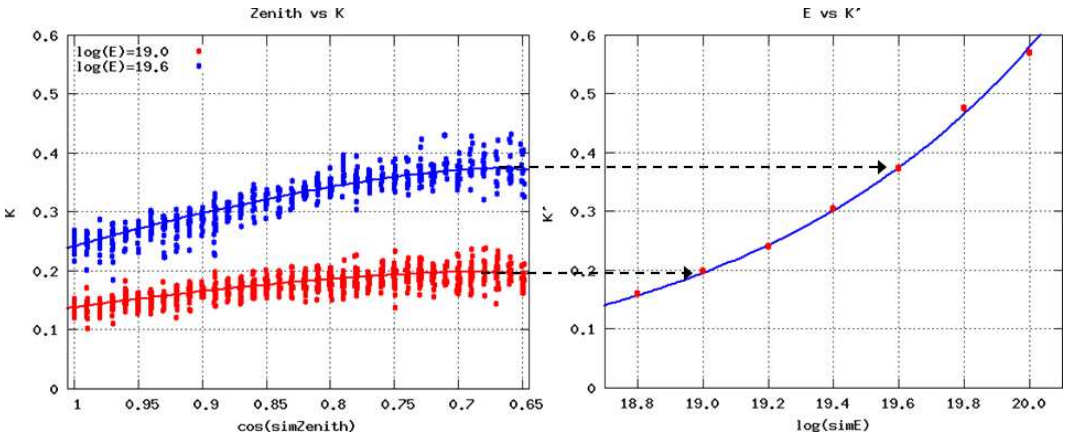

Figure 53: Left: The scatter plot of zenith angle and K whose simulated energy is $10^{19.0}$ eV and $10^{19.6}$ eV. The fit function (48) is obtained from this scatter plot and obtained the maximum of fit function K'. Right: The conversion function (50) from K' to energy is obtained. Therefore, the energy is determined by zenith angle and K for each event.

shown in (50), to describe the relation between K' and primary energy. This result is shown in right part of Figure 53.

$$E = \log(PrimaryEnergy[EeV]) \tag{49}$$

$$K' = 0.374e^{1.09(E-1.6)} \tag{50}$$

The energy is determined for each event from these conversion function.

The comparison between simulated energy and reconstructed energy, whose simulated energy is $10^{19.0}$ eV and $10^{19.6}$ eV, is shown in Figure 54. From these comparison, I evaluate the systematic errors and resolutions for each simulated energy. The primary energy dependence of the systematic errors and resolutions are shown in Figure 55. The energy resolution goes better with simulated energy increasing up to $10^{19.2}$ eV. This effect mainly comes

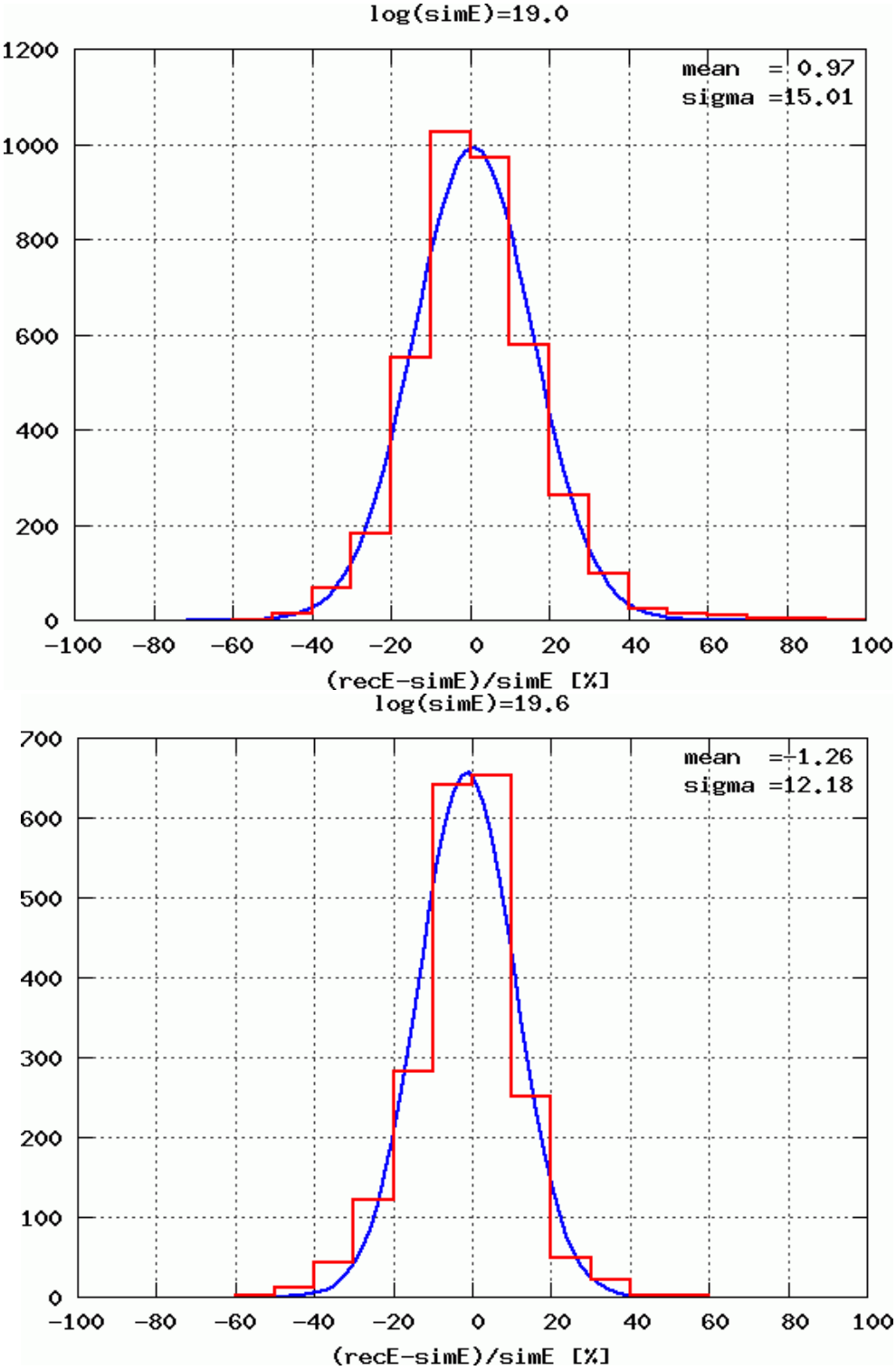

Figure 54: Energy histogram for evaluating systematic error and resolution (Red) for the events whose zenith angle is less than 45°. This histogram describes the reconstructed energy ratio for the simulated energy. Blue line is fitted Gaussian. Top: log(E[eV]) = 19.0, Bottom: log(E[eV]) = 19.6

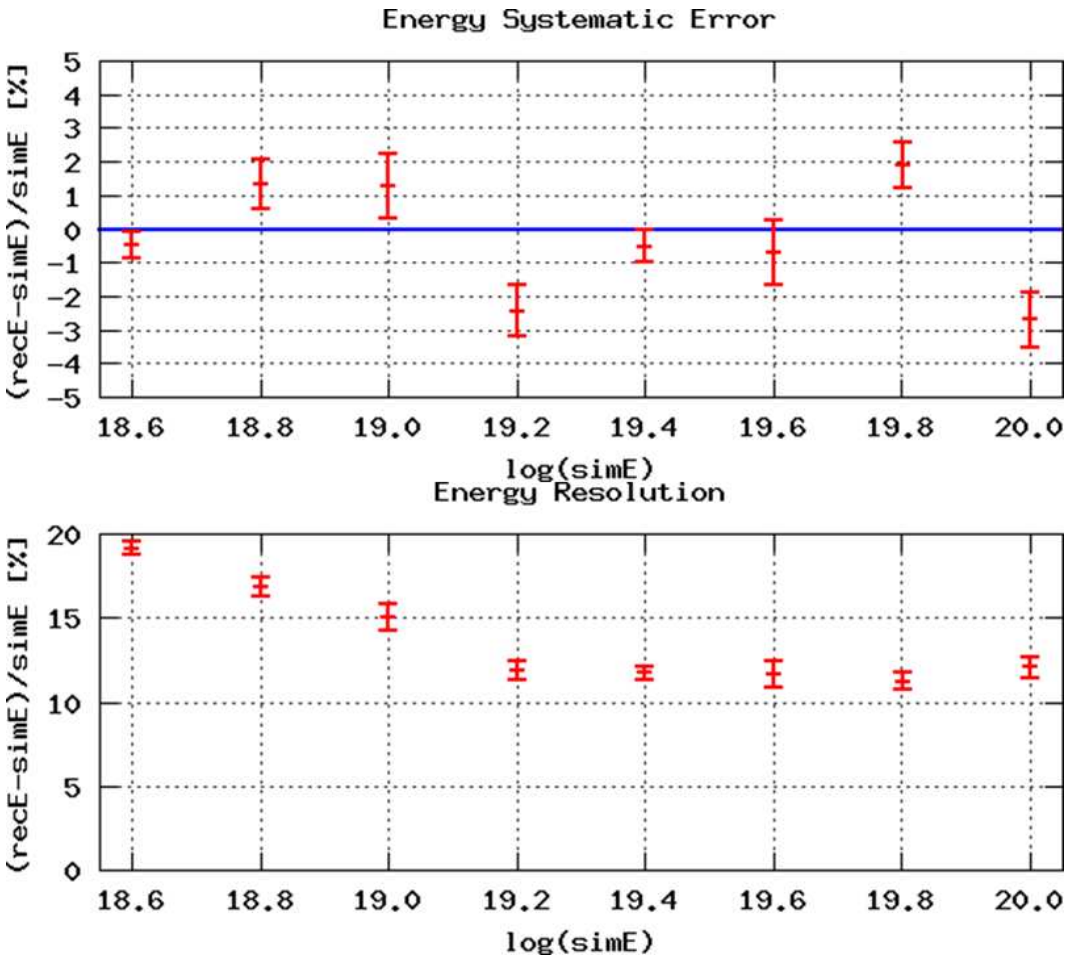

Figure 55: Evaluation of energy estimation for the events whose zenith angle is less than 45°. Top: Energy dependence of energy systematic error. This is mean value of comparison between reconstructed energy and simulated energy, shown in Figure 54 for each energy. The error bars are fitting error by Gaussian. Bottom: Energy dependence of energy resolution, This is sigma value of comparison between reconstructed energy and simulated energy, shown in Figure 54 for each energy. The error bars are fitting error by Gaussian.

from increasing the number of hit detector. Over $10^{19.2}$ eV, the remained factor mainly comes from the fluctuation of shower development, i.e. the fluctuation of first interaction point of primary cosmic ray.

3.6 Summary of Shower Data

The data term which I used for the arrival direction analysis is from May 11, 2008 to September 07, 2010. This reconstruction was made for the arrival direction analysis on this thesis. The result of the number of events which belongs to each stage of this reconstruction is shown in Table 2. The outside

Triggered	393509events
Passed pre-selection	16922events
Reconstructed	16902events
Arrival zenith angle $\leq 45°$	12580events
Core located inside array	12578events
Core located outside array	2events

Table 2: Number of events for each stage.

array two events are 40 m and 66 m out from the border of the array. Originally, the pre-selection works as a gradual 600 m border cut. Therefore, There are very few events whose core is located outside array. The events which I use for direction analysis on this thesis are the events whose core location is inside array and zenith angle is equal or less than 45°. The reconstructed core location map is shown in Figure 56. These events are "Arrival zenith angle $\leq 45°$" 12580 events in Table 2.

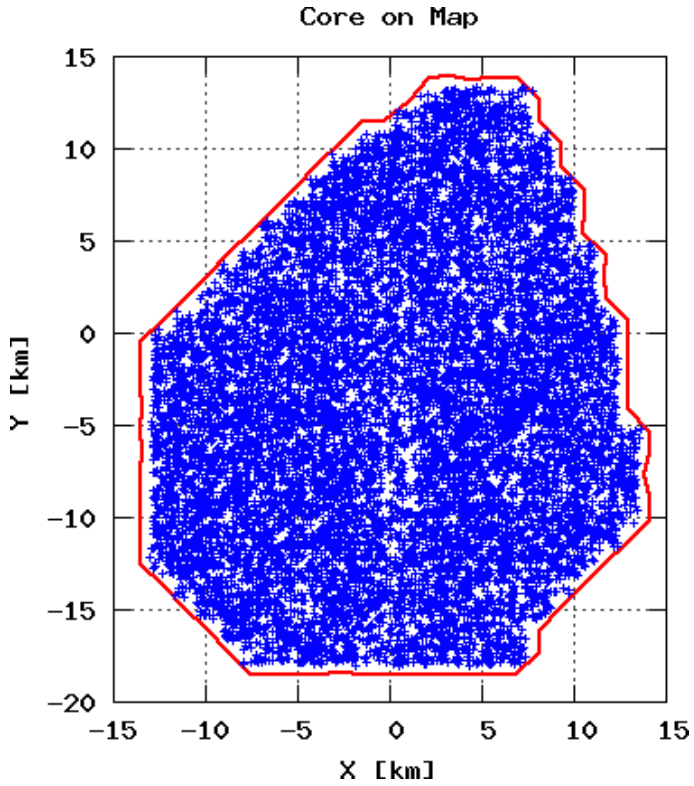

Figure 56: Core location map for the events whose zenith angle is equal or less than 45°.

The energy estimated by SD is different from the energy estimated by FD. For the post reconstruction analysis by TASD, current TASD energy is rescaled to FD energy which was by June 2008 FD data set. However, that FD data set has very small statistics. Therefore, the energy of current SD result for the arrival direction analysis is rescaled to another SD result, whose result was rescaled to FD by factor 1.27 and presented as an energy spectrum. This reconstruction which I made has better angular resolution compared with another SD reconstruction. The rescale factor is 1.10 by comparison between the two SD result for same events whose event satisfies the condition of $\sqrt{E_1[\mathrm{EeV}] \times E_2[\mathrm{EeV}]} \geq 10$. Here, subscript 1 shows another SD result presented as an energy spectrum. Subscript 2 shows my reconstruction result. We can get rescale factor by ratio histogram shown in Figure 57. The ratio histogram is taken as $\log(E_2/E_1)$, Therefore, the rescale factor

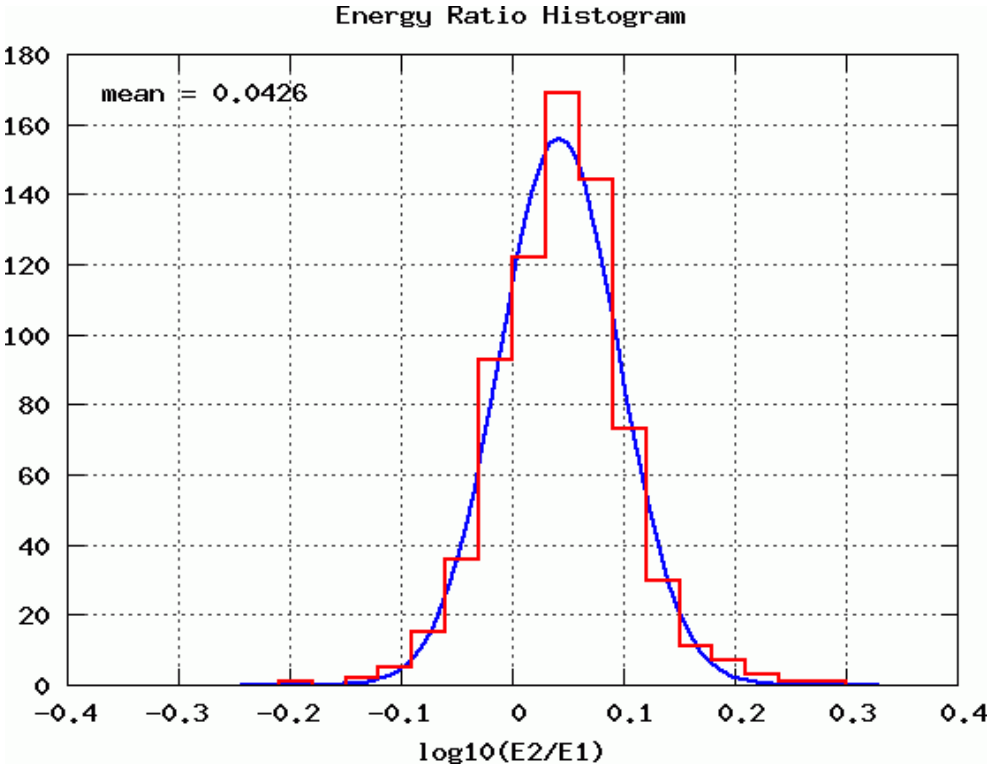

Figure 57: Energy ratio histogram for the events which satisfies the condition of $\sqrt{E_1[\mathrm{EeV}] \times E_2[\mathrm{EeV}]} \geq 10$.

$\frac{E2}{E1} = 10^{0.0426} \approx 1.10$. The energy threshold for the arrival direction analysis in this thesis is rescaled energy by 1.10.

For reconstructed highest energy event whose zenith angle is less than 45°, the overview is shown in Figure 58, and the fitted result by geometry reconstruction is shown in Figure 59.

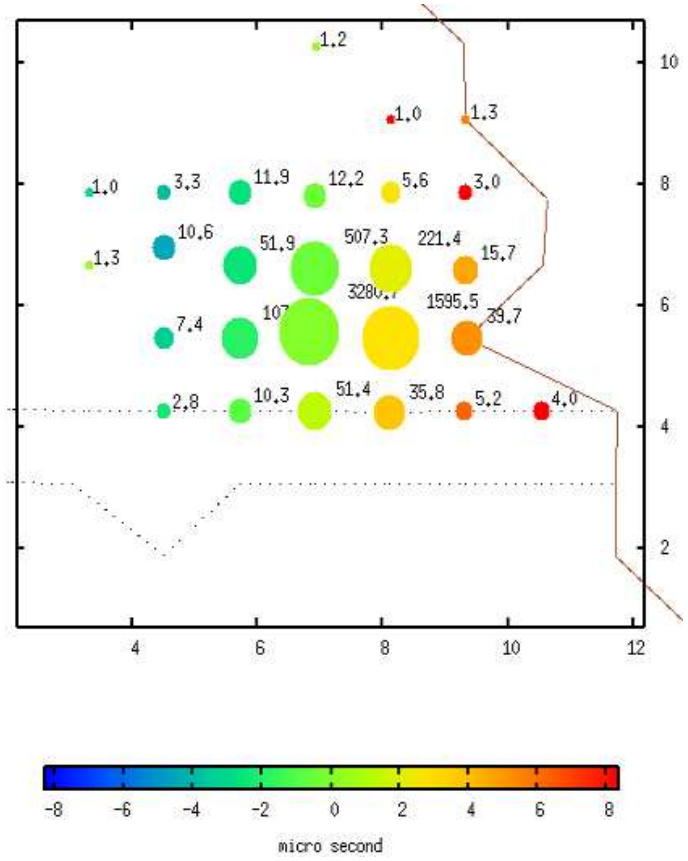

Figure 58: Overview of the highest energy event, whose zenith angle is less than 45° and core is inside the array. The simulated arrival direction is (Theta,Phi)=(38.06°,162.99°). The number beside the circles which are plotted on the SD location indicates the number of particles in VEM unit. The colors of the circles indicates the leading edge relative timing to the MaxSD, when arrival particles comes to the SD.

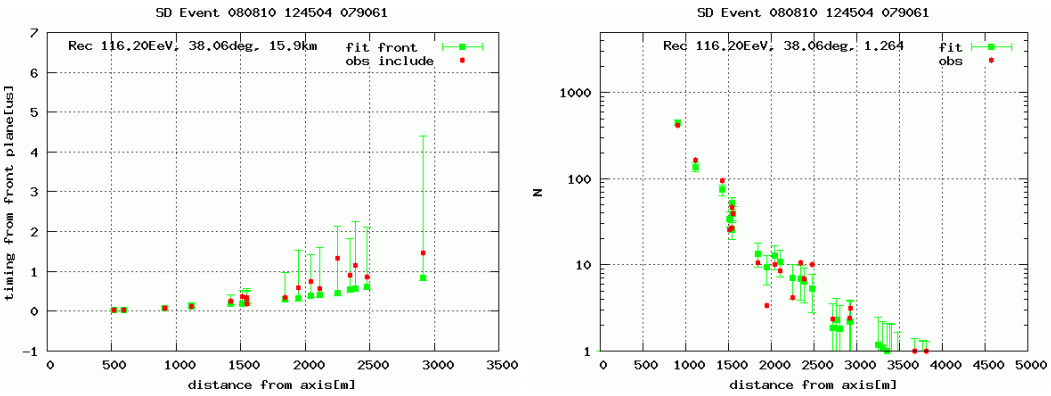

Figure 59: The fitted result of the event in Figure 58. Left: Delays of the particle arrival timing for each distance from shower axis. The green point with error bar shows $T_{\rm mdl}$ and σ_t. The red points shows $T_{\rm obs}$. Right: Number of particles (except for saturated SD) for each distance from shower axis. The green point with error bar shows $N_{\rm mdl}$ and σ_N. The red points shows $N_{\rm obs}$.

4 Analysis of Arrival Direction

4.1 Basic Angular Distribution and Sky Map

From Table 1, for the event energy whose energy is higher than 10 EeV and zenith angle less than 45°, the reconstruction efficiency is over 99%. In addition, TASD is deployed on the very flat ground for the detector spacing. Therefore, the exposure can be calculated simply by $\sin\theta\cos\theta$. Here, θ is zenith angle.

For arrival direction analysis in this thesis, I used the data observed from May 11, 2008 to September 07, 2010, and reconstructed events whose energy is higher than 10 EeV and zenith angle is less than 45°. There are 816 events whose energy are higher than 10 EeV, and, 42 events whose energy are higher than 40 EeV.

The scatter plot of the events for detected time and right ascension is shown in Figure 60. The arrival distribution in the horizontal coordinate is shown in Figure 61, in the equatorial coordinate is shown in Figure 62, in the galactic latitude is shown in Figure 63. The observed data looks consistent with the expected value from isotropic distribution. The sky map for the events whose energy is higher than 10 EeV and 40 EeV is shown in Figure 64.

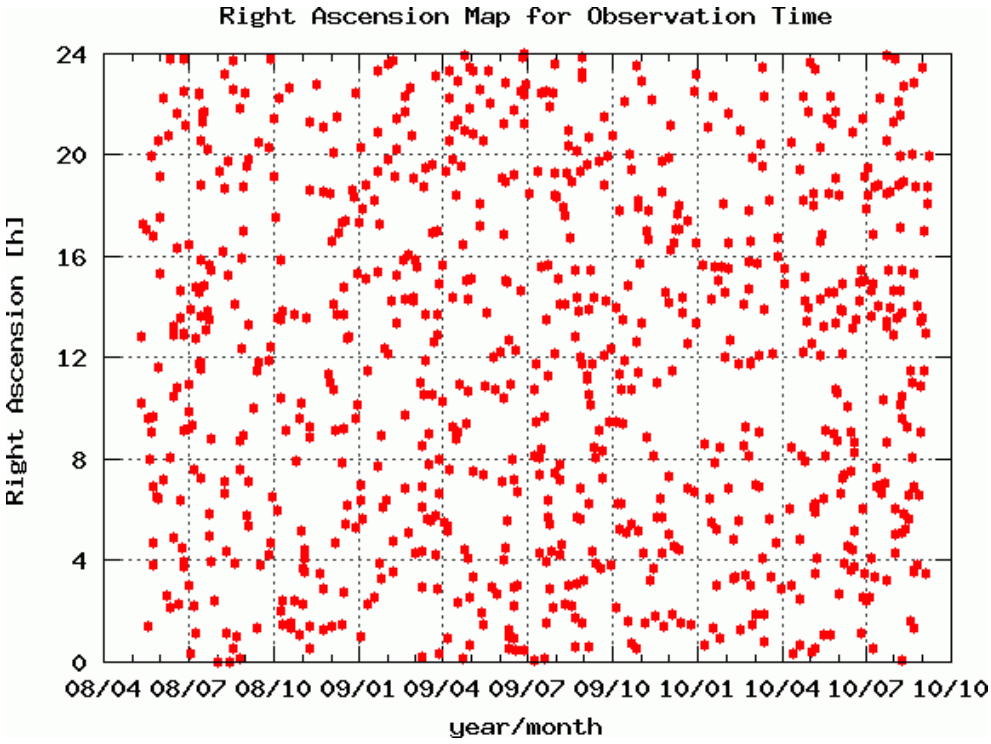

Figure 60: Scatter plot of the events for detected time and right ascension, The estimated energy of these event is higher than 10 EeV.

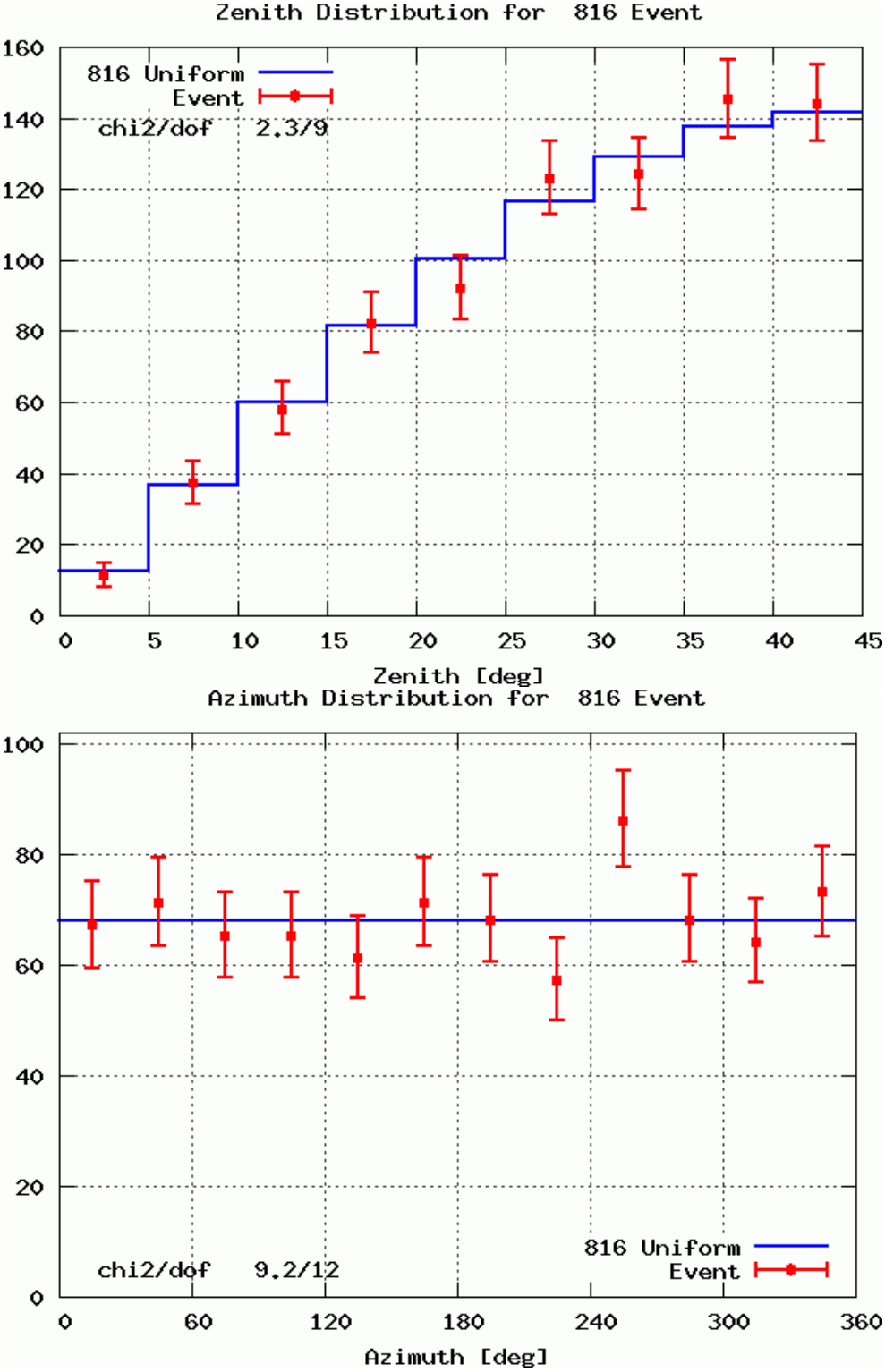

Figure 61: Arrival direction distribution in the horizontal coordinate for the events whose energy is higher than 10 EeV. The error bars and the chi-square comes from binomial distribution. Top: Zenith angle distribution, Bottom: Azimuth angle distribution.

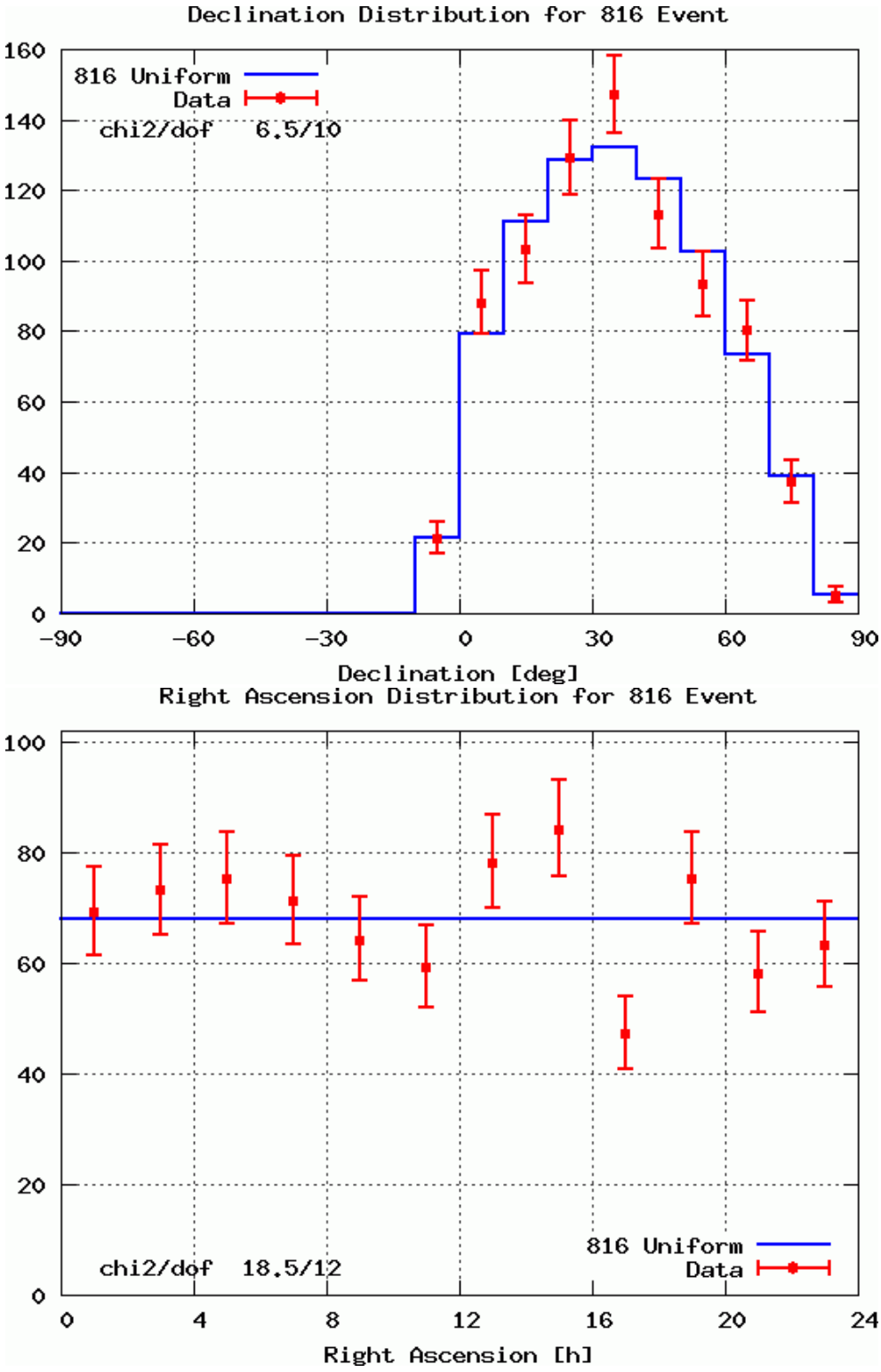

Figure 62: Arrival direction distribution in the equatorial coordinate for the events whose energy is higher than 10 EeV. The error bars and the chi-square comes from binomial distribution. Top: Declination distribution, Bottom: Right Ascension distribution.

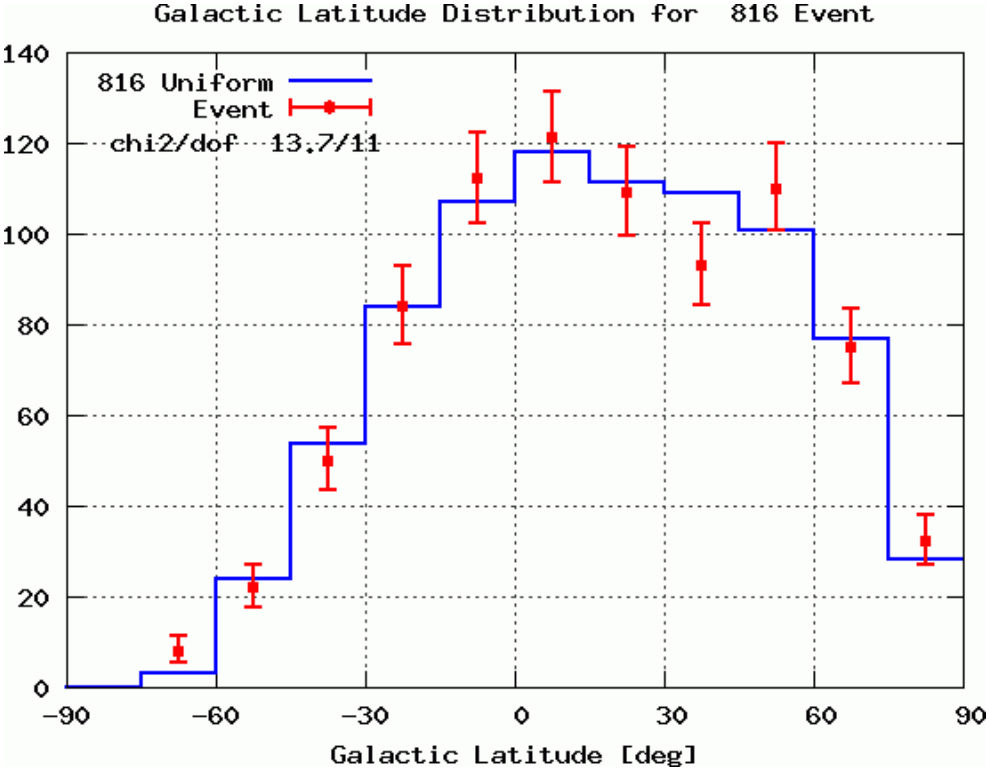

Figure 63: Arrival direction distribution in the galactic latitude for the events whose energy is higher than 10 EeV. The error bars and the chi-square comes from binomial distribution.

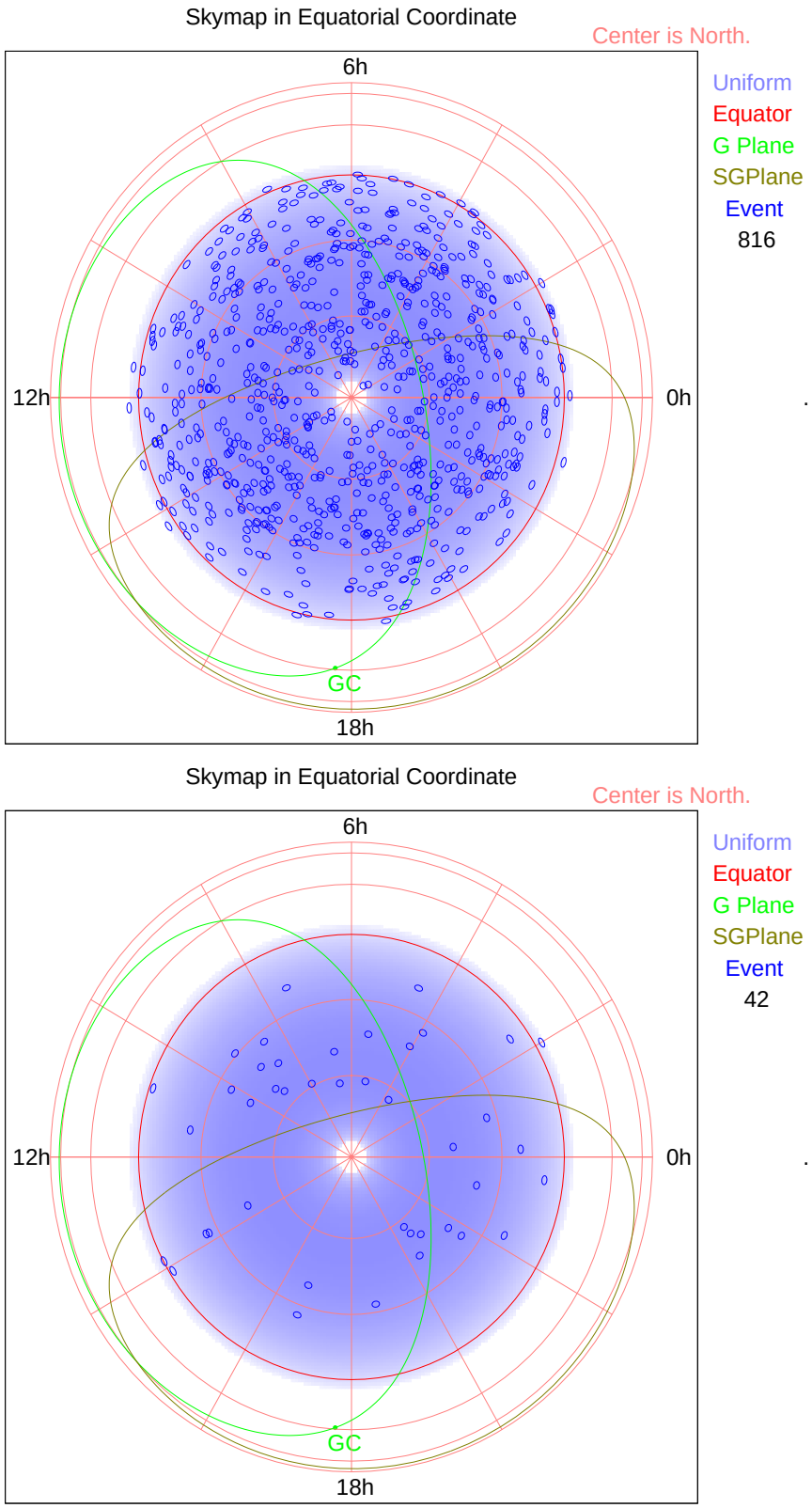

Figure 64: Sky map of cosmic rays observed by TASD in the equatorial coordinate. The radius of point is 1.25°. Top: For the events whose energy is higher than 10 EeV, Bottom: For the events whose energy is higher than 40 EeV.

4.2 Auto-correlation analysis

A separation angle is defined as an open angle of any two events. The auto-correlation analysis procedure is following. First, separation angle is calculated for all pairs. Second, the number of pairs in certain range of separation angle is counted. Third, the counted number of pairs is compared with the number of pairs in same procedure from model calculation whose event statistics is same. The bin width is 1° for separation angle distribution in this thesis. The counting example for auto-correlation analysis is shown in right figure. A cross point shows a event direction. The closest circle to the same colored cross point shows 1° open angle from the event. And their concentric circles radius (means open angle) increases by 1°. The first bin correspond to the separation angle between 0° and 1°. The separation angle of red event and blue event pair is between 2° and 3°. Therefore, the number of pairs in third bin is counted up.

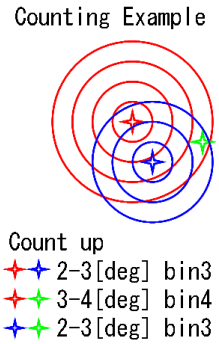

The separation angle distribution from model is obtained by a lot of arrival direction Monte Carlo (arrival MC) sets. If there are small scale clusters of arrival direction of ultra high energy cosmic rays, the observed data and the isotropic arrival MC data should be different in separation angle distribution. Therefore, I searched small scale clusters by auto-correlation analysis with separation angle distribution.

The example pair distribution for first and fifth separation angle bin is shown in Figure 65.

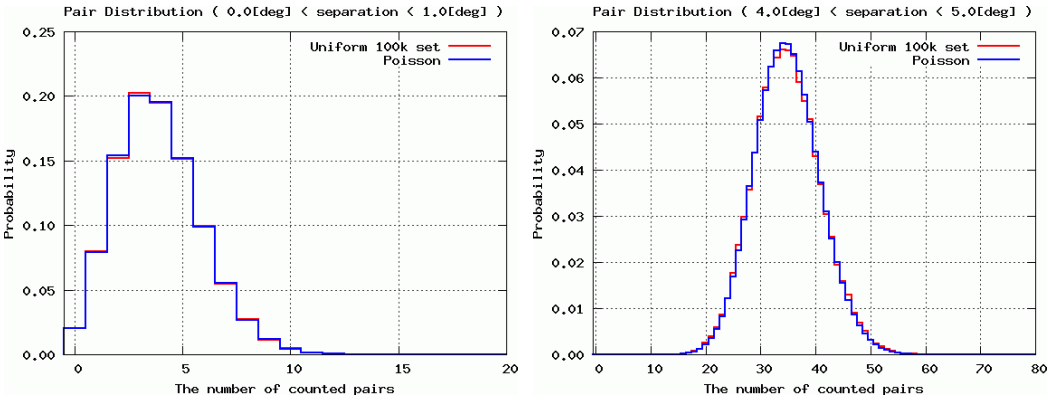

Figure 65: The pair distribution for first and fifth separation angle bin. The statistics is same as statistics for events whose energy is higher than 20 EeV. Red: The pair distribution of arrival MC. Blue: Poisson distribution whose average is arrival MC pair average. Left: Histogram for the number of pairs whose separation angle is between 0° and 1° (1st bin). Right: Histogram for the number of pairs whose separation angle is between 4° and 5° (5th bin).

The separation angle distribution of events higher than 20 EeV is shown in

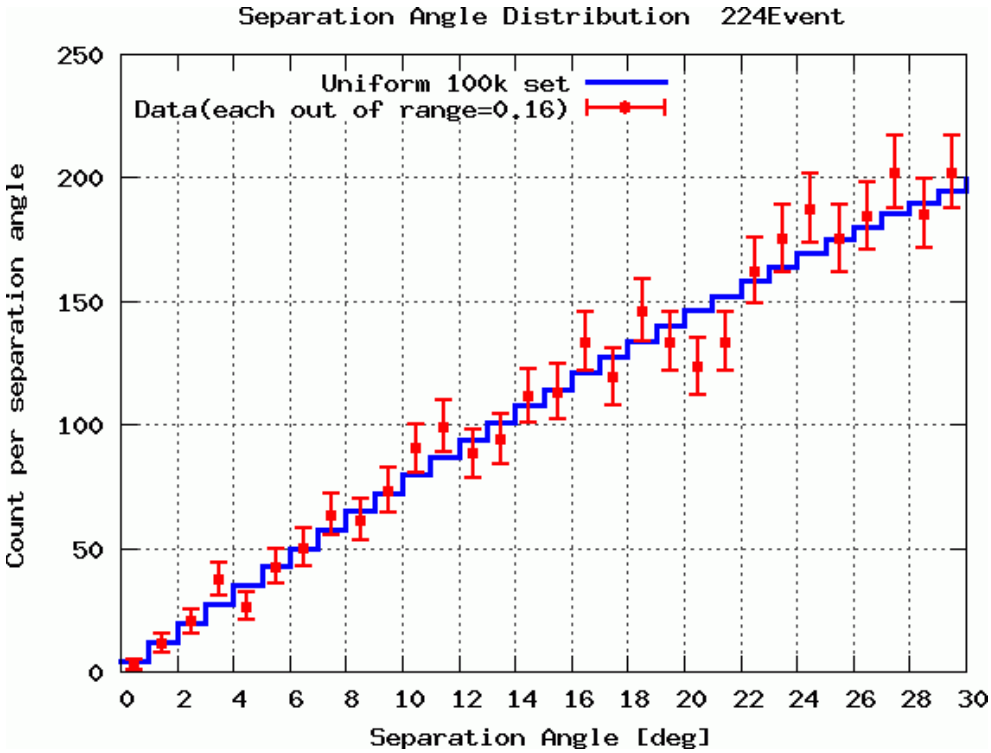

Figure 66: Separation angle distribution of events whose energy is higher than 20 EeV. The outside of error bar contains 16% from Poisson for each side. Therefore, the error bars represent 68% by Poisson, and in 84% for zero count.

Figure 66. The separation angle distribution normalized by solid angle to the first bin is shown in Figure 67. This is same style of AGASA plot in Figure 10. These two sets of separation angle distribution is very different at the small separation angle region. In TASD dataset, there is no indication of small scale clusters evaluated with isotropic model, which was pointed out by AGASA [17].

The number of pair that separation angle is less than certain angle is called doublet count. The doublet distribution in 2.5° and 5.0° is shown in Figure 68. (i.e. the doublet distribution for 1.0° is shown in left of Figure 65.)

The doublet counting in 2.5° and 5.0° for some energy threshold are shown in Table 3. The doublet counting in 2.5° was done by AGASA for events whose energy is higher than 40 EeV. From isotropic model, the average and deviation of doublet count is 1.7 and 1.36. However, there are 8 doublets in observed data [17]. From Table 3, The TASD result about doublet count (means small scale cluster) is very consistent with isotropic model, which model is inconsistent with AGASA [17].

The exposure of AGASA and TA covers almost same region on the sky. Therefore, the correlation analysis of AGASA 57 events whose energy is higher than 40 EeV [18] with TASD events is possible. In this case, the pair is defined between AGASA and TA events, not any two events. And separation angle is calculated for all pairs. Finally, the number of pairs whose open angle is within certain angle is compared with the number of pairs in same procedure

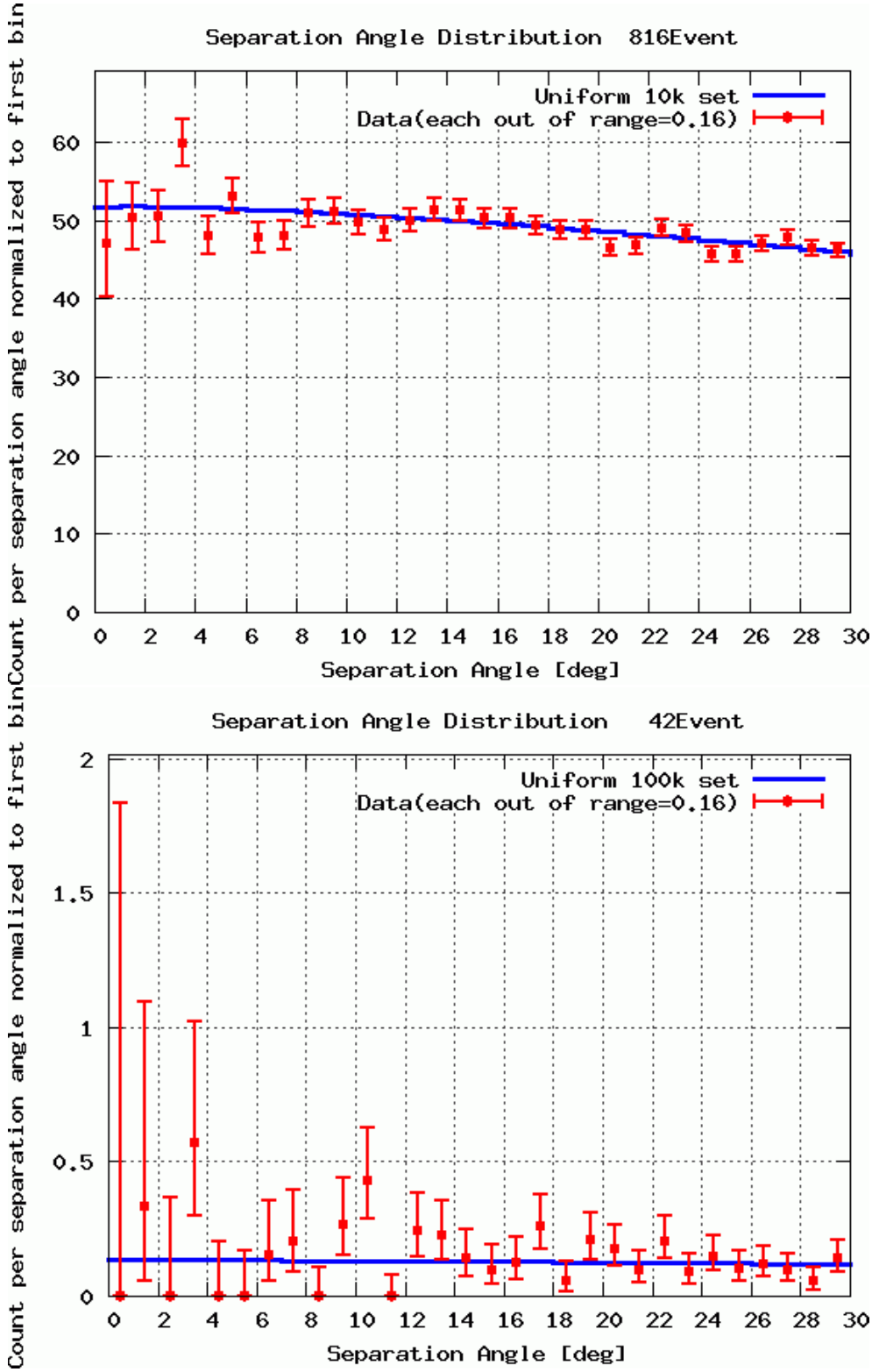

Figure 67: Separation angle distribution normalized by solid angle to first bin. Top: For the events whose energy is higher than 10 EeV, Bottom: For the events whose energy is higher than 40 EeV. The outside of error bar contains 16% from Poisson for each side. Therefore, the error bars represent 68% by Poisson, and in 84% for zero count.

from model calculation whose event statistics is same. I tested the observed TASD 42 events whose energy is higher than 40 EeV with isotropic model. The doublet count in 2.5° is average 2.17, deviation 1.61, observed 0. Therefore, the doublet count between AGASA and TASD event is consistent with TA isotropic expectation.

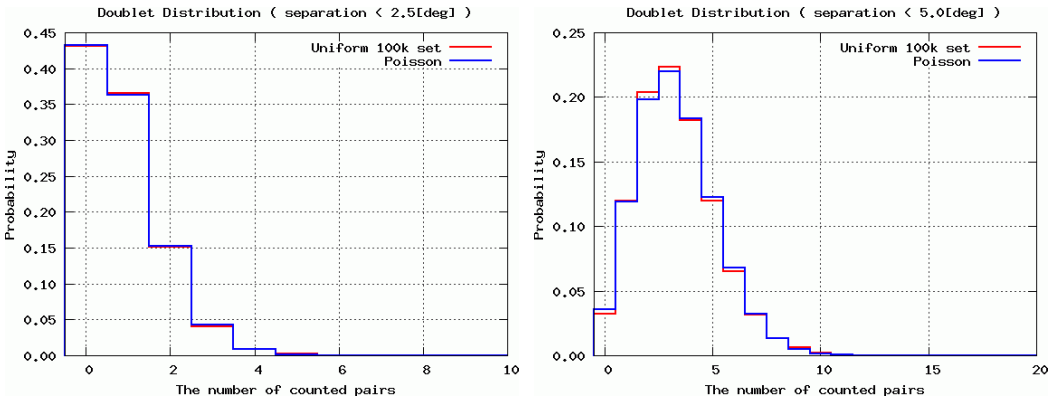

Figure 68: The doublet distribution in 2.5° and 5.0°. The statistics is same as statistics for events whose energy is higher than 40 EeV. Red: The doublet distribution of arrival MC. Blue: Poisson distribution whose average is arrival MC doublet average. Left: Histogram for the number of pairs whose separation angle is less than 2.5°. Right: Histogram for the number of pairs whose separation angle is less than 5.0°.

Energy Threshold	Events	Average	Deviation	Observed
10 EeV	816	323.5	18.9	311
20 EeV	224	24.31	5.01	20
30 EeV	83	3.32	1.82	2
40 EeV	42	0.838	0.919	1
50 EeV	22	0.225	0.474	0

Energy Threshold	Events	Average	Deviation	Observed
10 EeV	816	1291.0	42.2	1300
20 EeV	224	97.1	10.4	96
30 EeV	83	13.22	3.69	17
40 EeV	42	3.33	1.83	5
50 EeV	22	0.896	0.947	1

Table 3: Observed doublet count for some energy threshold with MC doublet count average and deviation from same statistics isotropic model. Top: Doublet in 2.5°. Bottom: Doublet in 5.0°.

5 Conclusion

The Surface Detector Array of Telescope Array experiment started the observation in March 2008, and it is collecting shower data continuously. Therefore, this result about small scale clusters will be updated.

I participated from the test production phase of the particle detection part of SD. I worked for mass production, deployment, adjustment, calibration and maintenance for SD. I developed the shower reconstruction program for direction analysis, and achieved that the angular resolution is 1.4° and 0.8° for primary energy 10 EeV and 40 EeV events. By this reconstructed data, I plotted the sky map of ultra high energy cosmic rays (Figure 64), and searched for small scale clusters by auto-correlation analysis (Figure 67 and Table 3).

The arrival direction distributions of detected events whose energy is higher than 10 EeV is consistent with isotropic model. Therefore, I searched for small scale clusters from 850-day TASD data by auto-correlation method, which is evaluated with isotropic model. The result is that there were no small scale clusters which is significantly more than isotropic model expectation for several energy threshold. The TASD result about small scale clusters was inconsistent with AGASA result by auto-correlation analysis [17]. For 40 EeV energy threshold, there is 1 pair whose open angle is less than 2.5°, 0.84 pair expected from isotropic model. The equatorial direction (δ, α) of pair events is (24.5°, 206.9°) × (25.9°, 207.0°). From Veron Catalog of Quasars & AGN, 13th Edition object which redshift is less than 0.05, the closest direction object is "IC 910" at (23.3°, 205.3°), $z = 0.027$. The other close direction objects are "MARK 661" and "SDSS J13275+2446".

If these cosmic rays are proton, this result does not favor simultaneous situation that the intergalactic magnetic field is weak and the number density of cosmic ray source is small.

Acknowledgements

I greatly thank Dr. Y. Hayashi and Dr. S. Ogio in Osaka City University for serving the environment to study and teaching to write this thesis. I also greatly thank Dr. M. Fukushima, Dr. H. Sagawa and Dr. M. Takeda in University of Tokyo for discussion and guide to study anisotropy analysis. In addition, I am grateful to Dr. S. Kawakami in Osaka City University for giving the chance to study cosmic ray with Telescope Array.

I dearly thank Dr. N. Sakurai, Dr. S. Ozawa, Dr. D. Ikeda, for assisting my work. I greatly thank Dr. T. Nonaka guiding the basic data handling and reading. I am grateful to Mr. A. Taketa serving many tools and ideas. Those components are essential for my study. I greatly thank Mr. E. Kido serving ideas and discussing about arrival direction analysis. I dearly thank Mr. T. Tomida helping my work at site and encouraging my study.

I greatly thank all collaborators, especially Dr. J. N. Matthews, Dr. R. Cady, Dr. K. Martens, Dr. G. Thomson, Dr. K. Honda, Dr. T. Ishii, Dr. K. Kasahara, Dr. M. Chikawa, Dr. Y. Tsunesada, Dr. H. Tokunou, Dr. S. Udo, Dr. T. Shibata, Dr. Y. Tameda, Mr. H. Ohoka, Mr. H. Shimodaira, Mr. K. Yamamoto, Mr. Y. Kondo, Mr. T. Matsuyama, Mr. D. Barr, Mr. D. Ivanov, Dr. G. Rubtsov, Mr. E. Barcikowski, Dr. A. Oshima, Ms. M. Minamino, Mr. T. Fujii, Mr. Y. Yamakawa, Mr. Y. Takahashi, Mr. Y. Wada, Mr. T. Kanbe, Mr. S. Iwamoto, Mr. Y. Tsuyuguchi, Mr. H. Ukai, Mr. K. Miyata, Mr. K. Kobayashi, Ms. S. Y. Roh, Ms. J. H. Kim and Ms. J. H. Lim.

Finally, I greatly thank my family very much for numerous supports.

The Telescope Array experiment is supported by the Ministry of Education, Culture, Sports, Science and Technology-Japan through Kakenhi grants on priority area (431) "Highest Energy Cosmic Rays", basic research awards 18204020(A), 18403004(B) and 20340057(B); by the U.S. National Science Foundation awards PHY-0307098, PHY-0601915, PHY-0703893, PHY-0758342, and PHY-0848320 (Utah) and PHY-0649681 (Rutgers); by the Korea Research Foundation (KRF-2007-341-C00020); by the Korean Science and Engineering Foundation (KOSEF, R01-2007-000-21088-0); by the Russian Academy of Sciences, RFBR grants 07-02-00820a and 09-07-00388a (INR), the FNRS contract 1.5.335.08, IISN and Belgian Science Policy under IUAP VI/11 (ULB). The foundations of Dr. Ezekiel R. and Edna Wattis Dumke, Willard L. Eccles and the George S. and Dolores Dore Eccles all helped with generous donations. The State of Utah supported the project through its Economic Development Board, and the University of Utah through the Office of the Vice President for Research. The experimental site became available through the cooperation of the Utah School and Institutional Trust Lands Administration (SITLA), U.S. Bureau of Land Management and the U.S. Air Force. We also wish to thank the people and the officials of Millard County, Utah, for their steadfast and warm supports. We gratefully acknowledge the contributions from the technical staffs of our home institutions and the University of Utah Center for High Performance Computing(CHPC).

Appendix

Sky map in the galactic coordinate

This sky map is same as Figure 64 in the galactic coordinate.

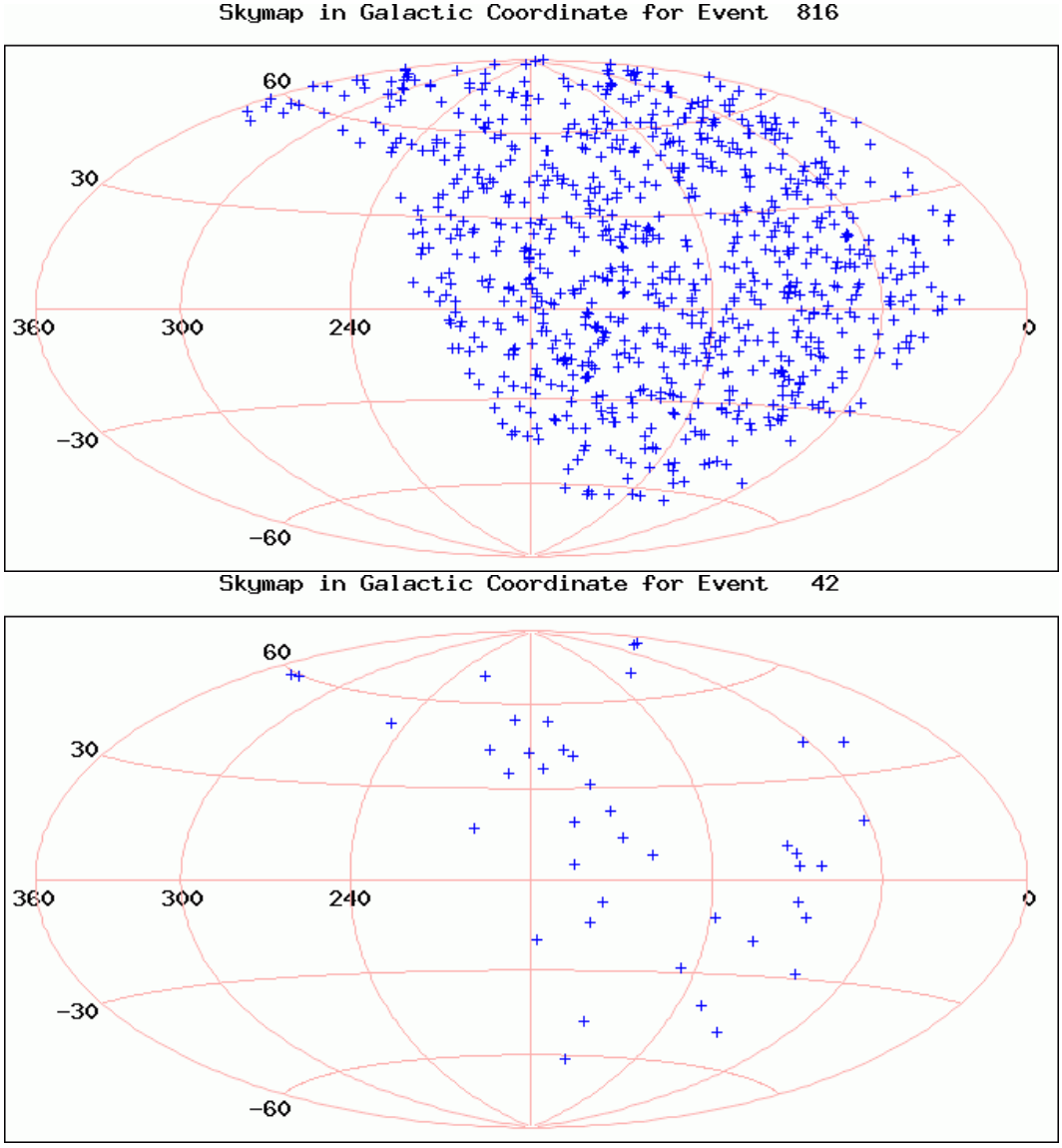

Figure 69: Sky map of cosmic rays observed by TASD in the galactic coordinate. Top: For the events whose energy is higher than 10 EeV, Bottom: For the events whose energy is higher than 40 EeV.

Relative Timing and Position Resolution

The relative timing of arrival particles for each SD and the detector position are important to reconstruct the air shower data precisely. Both of these relate to GPS which is used in SD. The GPS module for SD is "M12+ Timing Receiver" produced by Motorola. Here is some calibration results for these resolution.

Relative Timing

The relative timing is measured at workshop near TA site. The setup of measurement is shown in Figure 70. In principle, this measurement can be done in laboratory. However, the multiple path effect for GPS antenna is large on the roof of workshop. Therefore, I measured in almost same condition as field running SDs.

There are three components of relative timing resolution. One is the fluctuation of 1PPS generated by GPS module. Another is the individual difference of GPS for 1PPS. The other is the fluctuation of clock speed. The fluctuation of clock speed is ignored here. This measurement is done by four sets of SD electronics.

- One is a standard set for the relative measurement. (Changing None)
- Another set is for the reproducibility. (Changing None)
- Another set is for the board dependency. (Changing GPS board)
- The other set is for the antenna dependency. (Changing GPS antenna)

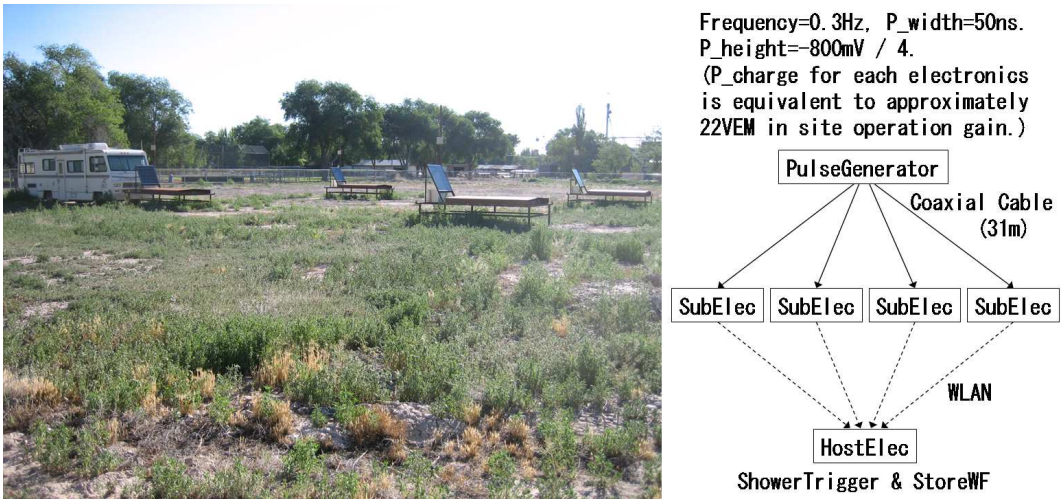

Figure 70:

There are some operation mode for GPS. The default mode is Position Survey Mode. This is for usual GPS positioning and the timing resolution is affected by unstable positioning. However, there is another operation mode, Position Hold Mode. This mode is valid for static GPS operation and required the fixed position information previously. The improvement of timing resolution for operation mode is shown in Figure 71.

The relative timing measurement is done in Position Hold Mode. The method to get the stable position information for this mode and for shower reconstruction is described later. The fluctuation of 1PPS for relative timing is 12.0 ns in Position Survey Mode and 9.2 ns in Position Hold Mode for each SD from standard deviation of the histogram like Figure 71. The individual difference for relative timing comes from peak variation of the histogram like

Figure 72. The reproducibility of the peak is 2.1 ns. The board dependency of the peak is 10.9 ns. The antenna dependency of the peak is 2.3 ns. The estimated total individual difference is 11.1 ns.

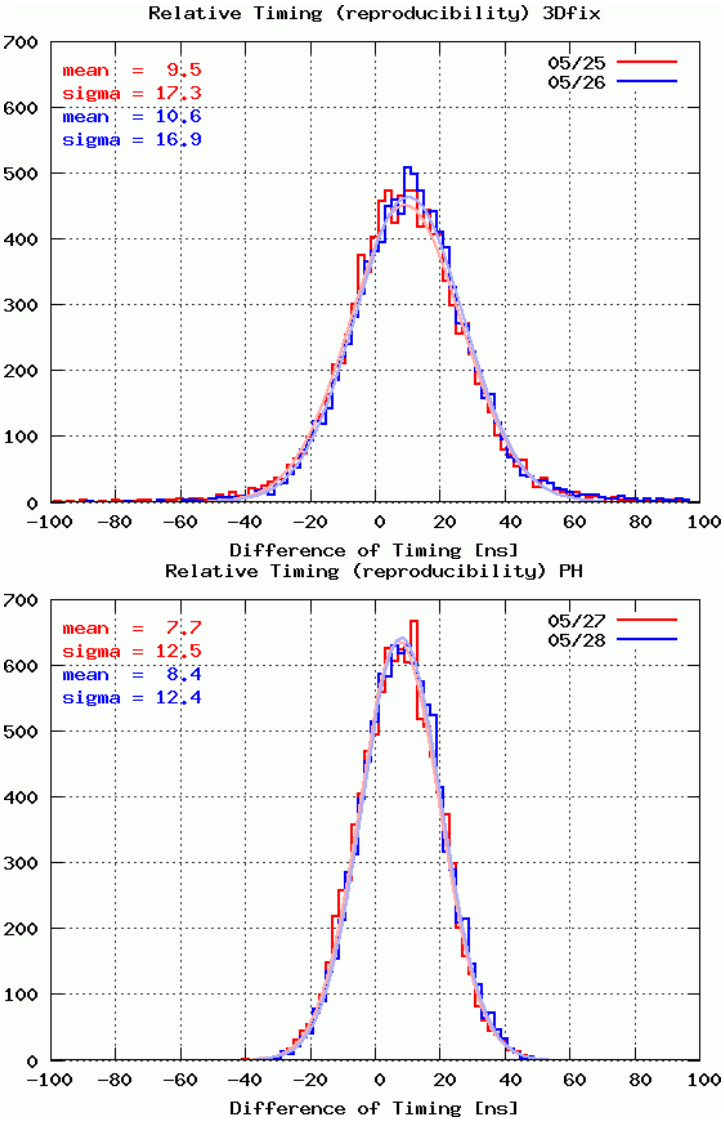

Figure 71: Relative timing histogram for two type of GPS operation mode. Top: Position Survey Mode. Bottom: Position Hold Mode.

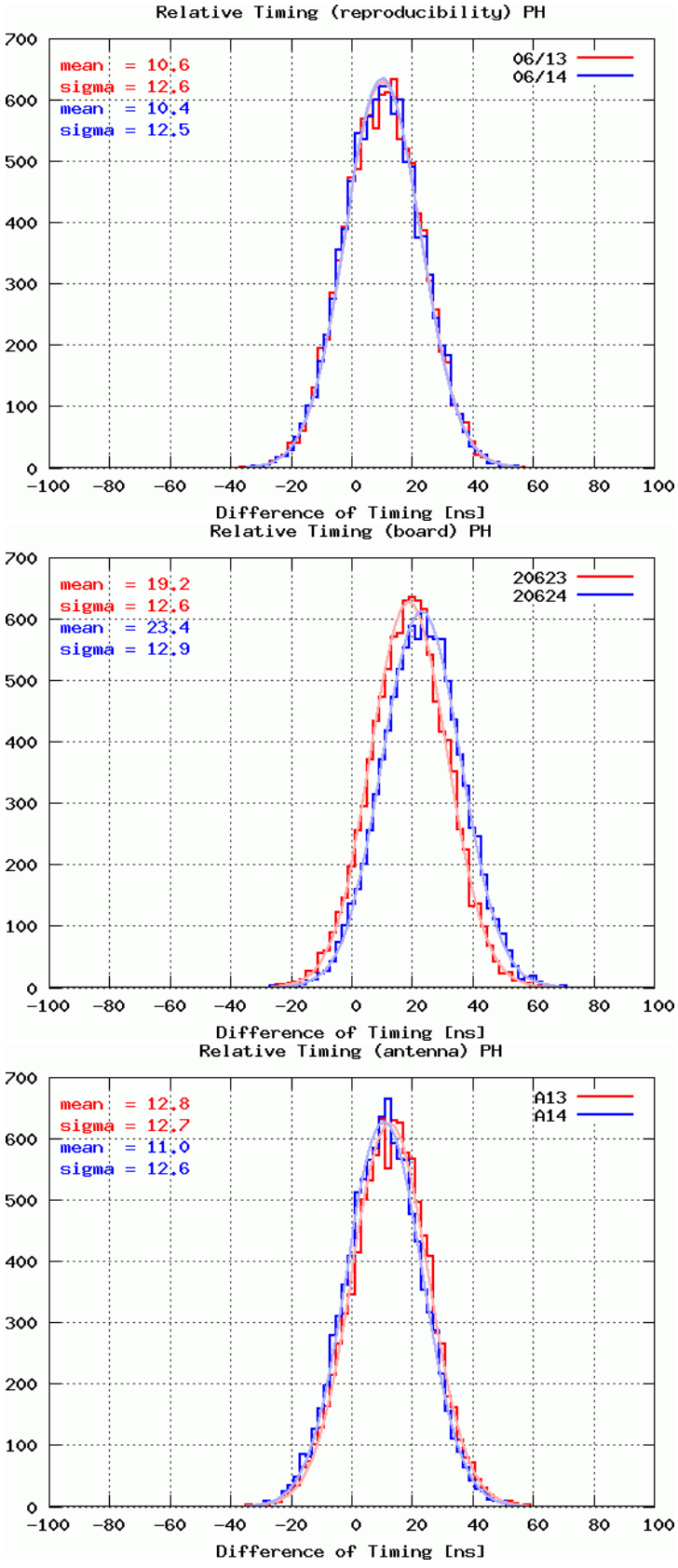

Figure 72: Relative timing histogram in Position Hold Mode. Top: Reproducibility. Middle: Board dependency. Bottom: Antenna dependency.

Detector Position

In order to get higher resolution of relative timing, the fixed position information is required for operating Position Hold Mode. The transition of GPS information is shown in Figure 73. Therefore, it is very dangerous, especially for altitude, to determine the position in short time measurement.

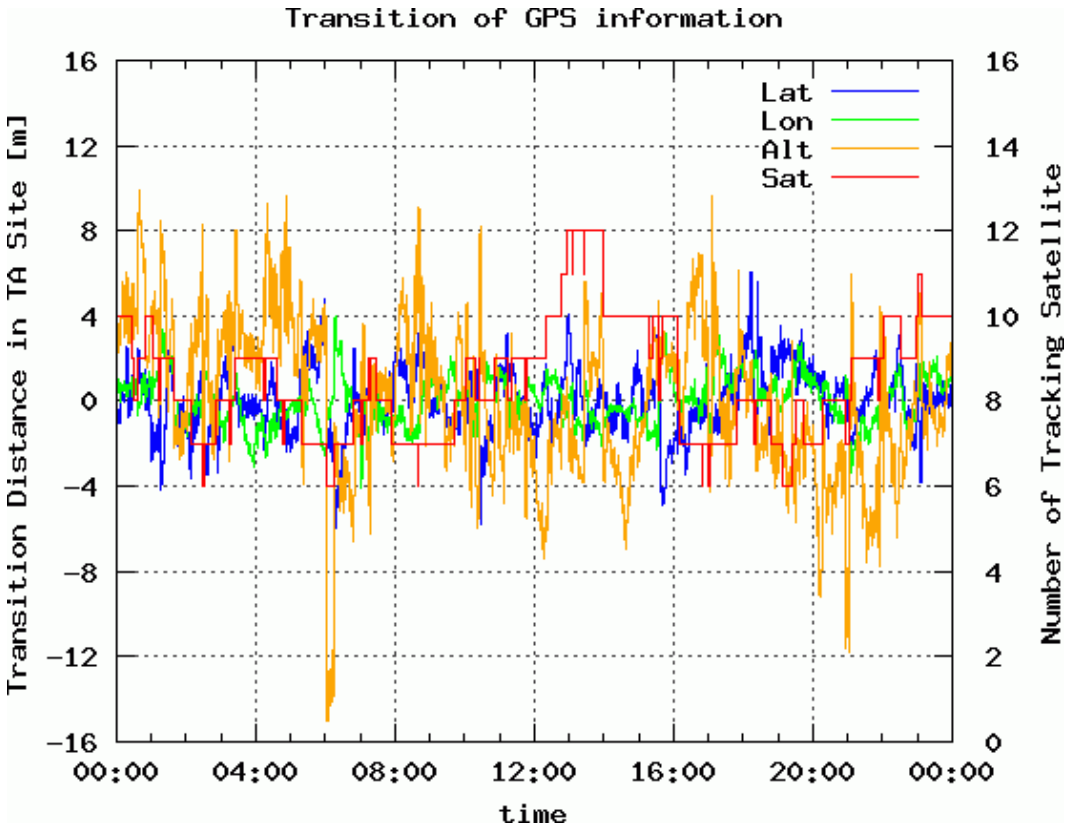

Figure 73: Transition of GPS information. Left Y: 0 is the average of one day position measurement for latitude, longitude and altitude. For latitude and longitude, values are converted to distance in TA site. (3.1 cm/mas in latitude, 2.4 cm/mas in longitude)

The GPS satellite orbit the earth twice a sidereal day. In order to get stable position, one set of position measurement takes place in continuous 86400 seconds (=1 day) and the measurement takes place at least three sets to reduce the unstable atmospheric effect. The procedure of one set of position measurement is here.

1. Changing the operation mode to Position Survey Mode.

2. Searching continuous 600 seconds with achieving enough GPS information.

3. Storing 1 second information of position, and this is the standard position for average and histogram.

4. Storing 86400 seconds position information with Position Survey Mode to average and histogram. In addition, storing raw position information every 300 seconds.

5. Setting the position for Position Hold Mode, according as measuring mode.

6. Changing the operation mode to Position Hold Mode, according as measuring mode.

7. Getting position data through the host electronics.

The position determination of one measurement is the weighted average after removing 10% of statistics for each side of histogram. The stable position for Position Hold Mode and shower reconstruction is the average of some sets of measurement, at least three sets.

The precision of position is estimated ± 50 cm for horizontal and ± 100 cm for vertical by measuring multiple sets and checking by exchanging GPS module. However, the relative position accuracy is not measured properly yet. But, all SDs use same type of GPS module. Therefore, even if there are some biases for absolute position, somewhat setoff effect is expected for relative accuracy. The relative timing and position are important for shower reconstruction, especially for arrival direction resolution. The relative position measurement by static interferometric method is desired to confirm the current position information.

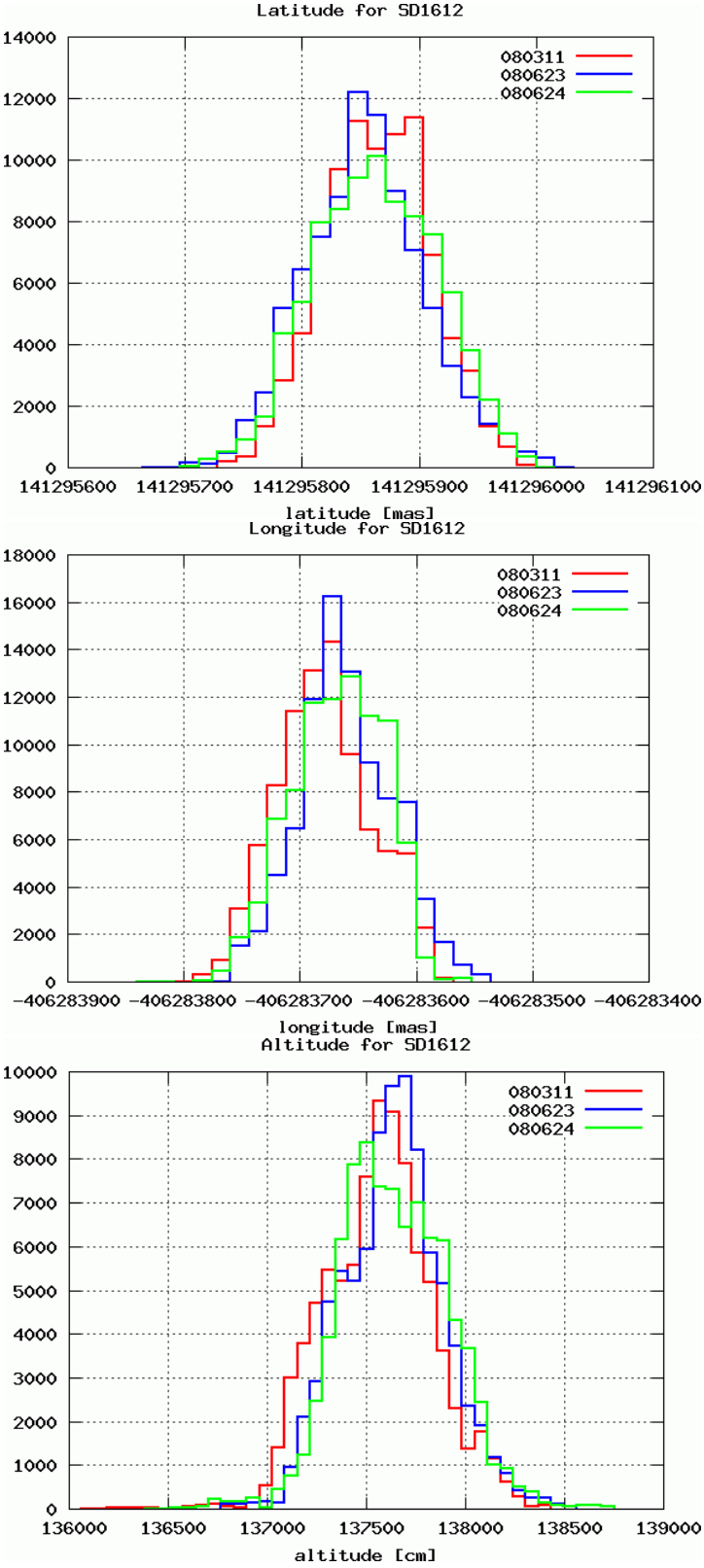

Figure 74: Position histogram for three days. Top: Latitude (full range = 15.5 m). Middle: Longitude (full range = 12.0 m). Bottom: Altitude (full range = 30.0 m)

References

[1] *Observations and implications of the ultrahigh-energy cosmic rays*
M. Nagano and A. A. Watson, Rev. Mod. Phys. 72, p.689 (2000)

[2] *On the Origin of the Cosmic Radiation*
E. Fermi, Phys. Rev. 75, p.1169 (1949)

[3] *Origin and propagation of the highest energy cosmic rays*
R. J. Protheroe, arXiv:astro-ph/9612212 (1996)

[4] *End to the Cosmic-Ray Spectrum*?
K. Greisen, Phys. Rev. Lett. 16, p.748 (1966)

[5] *Upper Limit of the Spectrum of Cosmic Rays*
G. T. Zatsepin and V. A. Kuz'min, JETP Lett. 4, p.78 (1966)

[6] *Direction of a Cosmic − Ray with Measured Energy Well Beyond the Expected Spectral Cutoff Due to Cosmic Microwave Radiation*
D. J. Bird, et al, Astrophysical J. 441, p.144 (1995)

[7] *Observation of a Very Energetic Cosmic Ray Well Beyond the Predicted* $2.7K$ *Cutoff in the Primary Energy Spectrum*
N. Hayashida, et al, Phys. Rev. Lett. 73, p.3491 (1994)

[8] *Astroparticle Theory : Some New Insight into High Energy Cosmic Rays*
E. Roulet, arXiv:astro-ph/0310367 (2003)

[9] *Diffusion and drift of cosmic rays in highly turbulent magnetic fields*
J. Candia, E. Roulet, arXiv:astro-ph/0408054 (2004)

[10] *Deflections of cosmic rays in a random component of the Galactic magnetic field*
P. G. Tinyakov, I. I. Tkachev, Astroparticle Physics 24, p32 (2005)

[11] *Cosmic Rays and Particle Physics*
T. K. Gaisser, Cambridge University Press(1991)

[12] *Reliability of the method of constant intensity cuts for reconstructing the average development of vertical showers*
T. K. Gaisser, A. M. Hillas, Proc. 15th ICRC 8, p.353 (1977)

[13] *The Extensive Air Shower*
K. Greisen, Progress in Cosmic Ray Physics 3 (1956)

[14] *Atomic and nuclear properties of materials : Air* $(dry,\ 1\ atm)$
Particle Data Group

[15] *Akeno Giant Air Shower Array* $(AGASA)$ *covering* $100\ km^2$ *area*
N. Chiba, et al, Nucl. Instrum. Methods Phtys. Res. A 331, p.338 (1992)

[16] *Energy Determination in the Akeno Giant Air Shower Array Experiment*
M. Takeda, et al, Proc. 28th ICRC 1, p.381 (2003)

[17] *AGASA Results* (*anisotropy*)
M. Takeda, et al, J. Phys. Soc. Jpn. 20, Suppl. B p.15 (2001)

[18] *Updated AGASA event list above* $4x10^{19}$ *eV*
N. Hayashida, et al, arXiv:astro-ph/0008102 (2000)

[19] *Description of the High Resolution Fly's Eye Detector*
J. N. Matthews et al, Proc. 27th ICRC p.350 (2001)

[20] *Measurement of the flux of ultra high energy cosmic rays by the stereo technique*
R. U. Abbasi et al, Astroparticle Physics 32, p.53 (2009)

[21] *Anisotropy Searches with the High-Resolution Fly's Eye*
J. Belz et al, Nuclear Physics B (Proc. Suppl.) 165, p.239 (2007)

[22] *Indications of Proton-Dominated Cosmic-Ray Composition above* 1.6 *EeV*
R. U. Abbasi et al, Phys. Rev. Lett. 104, 161101 (2010)

[23] *Properties and performance of the prototype instrument for the Pierre Auger Observatory*
Pierre Auger Collaboration, Nucl. Instrum. Methods Phtys. Res. A 523, p.50 (2004)

[24] *Measurement of the energy spectrum of cosmic rays above* 10^{18} *eV using the Pierre Auger Observatory*
Pierre Auger Collaboration, Physics Letters B 685, p.239 (2010)

[25] *Update on the correlation of the highest energy cosmic rays with nearby extragalactic matter*
Pierre Auger Collaboration, Astroparticle Physics 34, p.314 (2010)

[26] *Measurement of the Depth of Maximum of Extensive Air Showers above* 10^{18} *eV*
J. Abraham et al, Phys. Rev. Lett. 104, 091101 (2010)

[27] mapped by R. Cady, in private communication

[28] *Toward a comparison of fluorescence energy scale and spectra between Telescope Array and the High Resolution Fly's Eye*
C. C. H. Jui et al, Proc. 31th ICRC (2010)

[29] *Calibration of the Telescope Array Experiment Fluorescence Detectors*
D. Ikeda et al, Proc. 31th ICRC (2010)

[30] *Measurement of atmospheric transparencies with LIDAR for Telescope Array*
T. Tomida et al, Proc. 31th ICRC (2010)

[31] *Cloud Monitoring with an Infra-Red Camera for the Telescope Array Experiment*
M. Chikawa et al, Proc. 31th ICRC (2010)

[32] *An Electron Linear Accelerator for end-to-end absolute energy calibration of atmospheric fluorescence telescopes of the Telescope Array experiment*
T. Shibata et al, Proc. 31th ICRC (2010)

[33] figured by A. Taketa, in private communication

[34] *The Geant4 Toolkit : simulation capabilities and application results*
M. G. Pia, et al, Nuclear Physics B (Proc. Suppl.) 125, p.60 (2003)

[35] *A New Parallel Processing Scheme Enabling Full Monte Carlo EAS Simulation in the GZK Energy Region*
K. Kasahara and F. Cohen, Proc. 30th ICRC (2008)

[36] *QGSJET-II : towards reliable description of very high energy hadronic interactions*
S. Ostapchenko, Nuclear Physics B (Proc. Suppl.) 151, p.143 (2006)

[37] *The Monte Carlo Event Generator DPMJET-III*
S. Roesler, et al, arXiv:hep-ph/0012252 (2000)